Comparative Studies for the Sodium and Potassium Atmospheres of the Moon and Mercury

William H. Smyth

Atmospheric and Environmental Research, Inc.
840 Memorial Drive
Cambridge, MA 02139-3794

February 9, 1999

Final Report for the Period
February 1, 1995 to January 31, 1999

TABLE OF CONTENTS

I. INTRODUCTION

The overall objective of this project is to advance our physical understanding of the exospheric sodium and potassium atmospheres (and comae) of the Moon and Mercury both individually and collectively. This objective will be approached by undertaking studies for these atmospheres to improve significantly our understanding of their sources, sinks, transport, and interactions with the surfaces of these bodies and also how these processes affect their observed relative abundances, spatial distributions, and temporal variabilities. Information for sodium and potassium gained in this way will also be used to increase our understanding of the nature of other neutral constituents in the atmospheres. The primary scientific significance of the proposed research is to elucidate -- through interpretation and comparison of different observations self-consistently with a physically-based model -- the interplay that exists between key physical processes that determine the current state (and ultimately may have affected the time evolution) of the atmospheres of the Moon and Mercury.

To achieve these objectives, both theoretical studies and modeling analysis of images and spectrographic measurements of the solar resonance excited emission lines of sodium and potassium atoms in these atmospheres will be undertaken using highly-developed, physically-based models at AER. The basic strategy is first to undertake and complete very basic theoretical studies to evaluate the relative importance of various physical processes in shaping the sodium and potassium atmospheres of the Moon and Mercury, and second to use this detailed knowledge in modeling analysis studies of observational data for these atmospheres. The need for these more physically complete models to improve the modeling analysis studies is evident in the literature. The project combines through collaborative efforts a solid and already existing Moon/Mercury modeling analysis program at AER with two separate and excellent ground-based observing programs for the sodium and potassium atmospheres of the Moon and Mercury. Observational data analyzed for Mercury has been provided by an ongoing collaborative effort with A. E. Potter who is heading a very productive and continuing ground-based observing program initiated in January 1985 by the discovery of Mercury's sodium atmosphere (Potter and Morgan 1985) and expanded in 1986 by the discovery of Mercury's potassium atmosphere (Potter and Morgan 1986). Observational data analyzed for the Moon has been provided by an expanded collaborative effort with A. E. Potter, who is heading a very productive ground-based observing program initiated in January 1988 by the discovery of the lunar sodium and potassium atmospheres (Potter and Morgan 1988). A collaborative effort with R. M. Killen was also established for the purpose of properly treating the radiative transfer for the sodium emission from Mercury's atmosphere, which is the

only one of the four atmospheres of interest in this project thought to be optically thick. Sodium observations for Mercury analyzed to date have, however, been optically thin, as discussed below.

The availability in this project of reduced observational data in our collaboration with A. E. Potter, particularly for the atmospheres of Mercury, has been much slower than initially anticipated. This has been partly due (1) to limited funds for A. E. Potter to process these data and (2) to the realization that atmospheric and instrumental smearing in the existing sodium atmospheric data for Mercury must be understood before modeling studies could effectively proceed. This delay prompted the addition of a fourth-year no-cost extension to facilitate the situation. During the fourth-year, additional observational image data for the sodium atmosphere of Mercury (Potter et al. 1999) has been effectively reduced, including the Fourier transform deconvolution of atmospheric and instrumental smearing, and made available to us for modeling studies. Modeling of additional Mercury and lunar observational data undertaken beyond the first project year, including these new data for Mercury, are reported below for the Moon and Mercury, respectively, in Sections 3 and 4.

II. THEORETICAL OVERVIEW & MODELING OF EARLIER OBSERVATIONS

Research initiated during the prior three-year period of our ongoing program and completed in the first project year of this project is presented in the form of two papers in the appendix. Appendix A contains a theoretical overview and modeling for the sodium and potassium atmospheres of Mercury as published in The Astrophysical Journal in March 1995 (Smyth and Marconi 1995a). Appendix B contains a parallel paper for the sodium and potassium atmospheres of the Moon as published in The Astrophysical Journal in April 1995 (Smyth and Marconi 1995b). The paper for Mercury also has an accompanying video that shows various interesting space-time model-calculated animations for surface point sources of atomic sodium or potassium.

For the Mercury and lunar atmospheres, significant limitations in our physical knowledge to characterize and hence distinguish the separate effects of sources, sinks, transport, and gas-surface interactions in the behavior of the observational data still exist. Within the last year, however, significant progress that improves our understanding of the gas-surface processes, perhaps the poorest understood of these four factors, has begun to emerge based upon laboratory studies of Madey and Yakshinskiy (1998; Yakshinskiy and Madey 1998; Madey 1999). A source velocity distribution for sodium produced from electron-stimulated desorption of prepared surfaces and the cross section for the sodium atoms released are becoming available and are thought to apply equally as well to photon-stimulated desorption. It is very interesting to note that the source

velocity distribution for electron-stimulated desorption is very similar to a 1000 K Maxwellian velocity distribution that was determined earlier (e.g., Smyth and Marconi 1995b) to match the sodium brightness altitude profile at the lunar equatorial. In addition, new information on the temperature dependence of the surface sticking coefficient for sodium is also beginning to emerge. These initial gas-surface findings have begun to be available only in the (no-cost extension) fourth-year for this project so that we have been able to assess partially and only very preliminarily their impact on the modeling analysis. However, as shown below, the new velocity distribution is able to fit the observational data for both the sodium atmospheres of the Moon and Mercury. With this improvement in our understanding, future research should now be expected to make substantial and more rapid progress by continuing the comparison and study of the source, sink, transport and gas-surface factors that shape the atmospheres of the Moon and Mercury.

III. FURTHER STUDIES FOR THE MOON

3.1 Observational Data

Near Surface Sodium Data

The first image of the lunar sodium atmosphere near the surface for radial distances between about 1 and 2 lunar radii (R_L =1738 km), recently published by Potter and Morgan (1998) were made available to us for modeling in our collaboration with A. E. Potter. This sodium image in the D_2 emission line (5890 Å) was acquired on April 22, 1994 by use of the Evans 40 cm solar coronagraph at the National Solar Observatory at Sacramento Peak. In the image in Figure 1, the Moon is about three days past first quarter. At the subsolar point, the image extends to an altitude of about one lunar radius with a useful signal to noise measured up to an altitude of perhaps ~1200 km or so. The image extends in lunar latitude to ~±70° where the altitude coverage is highly reduced because of the restricted field of view captured on the CCD detector from the solar coronagraph. Observations from the surface to an altitude of ~100 km or so are also clearly affected by the occulting disk masking the lunar surface and are not appropriate for analysis. Modeling analysis of this image is presented in Section 3.2.

Far Surface Sodium Data

Spatially complementary images for the lunar sodium atmosphere measured in the sum of the D_1 (5896 Å) and D_2 (5890 Å) emission line brightnesses have also been acquired by Flynn and Mendillo (1993) for radial distances about 1.5 R_L and extending outward to ~8 R_L, i.e., for altitudes between about 900 km and 12,200 km. A direct imaging technique, where the bright reflected sunlight from the lunar disk is masked to distances somewhat larger than the lunar limb, was employed to acquire these images. An empirical fit to the observed sodium brightness, I,

(measured in kiloRayleighs) above a radius of ~1.5 R_L for an image acquired on September 30, 1991 is given by Flynn and Mendillo (1993) and cast into the form

$$I(r,\chi) = I_0(\chi)\, r^{-\alpha(\chi)}$$

where $\quad I_0(\chi) = (1 + 6\cos^8\chi) \quad$ and $\quad \alpha(\chi) = 2\,(1 + \cos^3\chi)$

and where r is the radial distance in units of R_L and χ is the solar zenith angle (latitude measured from the subsolar point). Model simulations for this image were undertaken by Flynn and Mendillo (1995) where surface sources were assumed that were both uniform and $\cos^N\chi$ dependent, with N having values of 1, 2, and even 10. As $\chi \to \pi/2$, all the model simulations presented yielded values for α and I_0 that were larger than observed, indicating that other physical factors not yet identified are present in the problem and that the source is much more complex in nature.

Sodium Observations for Different Lunar Phases

A collection of spectrographic observations acquired between altitudes of 10 to 70 km during the 1988-1993 time frame has been used by Potter and Morgan (1994) to investigate the variation of the sodium emission brightness as a function of lunar phase. The collection of observations indicates that the sodium brightness decreases for smaller lunar phase below about 30° (i.e., phase angle = 0° at full Moon), an angular location for which the Moon is approximately within the boundary of the Earth's magnetotail where solar wind sputtering should not occur. From this behavior they concluded that solar wind sputtering is the dominant process for sodium production. Alternatively, however, this behavior may be simply a geometric effect caused by the changing line of sight which samples, as $\chi \to \pi/2$, a smaller sodium atmospheric column density near the surface and hence would not require a decrease in the dominant source mechanism with smaller lunar phase. Preliminary modeling analysis of these data is presented in Section 3.2.

3.2 Modeling Analysis for the Lunar Sodium Atmosphere

Comparison of Different Model Profiles for Far Surface Sodium

Model calculations have been performed to compare sodium D_2 emission line brightness profiles above the surface at different points along the lunar surface for the same lunar phase and also for different lunar phase angles. Adopting a sodium sunlit surface source characterized by a 1000 K Maxwell Boltzmann velocity distribution and a $\cos\chi$ dependence and assuming 100% surface sticking for sodium atoms encountering the lunar surface, a model calculation for the Moon

at third quarter is shown in Figure 2. Sodium brightness profiles are compared above the equator (i.e., at $\chi = 0$ above the subsolar point) and above the pole (i.e., $\chi = \pi / 2$). The equatorial profile (dashed line) has a power law slope that falls off with radius as $r^{-4.4}$ and is steeper than the polar profile (solid line) that falls off with radius as $r^{-3.3}$. This rather small reduction in the power law index as one moves from the equator to the pole is similar to results obtained by Flynn and Mendillo (1995) for a $\cos\chi$ dependence source. The observed subsolar profile with a power law index of -4 at first or third quarter is readily produced for the $\cos\chi$ dependence source, as noted by Flynn and Mendillo (1995), by slightly increasing the temperature of the Maxwell-Boltzmann distribution in the model calculation. Adopting the same sodium source, a model calculation is shown in Figure 3 that compares the equatorial profile at first quarter and at full Moon. The equatorial profile at first quarter (solid line) has a power law index of -4.4, similar to the equatorial profile at first quarter in Figure 2. The equatorial profile at full Moon (dashed line) in Figure 3 has a slope that changes near 5 R_L with a power law index of about -3.7 between a radial distance of 1 and ~5 R_L and a power law index of about -2 between a radial distance of ~5 and 10 R_L. This power law index of -3.7 between radial distances of 1 and 5 R_L at full Moon is a bit steeper than the polar profile in Figure 2 with a power law index of -3.3 at third quarter. At full Moon in Figure 3, the smaller slope of the profile between radial distances of 5 and 10 R_L that falls off as about r^{-2} is due to upstream sodium atoms flowing downstream in the nearly anti-sunward direction because of the action of solar radiation acceleration on upstream sodium atoms in the dayside atmosphere, as illustrated by Smyth and Marconi (1995b). At larger radial distances (> 5 R_L), this downstream sodium atom population created by solar radiation acceleration is then at least one way of producing a distinct difference in the slopes of the polar profile at first (or third) quarter and the equatorial profile at full Moon.

Near Image of Lunar Sodium Atmosphere

Model calculations have been performed to study the sodium image for the sodium D_2 emission line brightness in Figure 1. Several comparisons of the observed image and model calculated brightness profiles for the lunar sodium brightness are shown in Figures 4a, 4b, and 5. These comparisons are discussed separately below. The source rates from these model calculations are summarized in Table 1 with the average sodium flux on the sunlit hemisphere ranging from 2.8×10^5 to 8.5×10^5 cm^{-2} s^{-1}. These average sodium fluxes are similar to the range of values of 3.5×10^5 to 2.1×10^6 cm^{-2} s^{-1} determined by Smyth and Marconi (1995b) from modeling analysis of only equatorial sodium brightness profiles.

In Figure 4a, the equatorial (i.e., subsolar) profile for the observed image (solid line) extracted from Figure 1 is shown for altitudes from ~100 to 1440 km. The dashed line is a

baseline model calculation for a 1000 K Maxwell-Boltzmann sodium source speed distribution that is uniform on the sunlit hemisphere. For the baseline model, the sodium atoms are assumed to have 100% surface sticking when they encounter the surface. The dot-dash line is a model calculation for the new electron-stimulated desorption source speed distribution of Yakshinskiy and Madey (1998) assuming a sunlit hemispherical source with a cosine dependence on the solar zenith angle. For this model calculation, the thermal accommodation of sodium to the lunar surface is assumed to be 100% (Madey 1999), and the surface sticking is assumed to depend upon the surface temperature according to new information provided by Yakshinskiy (1999) and following the fit [min(1,1.457*exp(-1.2835*(TEMP of surface)/300))]. This fit for the temperature dependent sticking coefficient more or less threads the laboratory data (Yakshinskiy 1999), has a value of 1.0 at about 140 K, and approaches 0.0 at high temperatures. Both model curves in Figure 4a provide a good fit to the observation except within an altitude of a few hundred kilometers of the surface (where the occulting mask may alters the data) and beyond an altitude of about 1200 km (where the signal to noise become problematic because the reliability of the data at these distances is compromised by the background subtraction). Another model calculation (not shown) similar to the dot-dash case except that it assumes a source with a cosine cube power dependence on the solar zenith angle was undertaken and produced a fit very similar to the dot-dash case. The overestimate of the model brightness within an altitude of ~200-300 km of the surface could reflect a smaller population than assumed here for sodium atoms in the source speed distribution at speeds below 1 km s^{-1}. A model brightness profile (see second-year annual report) that undercuts the observed profile at altitudes below 500 km and provides a similarly good fit to the observed brightness profile for altitudes above 500 km can be easily constructed for a sodium source that is a 1000 K Maxwell-Boltzmann speed distribution truncated (i.e., eliminated) below 1.25 km s^{-1} and that has a $\cos\chi$ dependence on the sunlit hemisphere. In Figure 4a, the source rates for the baseline model and the electron-stimulated desorption source model are, respectively, 1.2×10^{23} atoms s^{-1} and 8.3×10^{22} atoms s^{-1} and correspond to average sunlit hemispherical surface fluxes of 6.6×10^{5} atoms cm^{-2} s^{-1} and 4.4×10^{5} atoms cm^{-2} s^{-1}. For the electron-stimulated desorption source model with a cosine cube power dependence on the solar zenith angle (not shown in Fig. 4a), the source rate was 6.3×10^{22} atoms s^{-1}, slightly lower as expected, and corresponds to an average sunlit hemispherical surface flux of 3.3×10^{5} atoms cm^{-2} s^{-1}.

In Figure 4b, brightness profiles are compared south of the equator along a line parallel to the equator and 718 km vertical below the equator. The zero on the horizontal distance scale corresponds to a distance of 155 km above the surface. The solid line is the observed profile extracted from Figure 1, the dashed line is a model calculation with the baseline model used in Figure 4a, and the dash-dot line is a model calculation for the same electron-stimulated desorption

source speed distribution and surface conditions assumed in Figure 4a. Both model calculations provide very good fits to the observation, with the electron-stimulated desorption source (dash-dot line) being slightly better. In Figure 4b, the source rates for the baseline model and the electron-stimulated desorption source model are, respectively, 1.7 x 10^{23} atoms s^{-1} and 1.4 x 10^{23} atoms s^{-1} and correspond to average sunlit hemispherical surface fluxes of 8.9 x 10^{5} atoms cm^{-2} s^{-1} and 7.5 x 10^{5} atoms cm^{-2} s^{-1}. The source rates in Figure 4b are a little higher than for the corresponding sources in Figure 4a because of north-south asymmetries in the limb brightness (i.e., the limb brightness is larger south of the equator; see Figure 5 and discussions below).

A comparison of the observed image and model brightness profiles as a function of latitude is presented in Figure 5 for an altitude of ~110 km. The solid line is the observed brightness extracted from Figure 1. The dot-dash line is the model calculated brightness for the electron-stimulated desorption source of 5.3 x 10^{22} atoms s^{-1} (an average sunlit hemispherical surface flux of 2.8 x 10^{5} atoms cm^{-2} s^{-1}) with a hemispheric sunlit surface source which varies as cube of the cosine of the solar zenith angle. The model fit seems quite good except near the edges (particularly on the northern limb and to some extent on the southern limb) where the observed brightness suddenly cease to decrease and actually jumps. These brightness jumps are problems in the image brightness produced near the outer edge of the observing aperture. A model calculation (not shown) for a hemispheric sunlit surface source which varies as the $\cos^2 \chi$ and for a 1000 K Maxwellian with an atom-surface sticking coefficient of 100% provides a similar and only slightly poorer fit for a source of 5.6 x 10^{22} atoms s^{-1}. The image brightness in Figure 1 is not symmetric with respect to the north and south hemispheres. If the north-south asymmetry is real, the lunar source may be more complex than the simple hemispherical sources assumed here. If the brightnesses near the edge of the observed image are inaccurate, the fall off in the source strength with solar zenith angle may not be more rapid than the $\cos^2 \chi$ law in the latter model calculation.

Sodium Brightness Variations with Lunar Phase

Model calculations have been performed to explore if the variation of sodium brightness with lunar phase (as discussed in Section 3.1) may be simply a geometric effect produced by viewing the spatially asymmetric atmosphere at different angles relative to the sun-planet line. In Figure 6, the model calculated equatorial brightness of sodium ~35 km above the surface (solid line) is compared as a function of lunar phase angle with the various observed brightnesses (+ symbols) reported by Potter and Morgan (1994). For the model calculation, a hemispheric sunlit surface source is adopted which varies as the $\cos^4 \chi$ and is characterized by a 1000 K Maxwellian. An atom-surface sticking coefficient of 100% is assumed. The vertical dotted line delineates the lunar phases where the Moon was within the Earth's magnetospheric-tail cavity and

hence shielded from the solar wind. The scatter in the observed brightnesses reflects intrinsic variability of the source and the different altitudes (10 to 70 km) of the data. The simple geometric changing viewing direction of the spatially asymmetric atmosphere in the model appears, therefore, to reasonably well fit the average behavior of the observed brightness without any need to postulate, as did Potter and Morgan (1994), that the reduction of brightness is produced by a reduction in solar wind sputtering of the lunar surface when the Moon is within the Earth's magnetospheric-tail cavity. Because of the large scatter of the observations in Figure 6, a better determination of the observed angular dependence could be accomplished by the independent examination of the behavior of the observed brightness variation for different sets of observations, each acquired over a period of several nights.

IV. FURTHER STUDIES FOR MERCURY

4.1 Observational Data

Images of the Sodium and Potassium Atmospheres on the Planetary Disk

Images of the sodium brightness in both the D_2 (5890 Å) and D_1 (5896 Å) emission lines over a significant fraction of the area above the planetary disk were first measured by Potter and Morgan (1990). The brighter D_2 images, one acquired in 1988 (11 November) and five acquired in 1989 (16, 17, 18 February; 7 July; 23 August), were published (Potter and Morgan 1990) and illustrated that excess sodium emission was generally localized at higher northern and southern latitudes and that the spatial brightness pattern across the disk was time variable from day to day. These enhanced brightnesses of the images at higher northern and southern latitudes has lead to the suggestion by Potter and Morgan (1990) of a strong source mechanism for magnetospheric ion sputtering of the surface in the magnetospheric cusp regions of the planetary magnetic field which are located at higher north and south latitudes on the sunlit hemisphere (Luhmann et al. 1998).

Same-day images of sodium in the D_2 (5890 Å) and D_1 (5896 Å) emission lines and potassium in the stronger D_2 (7665 Å) emission line were acquired on 5 consecutive days (6-10 December) in 1990 by Potter and Morgan (1997a). These images showed that the sodium and potassium images were closely correlated in both their time variable intensity changes over the five day period as well as in their nonuniform spatial distribution over the planetary disk, with enhanced emission brightness occurring in the southern hemisphere. Peak intensities for both sodium and potassium were observed to increase by about a factor of two over the five days while the solar radiation acceleration increased only by a factor of ~15%. This implies that other factors were changing over this period and that the source mechanism for both sodium and potassium were similar in nature.

Sodium images in both the D_2 (5890 Å) and D_1 (5896 Å) emission lines have also been obtained in 1997 on the six days of November 13, 14, 15, 16, 18 and 20 using a new 10 x 10 arc seconds aperture image slicer coupled to a high-resolution spectrograph. These sodium images have been recently reduced and corrected (Potter et al. 1999) for the significant smearing caused by the terrestrial atmosphere by using a new Fourier transform deconvolution technique based on a computed Hapke reflection image and the observed surface reflection continuum image acquired simultaneously with the sodium image. During this period of observations, the images show that both the spatial distribution of sodium changes significantly across the planetary disk and that the total sodium atom population in the atmosphere increases by a factor of ~3. The sodium emission was generally brightest in the vicinity of the subsolar point with time varying excess sodium occurring near the subsolar meridian, sometimes at northern latitudes and sometimes at southern latitudes. Over the period of the observations, the solar radiation acceleration experienced by sodium atoms in the atmosphere increased by a factor of two, from ~61 to 122 cm s^{-2}. This change would not likely cause the increase seen in the sodium population. The cause of the increase is not known but it might be related to changes in solar activity and, in particular, to coronal mass ejection events that were reported to occur during the first two days of the observing period. Such events would be expected to distort severely or overwhelm the magnetopause morphology near the subsolar point (Luhmann et al. 1998) and thus significantly alter the interaction of the solar wind with the planetary surface (Potter et al. 1999).

Sodium and Potassium Column Abundance Changes for the Same Earth-Mercury Geometry

The column abundance ratio of Na to K was estimated by Potter and Morgan (1997a) to be 190 for the December 1990 observations, which occurred at a time of solar maximum. This column abundance ratio was about a factor of two larger than their earlier November 16, 1985 measurements (Potter and Morgan 1986) with a value of 80, which were acquired for the same relative geometry of Mercury and the Earth, but near solar minimum. Potter and Morgan (1997a) suggested that the change in the column abundance ratio was because of a relative change in the potassium ionization lifetime compared to the sodium lifetime produced because of a significant increased in the solar ultraviolet flux during the solar maximum time frame. The photoionization lifetimes of sodium and potassium are, however, determined primarily by photons near the threshold wavelengths (~3000 to 2000 Å) where the solar flux is very stable in time and not by the higher energy solar ultraviolet photons where the photoionization cross sections are very small. Consequently, the photoionization lifetimes of both sodium and potassium change only by about 5% from quiet to active solar conditions (Huebner et al. 1992) and hence cannot affect the relative column abundance of sodium and potassium in their observation.

What does noticeably increase, however, from the November 16, 1985 observations to the December 9, 1990 observations is the absolute column abundance of both sodium and potassium. The sodium column density changes from 1.3 x 10^{11} atoms cm^{-2} to values in the range from 4.5 to 6 x 10^{11} atoms cm^{-2} which is a factor of about 4 while the potassium column density changes from a value of ~1.6 x 10^9 atoms cm^{-2} (1/80 of the sodium column density) to values in the range from 2.1 to 4.6 x 10^9 atoms cm^{-2} which is a smaller factor of only ~1.3 to 2.8. This smaller change in the potassium column by the factor of about two or less might be due to other factors. One likely factor is that there may be a difference in the relative abundance of sodium and potassium in the surface composition observed on the two dates. Although the relative geometry of Mercury and the Earth for the two dates is the same, the observed surfaces are opposite hemispheres of Mercury. This can be seen by noting that the time interval between November 16, 1985 and December 8, 1990 is 1848 days, which corresponds to 21 (an odd number of 88 days orbital) periods of Mercury. Since there is 3:2 resonance between the satellite rotation period and the orbital period of the planet, an odd number of planetary periods means that the opposite hemisphere of Mercury is seen on the two dates for the same Mercury-Earth observing geometry since Mercury has rotated (3/2) x 21= 31.5 times. On the Moon, the surface composition of potassium is known to change by an order of magnitude in longitude while that for sodium is relatively constant, varying by only a factor of two. Hence it is very plausible that the smaller relative abundance of potassium on the hemisphere observed in December 1990 is caused by a difference in the surface composition between the two opposite hemispheres of the planet. A second factor that may also contribute to the change in the Na to K ratio involves an optical depth effect present for the sodium emission lines but not for the potassium emission line. The substantial increase in the sodium intensity in December 1990 should correspond to a more optically thick sodium column and hence should locally shield more sodium atoms in the atmosphere from the direct sunlight and therefore significantly reduce any large radiation acceleration driven loss to the night side. For potassium, the radiation acceleration driven loss to the night side will be unaltered since it is always optically thin. The net effect will be to effectively increase the sodium to potassium column density.

Images of the Sodium Atmosphere Substantially above the Planetary Surface

Recently Potter and Morgan (1997b) measured images of the sodium brightness in both the D_2 (5890 Å) and D_1 (5896 Å) emission lines from the atmosphere of Mercury that incorporated spatial regions well above the limb. Observations acquired on three days (20-22 July) in 1994 detected sodium up to a planetary radius above the north and south poles, with the peak emission intensity seen above the north pole on July 20 moving to a position well above the south pole on

July 22. This time variable behavior supports the idea of an ion sputtered source mechanism at the magnetic cusp regions of the planet. In contrast, observations acquired on October 24, 1995 were almost completely uniform over the planetary disk and extended well beyond the disk in all directions. For the October 24, 1995 observations, the summed D_2 plus D_1 brightness image indicated for the first time the two-dimensional nature of the sodium atmosphere thousands of kilometers above the planetary surface. The very strong effects that solar radiation acceleration played in shaping the atmosphere into an asymmetric comet-like coma with a tailward shadow region were clearly visible and may be similar to model calculations shown earlier by Smyth and Marconi (1995a) if the sodium atoms are hot enough to populate these spatial regions directly. The extension of the sodium atmosphere to distances of a planetary radius along the subsolar direction places the gas well in front of the magnetopause (nominally located at an altitude of ~0.6 planetary radii) so that a significant fraction of the sodium will be lost upon undergoing photoionization in the solar wind. Such a behavior was also illustrated for strong radiation acceleration in earlier model calculations of Smyth and Marconi (1995a).

For the October 24, 1995 sodium observation, the constructed D_2 plus D_1 emission brightness profile was analyzed by Potter and Morgan (1997b) along the subsolar direction using a simple barometric function that included as an increase to the planetary gravity the large solar radiation acceleration of sodium atoms of 175 cm sec^{-2}. They estimated a sodium source temperature of 6500 K, a sodium concentration at the surface of ~500 atoms cm^{-3}, and a column density of ~5×10^{11} atoms cm^{-2}. These source atoms are suprathermal in that they are about an order of magnitude more energetic than the surface temperature (~700 K maximum at perihelion). Preliminary model calculations for these sodium observations of Mercury are presented below in Section 4.2 and give similar results.

The problem with this interpretation is that the sodium brightness well above the limb may be due partially and even entirely to the significant terrestrial atmospheric smearing of sodium emissions that otherwise resides primarily or wholly only on the planetary disk of Mercury. The extended atmosphere may thus be produced artificially and hence not exist in reality. This was one of the reasons for extending this project into a (no-cost) fourth year. The more recent sodium image observations of November 13-20, 1997 (see discussed above), reduced using a new Fourier transform technique to remove atmospheric smearing, essentially show little or no significant emission off the disk at the spatial resolution of 350 km/pixel. Because at present this question of extended off-disk emission remains unanswered, primary efforts here have been focused to investigate these new deconvolution sodium images and postpone the extended atmosphere issue

for later resolution. Preliminary model calculations for these deconvolution sodium images are presented below in Section 4.2.

4.2 Modeling Analysis for the Sodium Atmosphere

Modeling the Sodium Images Substantially above the Planetary Surface

Preliminary model calculations for the D_2 plus D_1 sodium image obtained by Potter and Morgan (1997b) well above the planetary surface discussed in Section 4.1 have been undertaken. A model calculation for an isotropic surface source with a 7000 K Maxwellian with no surface sticking and complete surface accommodation is shown in Figure 7. The intensity was calibrated by roughly aligning the contour for the 2000 Rayleighs with the sodium brightness contour plot of the observed image. While the overall brightness appears similar near the subsolar point, which is at about 45 degrees in the plot (i.e., along the symmetry axis of the contours), the model appears to be too dim for directions perpendicular to the Sun-planet line (i.e., perpendicular to the symmetry axis of the contours). Potter (1997) has indicated that the image contours are artificially inflated in this direction and should not be taken literally. In addition, the model predicts an excessively large brightness very near the disc of Mercury. This may be due to the failure to account for optical depth effects in the model. In Figure 8, the brightness profile (solid line) is shown along the subsolar line between 1800 to 5500 km above Mercury's surface for the model calculation in Figure 7 and is compared to the observation (* symbols). The agreement is quite good, strongly suggesting that 7000 K is a good measure of the mean energy of the sodium at Mercury if atmospheric smearing is not responsible for the sodium brightness substantially above the planetary disk. This temperature corresponds to a Maxwellian flux distribution for sodium that peaks at 2.25 km/sec. This large velocity and the higher temperature suggest that an ion sputtering source and/or a micro-meteoroid source are likely important sources for the sodium atmosphere. The more recent images acquired on November 13-20, 1997, which are discussed below and corrected for atmospheric smearing, however, show no appreciable sodium brightness above the disk and bring into question the existence of any substantial sodium population far above the disk.

Modeling the Sodium Images on the Planetary Disk

Preliminary assessment and modeling analysis have been performed for six sodium D_2 emission image observations acquired in 1997 on the six days of November 13, 14, 15, 16, 18 and 20 and subsequently spatially deconvolved (as discussed above) by Potter et al. (1999). The deconvolved images are shown in Figure 9 where the D_2 emission brightness in kiloRayleighs is represented by color-coded pixels that are 0.5 x 0.5 arc seconds (~350 x 350 km) in size. Each image for a particular day was constructed from the addition of several short-exposure (40-60 s)

images acquired on that day in order to improve the signal to noise. To obtain a quantitative measure of the brightness distribution and time dependence of these images over this observing period, a north-south profile located at half the distance between the center of the planetary disk and the subsolar limb and an east-west brightness along the equator containing the subsolar point were extracted from each image and are shown, respectively, in Figures 10a and 10b. The north-south profiles in Figure 10a all have an approximately trapezoidal-like shape with a similar north-south-base width and a variable height (in brightness) that increase from the first image (November 13) to the last image (November 20) by about a factor of five. The east-west profiles in Figure 10b have a triangular-like shape with a comparable east-west base and a variable height (in brightness) that increase from the first image (November 13) to the last image (November 20) by about a factor of five. A much smaller emission brightness exists beyond the terminator and could represent bound and escaping sodium above the terminator shadow line but is near the noise level and must be treated with caution (Potter 1999). The absence of expected limb enhancements in the form of sharply defined spikes at the north and south limbs in Figure 10a and the subsolar-ward limb in Figure 10b may be due to (1) atmospheric smearing, (2) the Fourier transform inversion technique adopted for deconvolution, and (3) the 0.5 x 1.0 arc second pixel sizes of the new 10 x 10 arc seconds aperture image slicer. Additional investigation beyond this project will be required to address the combined effects of these three factors on limb enhancement.

Model calculations have been undertaken to explore the spatial distribution and time dependent brightness increase of the profiles in Figures 10a and 10b. In the model, the observed brightness distribution will physically depend upon the combined effects of a number of factors for (1) the source velocity distribution, (2) the sodium photoionization sink, (3) the gas random-walk and solar-radiation-acceleration driven transport of the gas across the surface, and (4) various gas-surface interactions. A theoretical overview of these factors has been discussed in detail in the paper by Smyth and Marconi (1995a) in Appendix A. For all model calculations presented in this subsection for Mercury's sodium atmosphere, a new source velocity distribution recently determined for electron-stimulated desorption based upon laboratory studies of Madey and Yakshinskiy (1998; Yakshinskiy and Madey 1998; Yakshinskiy 1999) has been adopted. This new source velocity distribution, thought to apply equally well for photon-stimulated desorption (Yakshinskiy and Madey 1998; Yakshinskiy 1999), is very similar in shape to a Maxwell-Boltzmann source velocity distribution with a temperature of ~1000 K. Model calculations presented below differ only in the absolute source rate and the surface area on Mercury assumed for this sodium source. A number of the sodium source areas and rates for these model calculations are summarized in Table 2 with the average sodium fluxes, surprisingly, having very similar values to those for the lunar sodium atmosphere in Table 1 and the total sodium source rates

at the Moon being larger due to the larger effective surface source area available at the Moon. For the sodium photoionization sink, a new larger lifetime value (Verner at al. 1996) of 1.83 x 10^5 s (50.8 hr) at 1 AU has been adopted and is based upon theoretical calculation of Na photoionization cross-sections (Chang and Kelly 1974; Dasgupta and Bhatia 1985). This new value is about a factor of 3 longer than an earlier adopted sodium photoionization lifetime of ~15 hr at 1 AU based upon the measurements of Hudson and Carter (1967). This discrepancy has recently been have attributed by Seaton et al. (1992) to experimental error. Using this new lifetime value, the sodium lifetime at Mercury's orbital position for the observations in Figure 9 varies from 10.2 hr (November 13) to 8.93 hr (November 20). The treatment for the random-walk and solar-radiation-acceleration driven transport of the sodium atoms across the surface of Mercury adopted here is described in Appendix A. For the gas-surface interactions for sodium atoms, a thermal accommodation coefficient of 0.5 is adopted, a preferred valued suggested from modeling by Smyth and Marconi (1995a, in Appendix A), and a sticking coefficient of 0.2 is adopted as recently suggested by Yakshinskiy (1999) for temperatures of ~500 K, similar to those of the surface of Mercury for the observations in Figure 9.

For the observation on November 20, model calculations are presented in Figures 11a and 11b and compared to the observed profiles, where a total sunlit hemispherical sodium source of 1.31 x 10^{24} atoms s^{-1} is assumed with a cosine angular fall-off dependence from the subsolar point. For this model calculation, the total number of atoms in the atmosphere is 1.37 x 10^{28} and the average surface source flux is 3.50 x 10^6 cm^{-2} s^{-1} (see summary in Table 2). In Figure 11a, the calculated north-south profile (solid line) has a similar width to the observational profile (dashed line) but exhibits a very different brightness distribution. The model profile has brightness spikes at both the north and south limbs and a much lower and minimum brightness value located at the equator. In Figure 11b, the calculated east-west profile (solid line) has a similar horizontal width to the observational profile (dashed line) but exhibits a very different brightness distribution. The model profile has a brightness spike at the subsolar-ward limb that is much too high and not present in the observation, and a brightness level between the subsolar point and the terminator that is flat (not triangular-shaped like the observation) and much too low. The absence of limb enhancements in the observational profiles, as discussed earlier, could be reduced or possibly eliminated by the combination of instrumental spatial resolution, atmospheric seeing, and the Fourier transform deconvolution technique. If, however, the image distribution is taken at face value, the absence of significant limb enhancements suggests that the sodium source should be more spatially confined near the subsolar point.

Model calculations for the observation on November 20 are therefore undertaken and shown in Figures 12a and 12b for a "bulls-eye" sodium source of 7.48 x 10^{22} atoms s^{-1} that is confined to an angular interval that is 30° from the subsolar point and has an assumed cosine angular fall-off dependence from the subsolar point. For this model calculation, the total number of atoms in the atmosphere is 1.05 x 10^{28} and the average surface source flux is 1.49 x 10^{6} cm^{-2} s^{-1} (see Table 2). For the north-south profile in Figure 12a, this more confined surface source significantly reduces the model calculated (solid line) enhanced peaks near and at the north and south limbs and increases the minimum brightness at the equator, producing a much better fit to the observational profile (dashed line) than in Figure 11. In Figure 12b, the model calculated east-west profile still exhibits a thin brightness spike at the subsolar-ward limb (because of the close proximity of the source region to this limb) that is not seen in the observed profile. In the spatial interval between the subsolar point and the terminator, the model profile now has a more triangular shape but it is still significantly below the observational profile brightness. This improvement in the model profile suggests that a source that is more concentrated in the north-south direction near the subsolar point and that is distributed in the east-west direction more toward the terminator side of the subsolar point should be more appropriate.

Model calculations for the observation on November 20 are therefore undertaken and shown in Figures 13a and 13b for a more complex surface area for the sodium source. This source area is confined to a 24° radius "bulls-eye" area centered upon the equator plus a north angular sector and a south angular sector both located on the meridian line tangent to the sunward (west) side of the "bulls-eye" circle at the equator. The north and south sectors are located on this meridian, respectively, between 20 to 45° latitude north and between 20 to 45° latitude south. The south angular sector (top) has a longitudinal angular width of 25° (±12.5° about the meridian). The north angular sector (bottom) has a slightly smaller longitudinal angular width of 22° (±11° about the meridian), creating a slight north-south asymmetry. The center of the "bulls-eye" is offset from the subsolar point by 24° longitude toward the terminator. The total source in this area is 5.84 x 10^{22} atoms s^{-1} with an assumed cosine angular fall-off dependence from the subsolar point. For this model calculation, the total number of atoms in the atmosphere is 1.40 x 10^{28} and the average surface source flux is 1.45 x 10^{6} cm^{-2} s^{-1} (see Table 2). For the north-south profile in Figure 13a, this surface source produces a model calculated (solid line) profile that provides an excellent fit to the observational profile (dashed line). In Figure 13b, the model calculated east-west profile now has no significant spike at the subsolar-ward limb (because of the farther proximity of the source region from this limb) and provides an excellent fit to the triangular brightness pattern in the spatial interval between the subsolar point and the terminator. The corresponding north-south and east-west profiles for the sodium column density are presented in

Figures 14a and 14b. In Figure 14a, the column density in the north-south profile is rather flat with a nominal value that is near ~1.6 x 10^{11} cm^{-2} and everywhere less than 2 x 10^{11} cm^{-2}. Along the east-west profile in Figure 14b, the column density is furthermore seen to decrease by a factor of ~4 from this peak as one moves toward the terminator. This maximum value of the column density and its associated D_2 emission brightness of 4-5 MR in Figure 13 correspond to an optically thin sodium column. Therefore, these sodium observations for Mercury do not require, as originally proposed in our collaboration with Dr. R. M. Killen, a radiative transfer inversion to deduce the column density from the brightness distribution.

The observed brightness profiles on November 20, which have the largest absolute brightness for the six images in Figure 9 and are still optically thin, can therefore be accurately reproduced with a surface sodium source that is concentrated and somewhat asymmetrically distributed about the subsolar point. This suggests that a suitably constructed asymmetric sodium source near the subsolar point may also be able to fit all of the other profiles in Figure 10. For the observed profiles on November 13, which has the smallest absolute brightness for the six images in Figure 9, such a model fit is illustrated in Figures 15a and 15b. For this calculation, a sodium surface source of 1.51 x 10^{22} atoms s^{-1} was assumed from the same source area assumed in Figure 13 except that the center of the "bulls-eye" is off-set from the subsolar point by only 11°. The model calculation provides a good fit for both the observed north-south profile in Figure 14a and the observed east-west profile in Figure 14b and could be improved and refined by the addition of minor asymmetric adjustments to the source area.

In comparing the model calculation for the dimmest profiles on November 13 and the brightest profiles on November 20, the sodium sources have (1) the same surface area, only 11.7 % of the area of the sunlit hemisphere, (2) significantly different longitudinal offsets relatively to the subsolar point, and (3) an average flux that increases by a factor of ~4.2, from a value of 3.46 x 10^5 to 1.45 x 10^6 atoms cm^{-2} s^{-1}. During this time interval, the total number of atoms in the modeled atmosphere have increased by a factor of ~2.5, from 5.56 x 10^{27} to 1.40 x 10^{28}. Other model calculations using slightly different surface source area distributions were also able to provide reasonable and simultaneous fits to the observed north-south and east-west profiles, but these source areas were always similar in shape and asymmetrically distributed about the subsolar point. This small sunlit hemispheric source area near the subsolar point and this large enhancement in the source strength provide profound constraints on the nature of the sodium source mechanism for the atmosphere of Mercury. The analysis of additional sodium image observations for Mercury's atmosphere (already acquired by A. E. Potter) is therefore recommended and is of fundamental importance in confirming this source pattern and in studying the source mechanism.

REFERENCES

Chang J.J. and Kelly, H.P. (1974) Phys. Rev. A 12, 92-98.

Dasgupta A and Bhatia J. (1985) Phys. Rev. A 31, 759-771.

Flynn, B. and Mendillo, M. (1993) A Picture of the Moon's Atmosphere, Science 261, 184-186.

Flynn, B. and Mendillo, M. (1995) Simulation of the Lunar Sodium Atmosphere, J. Geophys. Res. 100, 23271-23278.

Hudson R.D. and Carter, V.L. (1967) Atomic Absorption Cross Section of Lithium and Sodium between 600 and 1000 Å, Journal of the Optical Society of America 57, 651-654.

Huebner, W. F., Keady, J. J. and Lyon, S. P. (1992) Solar Photo Rates for Planetary Atmospheres and Atmospheric Pollutants, Kluwer Academic Publishers, Dordecht.

Luhmann, J. G., Russell, C. T. and Tsyganenko, N. A. (1998) Disturbances in Mercury's Magnetosphere: Are the Mariner 10 "Substorms" Simply Driven?, J. Geophys. Res. 103, 9113-9119.

Madey, T.E (1999) private communication.

Madey, T.E. and Yakshinskiy, B.V. (1998) Desorption of Alkali Atoms and Ions from Oxide Surfaces: Relevance to Origins of Na and K in Atmospheres of Mercury and the Moon, J. Geophys. Res 103, 5873-5887.

Potter, A. E. (1997) Private communication.

Potter, A. E. (1999) Private communication.

Potter, A. E. and Morgan, T. H. (1985) Discovery of Sodium in the Atmosphere of Mercury. Science, 229, 651-653.

Potter, A. E., and Morgan, T. H. (1986) Potassium in the Atmosphere of Mercury. Icarus, 67, 336-340.

Potter, A. E., and Morgan, T. H. (1988) Discovery of Sodium and Potassium Vapor in the Atmosphere of the Moon. Science, 241, 675-680.

Potter, A. E., and Morgan, T. H. (1990) Evidence for Magnetospheric Effects on the Sodium Atmosphere of Mercury, Science 248, 835-838.

Potter A. E. and T. H. Morgan (1994) Variation of Lunar Sodium Intensity with Phase Angle, Geophys. Res Letts. 21, 2263-2266.

Potter A. E. and T. H. Morgan (1997a) Sodium and Potassium Atmospheres of Mercury, Planet. Space Sci. 45, 95-100.

Potter A. E. and T. H. Morgan (1997b) Evidence for Suprathermal Sodium on Mercury Adv. Space Res. 19, 1571-1576.

Potter A. E. and T. H. Morgan (1998) Coronagraphic Observations of the Lunar Sodium Exospheree near the Lunar Surface, J. Geophys. Res. 103, 8581-8586.

Potter A. E., Killen, R. M. and T. H. Morgan (1999) Rapid Changes in the Sodium Exosphere of Mercury, preprint.

Seaton, M.J., Zeippen, C.J., Tully, J.A. Pradhan, A.K. Mendoza, C., Hibbert, A. and Berrington, K.A. (1992) Rev. Mexicana Astron. Astrof. 23, 19-43.

Smyth, W. H. and Marconi, M. L. (1995a) Theoretical Overview and Modeling of the Sodium and Potassium Atmospheres of the Moon, Ap. J. 443, 371-392.

Smyth, W. H. and Marconi, M. L. (1995b) Theoretical Overview and Modeling of the Sodium and Potassium Atmospheres of Mercury, Ap.J. 441, 839-864.

Verner D.A., Ferland, G.J. Korista, K.T. and Yakolev, D.G. (1996) Ap.J.465, 487-498.

Yakshinskiy, B.V. (1999) private communication.

Yakshinskiy, B.V. and Madey, T.E. (1998) Desorption of Na from SiO_2 Film, Induced by Low Energy Electrons: Relevance to Atmospheres of Mercury and the Moon, BAAS 30, 1110-1111.

Table 1
Lunar Sodium Source Determined from the Coronagraph D_2 Emission Image

	Solar Zenith Angle Dependence	Total Source (atoms s^{-1})	Average Flux (atoms cm^{-2} s^{-1})
1. Equatorial Profile (100-1440 km)			
• Baseline Model	$\cos^0 \chi$	1.2×10^{23}	6.6×10^5
• ESD Source Model	$\cos^1 \chi$	8.3×10^{22}	4.4×10^5
• ESD Source Model	$\cos^3 \chi$	6.3×10^{22}	3.3×10^5
2. Profile 718 km South Parallel to Equator			
• Baseline Model	$\cos^0 \chi$	1.7×10^{23}	8.9×10^5
• ESD Source Model	$\cos^1 \chi$	1.4×10^{23}	7.5×10^5
3. Latitude Profile			
• Baseline Model (+$\cos^2 \chi$ dependence)	$\cos^2 \chi$	5.6×10^{22}	3.0×10^5
• ESD Source Model	$\cos^3 \chi$	5.3×10^{22}	2.8×10^5

Table 2
Model Calculation for Mercury's Sodium Atmosphere: Atom Source and Population

Observation Date	Subsolar Source Description[a]	Total Source (atoms s^{-1})	Source Area $\left(2\pi R_M^2\right)^b$	Average Flux (atoms $cm^{-2} s^{-1}$)	Average Column Density[c] (atoms cm^{-2})	Total Number of Atoms
Nov. 13	offset "bulls-eye" + N & S sectors[d]	1.51×10^{22}	0.117	3.46×10^{5}	2.58×10^{10}	5.56×10^{27}
Nov. 20	sunlit hemisphere	1.31×10^{24}	1.000	3.50×10^{6}	6.66×10^{10}	1.37×10^{28}
Nov. 20	centered 30° "bulls-eye"	7.48×10^{22}	0.134	1.49×10^{6}	5.48×10^{10}	1.05×10^{28}
Nov. 20	offset "bulls-eye" + N & S sectors[e]	5.84×10^{22}	0.117	1.45×10^{6}	7.31×10^{10}	1.40×10^{28}

a. The source rate for all source areas varies as the as the cosine of the solar zenith angle.

b. Hemispherical surface area of Mercury $\left(2\pi R_M^2\right)$ is 3.738×10^{17} cm^2.

c. The average column is calculates based upon a disk area πR_M^2.

d. 24° radius "bulls-eye" area centered upon the equator plus a north angular sector and a south angular sector both located on the meridian line tangent to the sunward (western) side of the "bulls-eye" circle at the equator. The north and south sectors are located on the meridian, respectively, between 20 to 45° latitude north and between 20 to 45° latitude south. The south angular sector (top) has a longitudinal angular width of 25° (±12.5° about the meridian). The north angular sector (bottom) has a slightly smaller longitudinal angular width of 22° (±12.5° about the meridian), creating a slight north-south asymmetry. The center of the "bulls-eye" is offset from the subsolar point by 11° longitude toward the terminator.

e. Same source area as in "d" except that the center of the "bulls-eye" is offset from the subsolar point by 24° longitude toward the terminator.

FIGURE CAPTIONS

Figure 1. Image of Lunar Sodium in the D_2 Emission Line. This is an image of lunar sodium measured by Potter at UT 03:31 on April 22, 1994. South is up and north is down. The subsolar point is about 8.4 degrees above a horizontal line bisecting the image. The sodium source would appear to be a strong function of latitude and stronger in the southern hemisphere.

Figure 2. Comparison of the Polar and Equatorial Relative Brightness Profiles for Lunar Sodium at 3rd Quarter. The modeled calculated relative brightness profiles at the equator (dashed line) and at the pole (solid line) are compared for the Moon at 3rd quarter. The source is assumed to be a 1000 K Maxwellian with a strength which varies as the $\cos\chi$. The source is assumed to be entirely restricted to the sunlit hemisphere, and the lunar surface is taken to have a sticking coefficient of 100 %.

Figure 3. Comparison of the Relative Brightness of the Equatorial Profiles for Lunar Sodium at 1st Quarter and at Full Moon. At the equator, the modeled calculated brightness profiles of the Moon are compared at 1st quarter (solid line) and at full Moon (dashed line). In both cases, the source was assumed to be a 1000 K Maxwellian with a surface strength which varies as $\cos\chi$. The surface was characterized by sticking coefficient of 100 %.

Figure 4. Comparison of Observed and Model Calculated Brightness Profiles for the Lunar Sodium Atmosphere. The solid line is the observed profile in (a) at the equator and in (b) south of the equator along a line parallel to the equator and 718 km vertical below the equator, both of which are extracted from the image of lunar sodium in Figure 1. The observational data were rebinned from (256 x 256) to (64 x 64) to reduce noise. In (b), the zero on the horizontal distance scale corresponds to a distance of 155 km above the surface. The dashed line is for a baseline model calculation with 100% surface sticking and a 1000 K Maxwellian speed source of 1.2 x 10^{23} atoms s^{-1} in (a) and of 1.7 x 10^{23} atoms s^{-1} in (b) that is uniform on the sunlit hemisphere. The dot-dash line is a model calculation for the electron-stimulated desorption source speed distribution (Yakshinskiy and Madey 1998) of 8.3 x 10^{22} atoms s^{-1} in (a) and of 1.4 x 10^{23} atoms s^{-1} in (b) on the sunlit hemispherical surface with a cosine dependence on the solar zenith angle and a temperature dependent sticking coefficient and a thermal accommodation of 100% for sodium on the lunar surface.

Figure 5. Comparison of Observed and Model Brightness Profiles for Lunar Sodium as a Function of Latitude. The solid line is the image brightness at about 110 km above the surface extracted from the image of lunar sodium in Figure 1. The subsolar point is at ~8.4°. The dot-dash line is a model calculation for the electron-stimulated desorption source of 5.3 x 10^{22} atoms s^{-1} with a hemispheric sunlit surface source that varies as cube of the cosine of the solar zenith angle and a temperature dependent sticking coefficient and a thermal accommodation of 100% for sodium on the lunar surface.

Figure 6. Comparison of Model Calculated Equatorial Brightness for Sodium with Observational Data for Different Lunar Phase Angles. The + symbols are the sodium brightness for various observations near the lunar surface for different lunar phase angles from Potter and Morgan (1994). The solid line is the model calculated sodium brightness at about 35 km above the surface for a hemispheric sunlight surface source which varies as the fourth power of the cosine of the solar zenith angle and is characterized by a 1000 K Maxwellian. An atom-surface sticking coefficient of 100 % is assumed. The dotted line delineates the lunar phases where the moon was shielded by the Earth from the solar wind. The scatter in the data may be accounted by intrinsic variability of the source and the different altitudes of the data.

Figure 7. Model Calculated Contour Plots for Brightness of Mercury's' Sodium Atmosphere. A 7000 K Maxwellian isotropic source with no sticking and complete accommodation was generated for the October 24, 1995 observation of Potter and Morgan (1997b). The model intensity was calibrated by roughly aligning the contour for 2000 Rayleighs with the sodium brightness contour plot of the observed image. The subsolar point is at about 45 degrees in the plot (along the symmetry axis of the contours).

Figure 8. Model Data Comparison for Sodium along the Subsolar Line. The brightness profile (solid line) determined from the model calculation described in Figure 7 is compared to the image brightness (* symbols) along the subsolar line between 1800 to 5500 km above Mercury's surface.

Figure 9. Sodium D_2 Image Observations of Mercury's Atmosphere. The D_2 brightness of six images acquired from earth-based observations during the period November 13 to November 20,1997 by Potter et al. (1999) are shown as corrected for atmospheric seeing (see text). The small red dot denotes the position of the subsolar point. The locations of the planetary disk and the terminator are indicated as well as the north-south and east west orientation of the images on the sky plane.

Figure 10. Sodium D_2 Observed Brightness Profiles. For a location containing the subsolar point, six observed brightness profiles extracted from the images in Fig.9 are shown in (a) along the north-south direction and in (b) along the east-west direction. The profiles are labeled to identify their observed dates: November 13 by "a", November 14 by "b", November 15 by "c", November 16 by "d", November 18 by "e", and November 20 by "f". Also shown, as seen by an earth-based observer, are the location of the planetary equator in (a) and the range of locations of the subsolar point and the terminator in (b).

Figure 11. Comparison of Model and Observed D_2 Brightness Profiles for Mercury's Sodium Atmosphere on November 20, 1997. Model calculation (solid line) and observations (dashed line) from Fig. 10 are shown for the north-south brightness profile in (a) and for the east-west brightness profile in (b). The model calculation is based on a sunlit hemispheric sodium source for the electron-stimulated desorption source speed distribution (Yakshinskiy and Madey 1998) of 1.31 x 10^{24} atoms s^{-1} that is assumed to vary as the cosine of the solar zenith angle. Also shown, as seen by an earth-based observer, are the locations of the planetary equator in (a) and the subsolar point and the terminator in (b).

Figure 12. Comparison of Model and Observed D_2 Brightness Profiles for Mercury's Sodium Atmosphere on November 20, 1997. Model calculation (solid line) and observations (dashed line) from Fig. 10 are shown for the north-south brightness profile in (a) and for the east-west brightness profile in (b). The calculation for the electron-stimulated desorption source speed distribution (Yakshinskiy and Madey 1998) with a source strength of 7.48 x 10^{22} atoms s^{-1} is confined to a "bulls-eye" area centered at the subsolar point and extending up to a solar zenith angle of 30°. The source strength is assumed to vary as the cosine of the solar zenith angle. Also shown, as seen by an earth-based observer, are the locations of the planetary equator in (a) and the subsolar point and the terminator in (b).

Figure 13. Comparison of Model and Observed D_2 Brightness Profiles for Mercury's Sodium Atmosphere on November 20, 1997. Model calculation (solid line) and observations (dashed line) from Fig. 10 are shown for the north-south brightness profile in (a) and for the east-west brightness profile in (b). The model calculation assumes an electron-stimulated desorption source speed distribution (Yakshinskiy and Madey 1998) with a source strength of 5.84 x 10^{22} atoms s^{-1}. This source is confined to a 24° radius "bulls-eye" area centered

upon the equator plus a north angular sector and a south angular sector both located on the meridian line tangent to the sunward (western) side of the "bulls-eye" circle at the equator. The north and south sectors are located on the meridian, respectively, between 20 to 45° latitude north and between 20 to 45° latitude south. The south angular sector (top) has a longitudinal angular width of 25° (±12.5° about the meridian). The north angular sector (bottom) has a slightly smaller longitudinal angular width of 22° (±11° about the meridian), creating a slight north-south asymmetry. The center of the "bulls-eye" is offset from the subsolar point by 24° longitude toward the terminator. The source strength is also assumed to vary as the cosine of the solar zenith angle. Also shown, as seen by an earth-based observer, are the locations of the planetary equator in (a) and the subsolar point and the terminator in (b).

Figure 14. Model Calculated Column Density Profiles for Mercury's Sodium Atmosphere on November 20, 1997. The column density profiles corresponding to the model calculated brightness profiles in Fig.13 are shown for the north-south direction in (a) and for the east-west direction in (b).

Figure 15. Comparison of Model and Observed D_2 Brightness Profiles for Mercury's Sodium Atmosphere on November 13, 1997. Model calculation (solid line) and observations (dashed line) from Fig. 10 are shown for the north-south brightness profile in (a) and for the east-west brightness profile in (b). The model calculation assumes an electron-stimulated desorption source speed distribution (Yakshinskiy and Madey 1998) with a source strength of 1.51×10^{22} atoms s^{-1}. The source is confined to a 24° radius "bulls-eye" area centered upon the equator plus a north angular sector and a south angular sector as described in Fig. Caption 13 with the exception that the center of the "bulls-eye" is now offset from the subsolar point by 11° longitude toward the terminator. Also shown, as seen by an earth-based observer, are the locations of the planetary equator in (a) and the subsolar point and the terminator in (b).

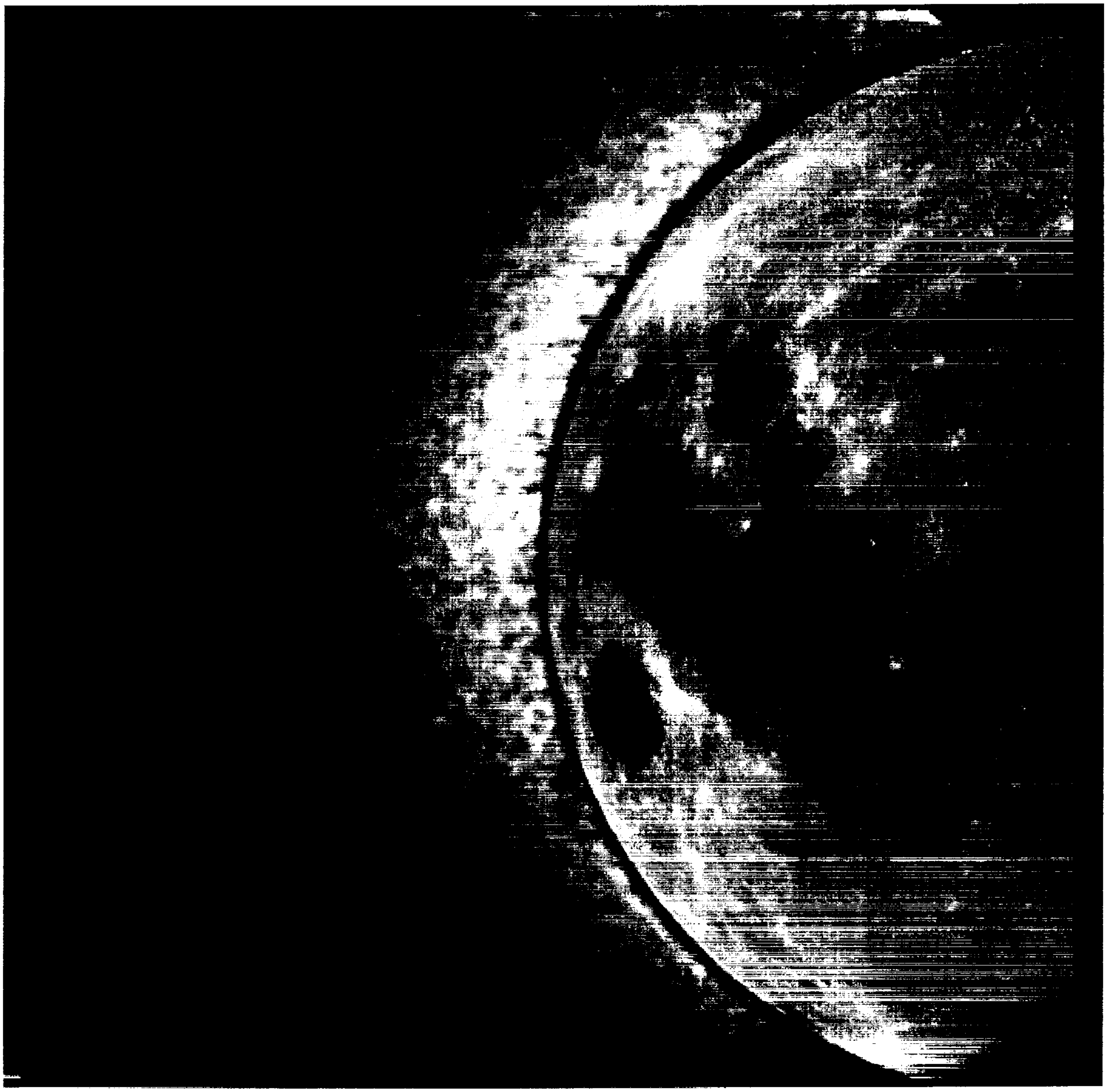

Figure 1

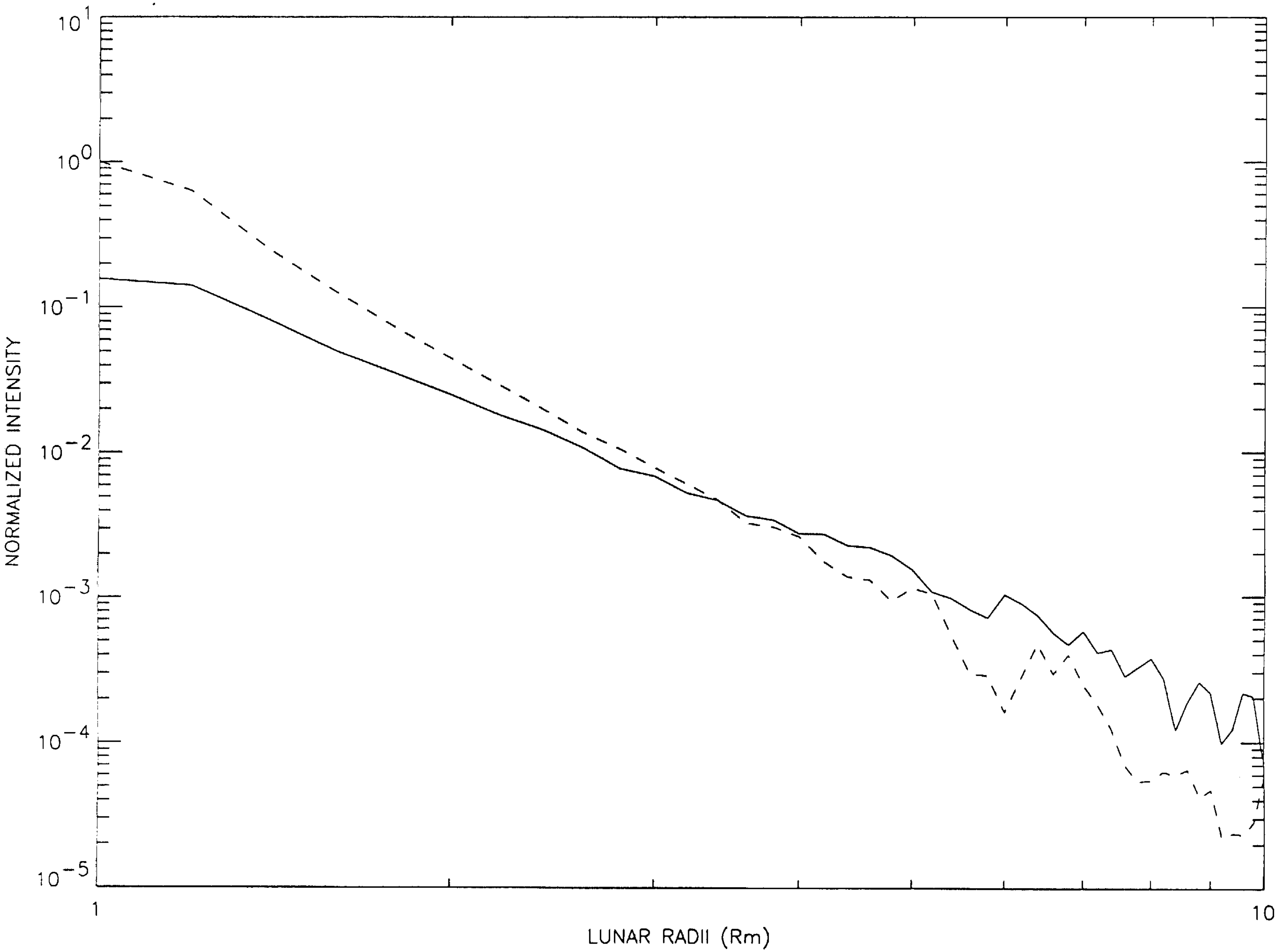

10^{1}
10^{0}
10^{-1}
10^{-2}
10^{-3}
10^{-4}
10^{-5}
NORMALIZED INTENSITY
1
10
LUNAR RADII (Rm)

Figure 2

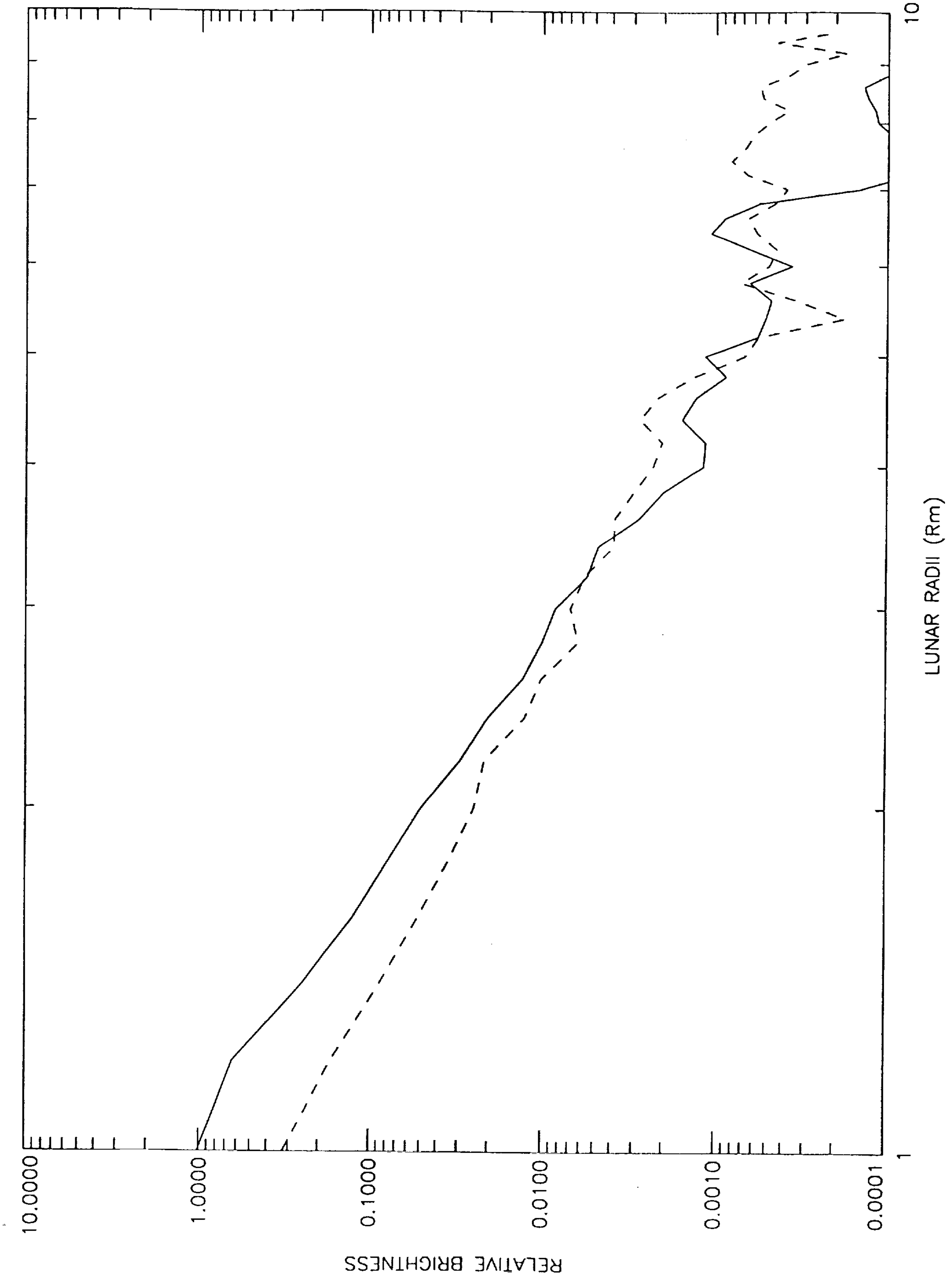
RELATIVE BRIGHTNESS
10.0000
1.0000
0.1000
0.0100
0.0010
0.0001
1
10
LUNAR RADII (Rm)

Figure 3

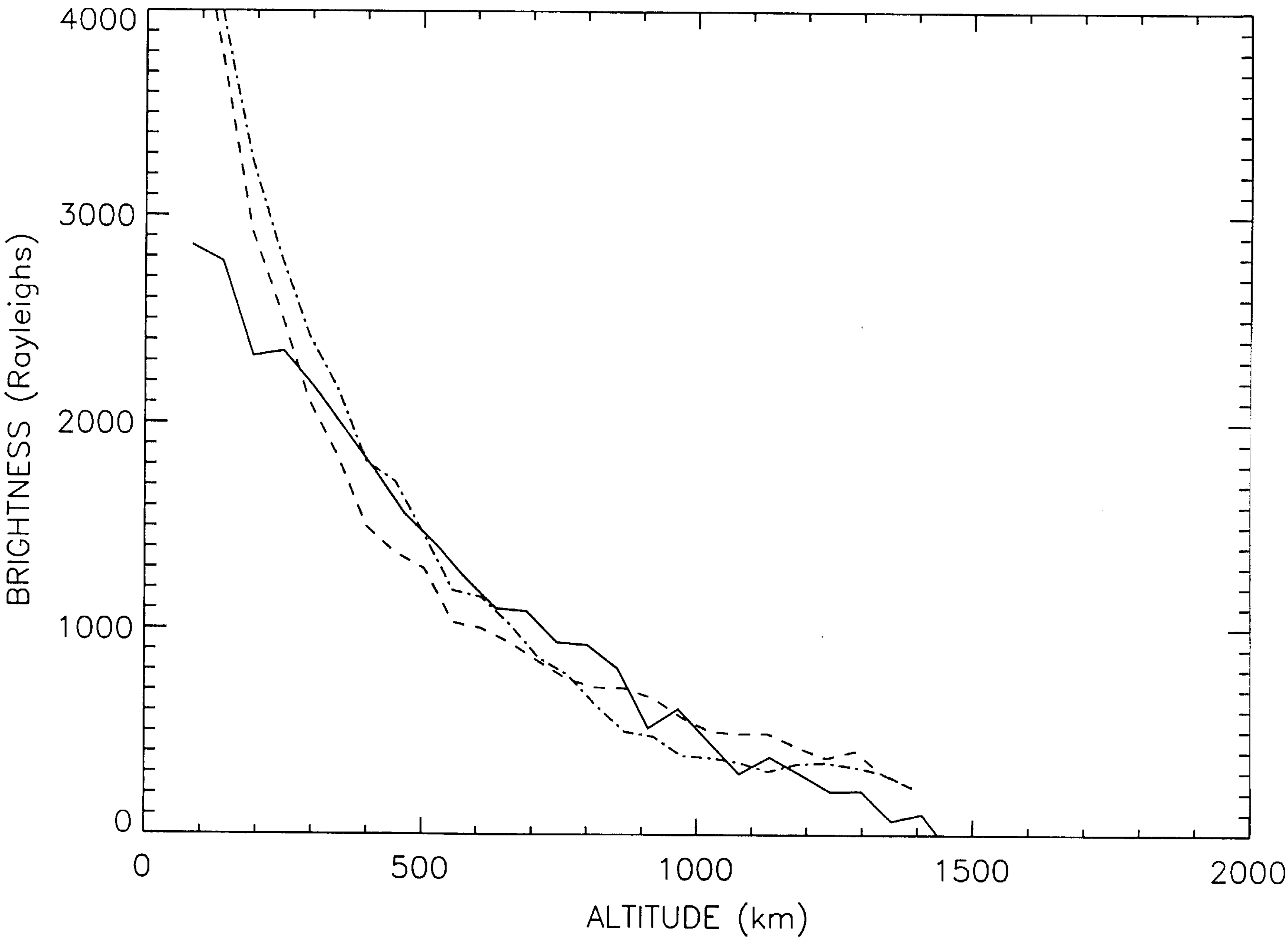
4000
3000
2000
1000
0
BRIGHTNESS (Rayleighs)
0
500
1000
1500
2000
ALTITUDE (km)

Figure 4a

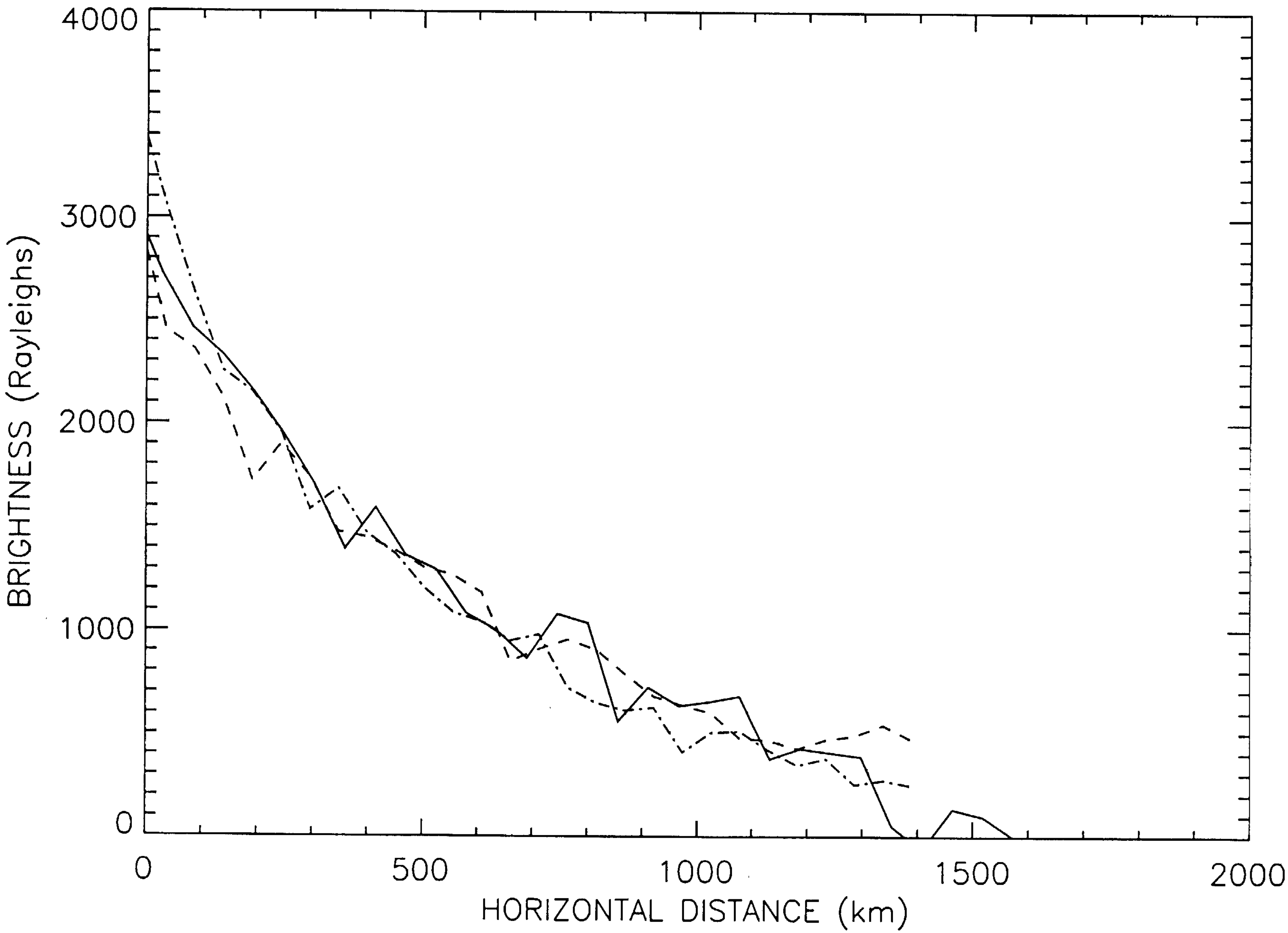
4000
3000
2000
1000
0
BRIGHTNESS (Rayleighs)
0
500
1000
1500
2000
HORIZONTAL DISTANCE (km)

Figure 4b

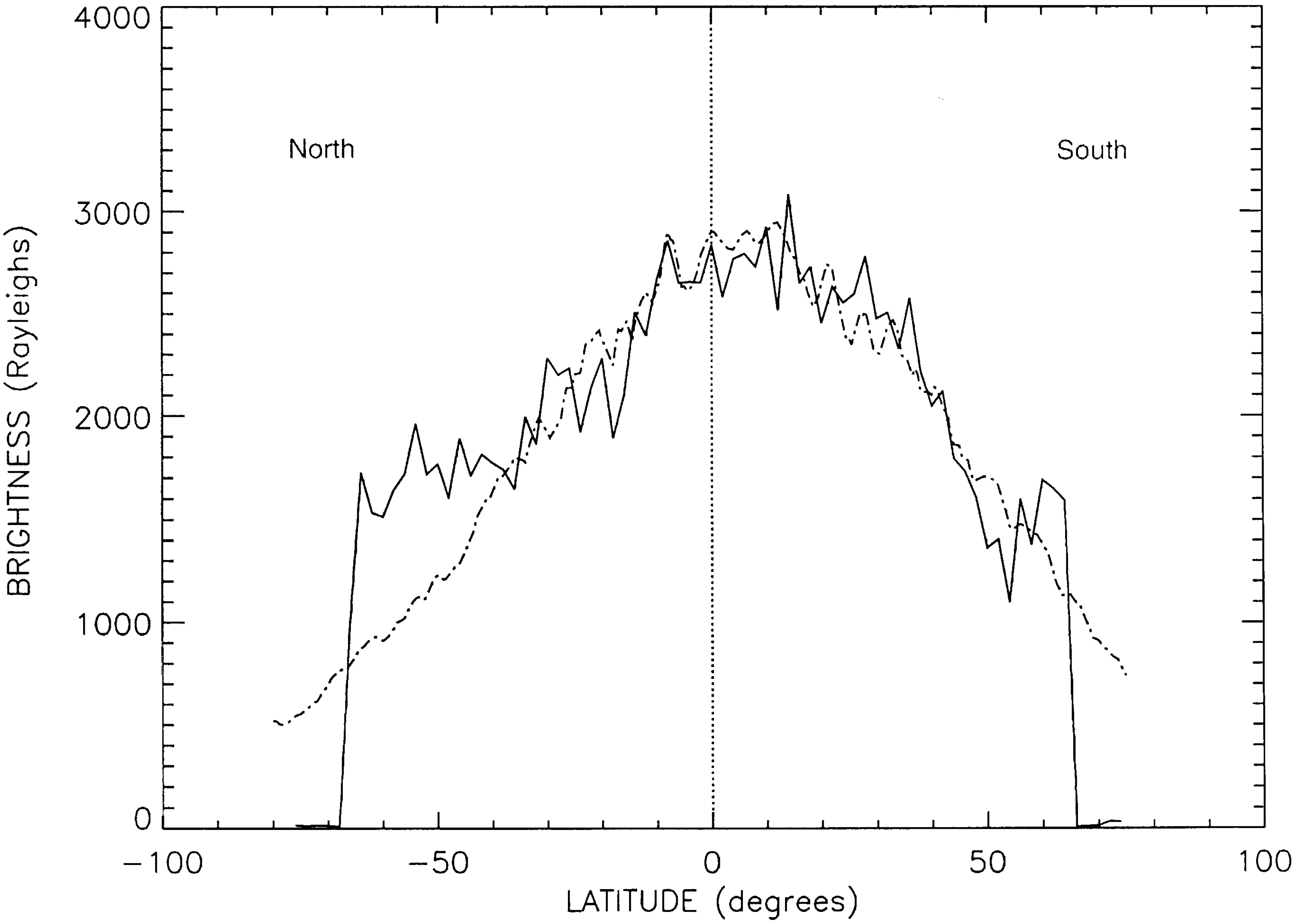

North
South
BRIGHTNESS (Rayleighs)
4000
3000
2000
1000
0
−100
−50
0
50
100
LATITUDE (degrees)

Figure 5

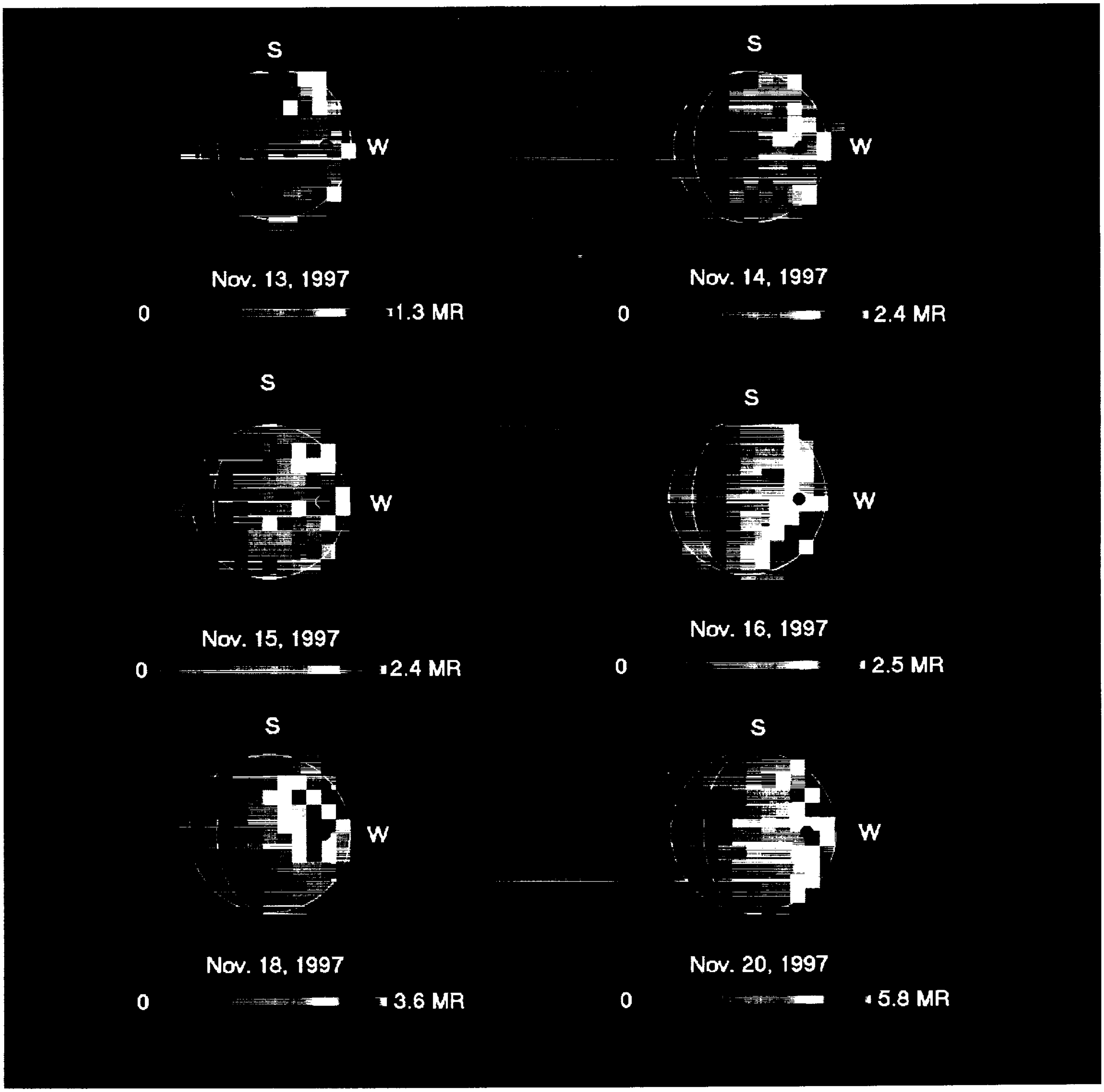
S
W
Nov. 13, 1997
0
1.3 MR
S
W
Nov. 14, 1997
0
2.4 MR
S
W
Nov. 15, 1997
0
2.4 MR
S
W
Nov. 16, 1997
0
2.5 MR
S
W
Nov. 18, 1997
0
3.6 MR
S
W
Nov. 20, 1997
0
5.8 MR

Figure 9

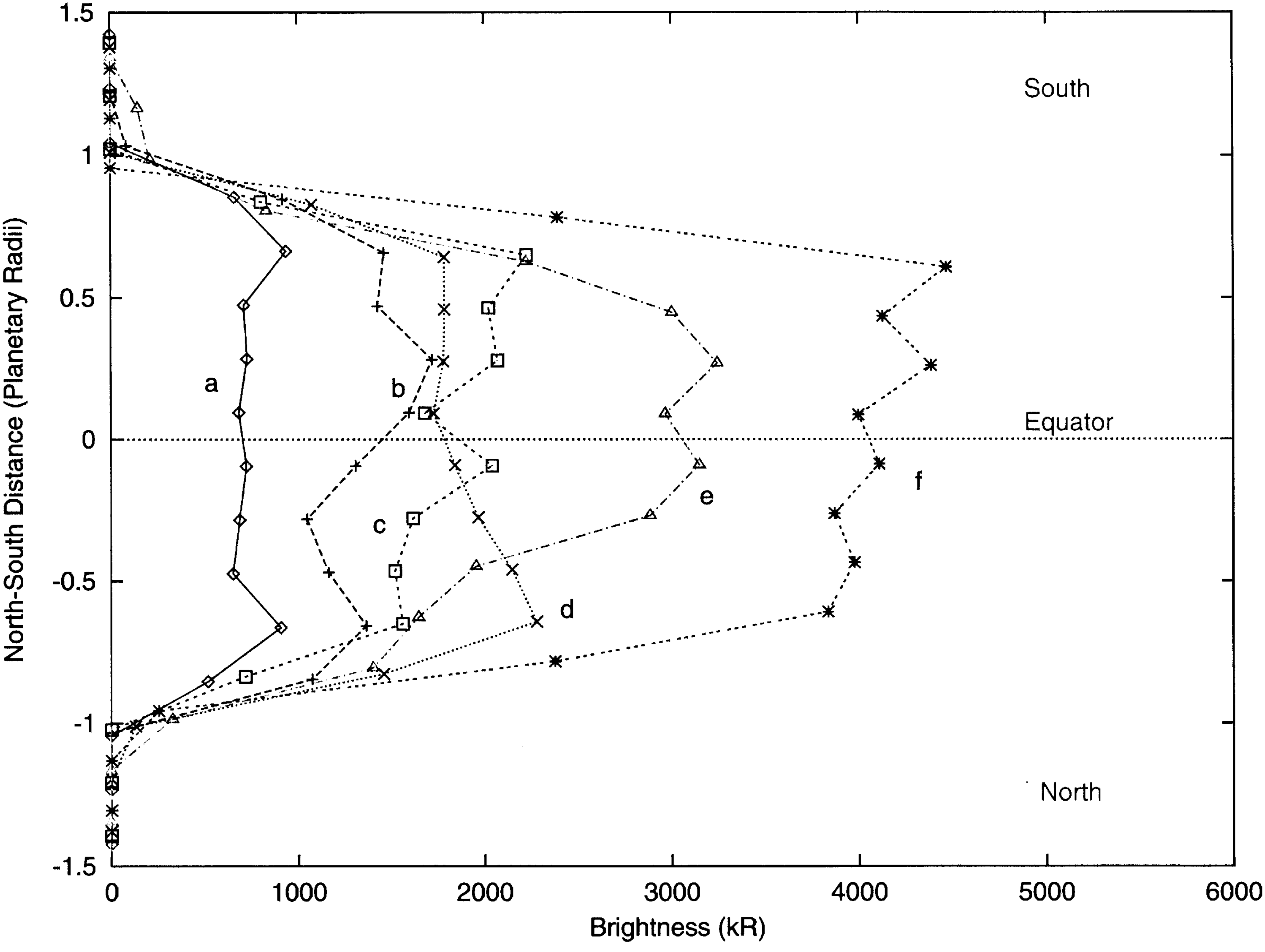
1.5
1
0.5
0
-0.5
-1
-1.5
North-South Distance (Planetary Radii)
0
1000
2000
3000
4000
5000
6000
Brightness (kR)
South
Equator
North
a
b
c
d
e
f

Figure 10a

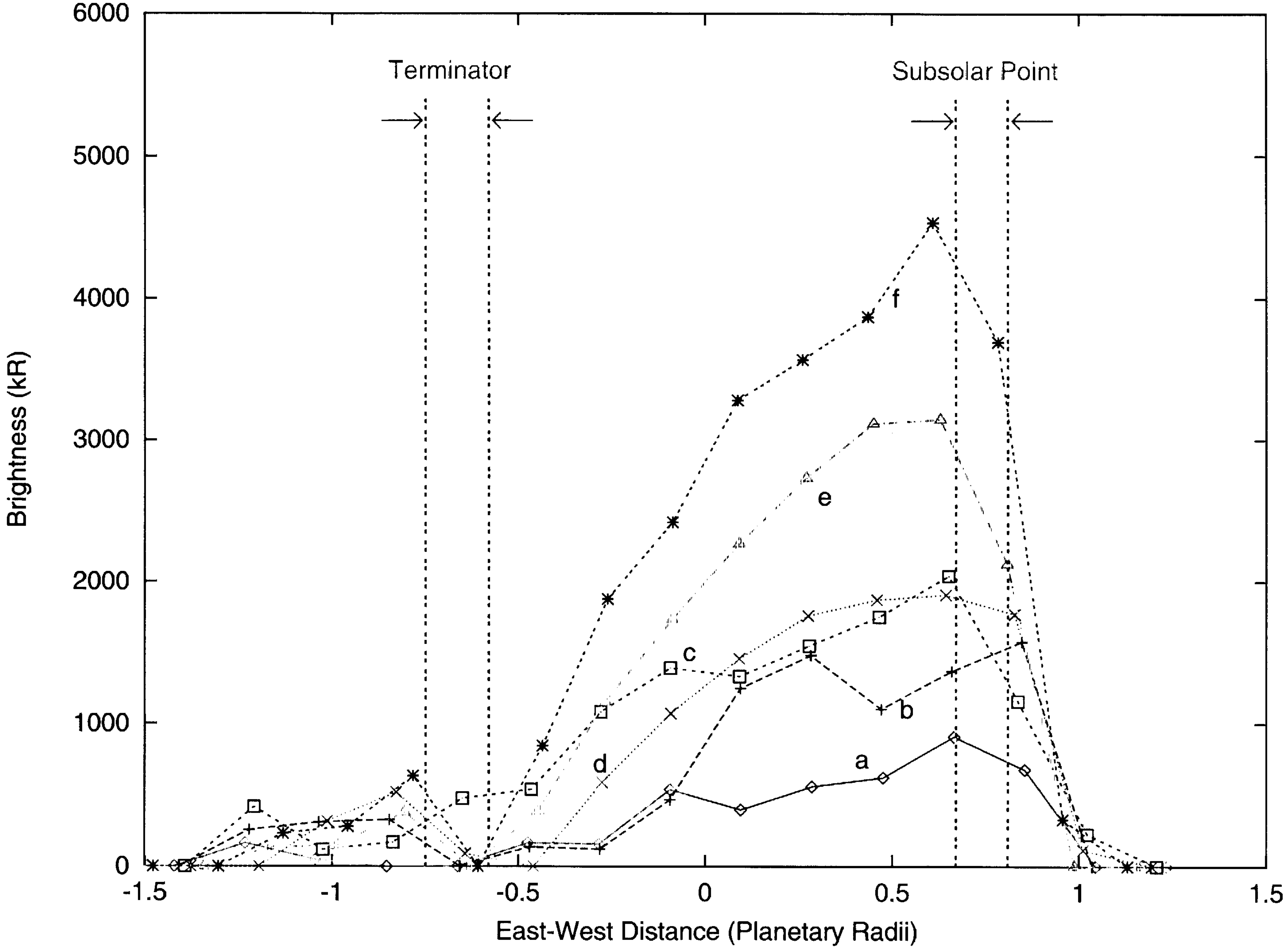

Brightness (kR)
6000
5000
4000
3000
2000
1000
0
-1.5
-1
-0.5
0
0.5
1
1.5
East-West Distance (Planetary Radii)
Terminator
Subsolar Point
a
b
c
d
e
f

Figure 10b

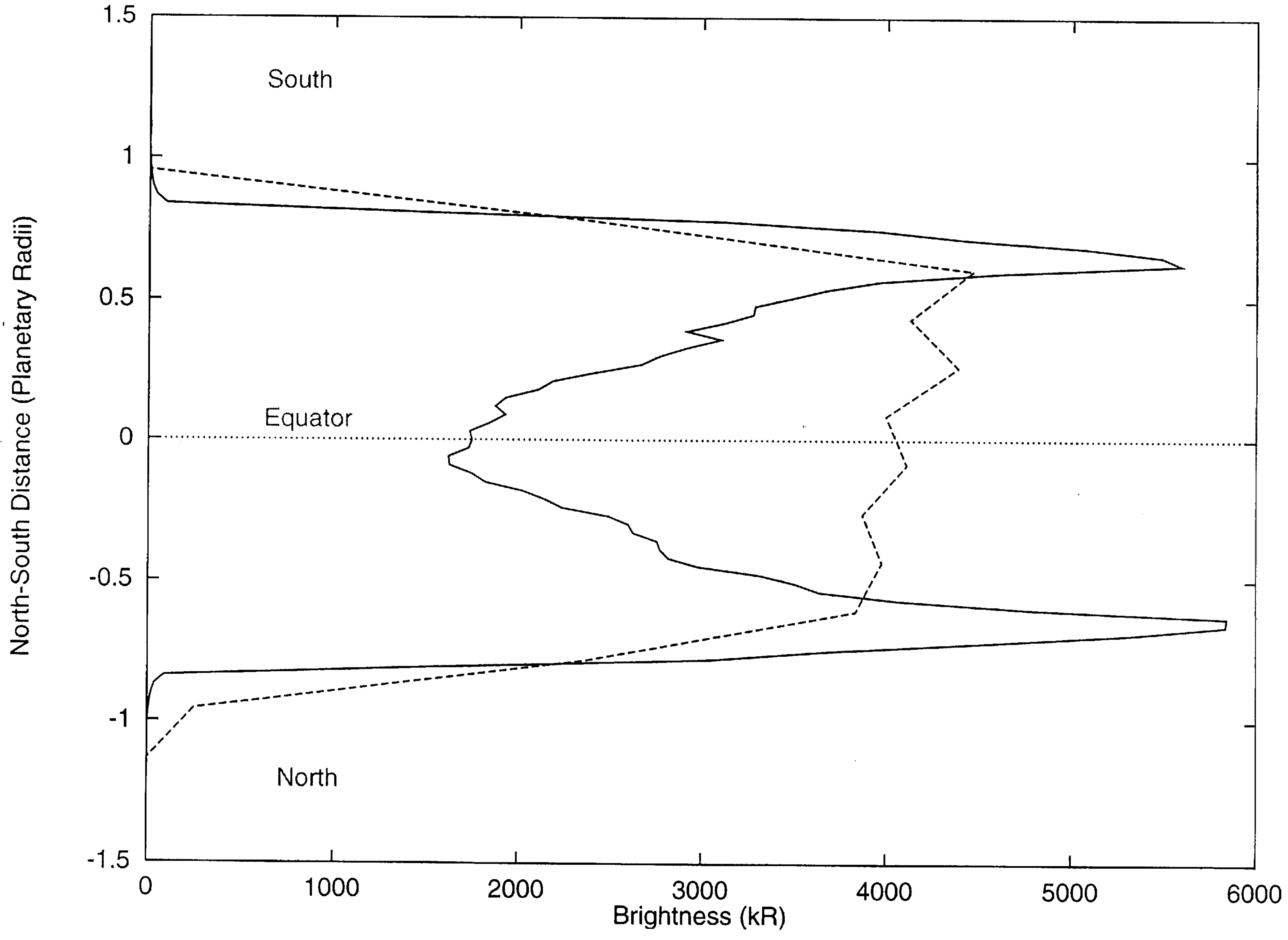
1.5
1
0.5
0
-0.5
-1
-1.5
North-South Distance (Planetary Radii)
South
Equator
North
0
1000
2000
3000
4000
5000
6000
Brightness (kR)

Figure 11a

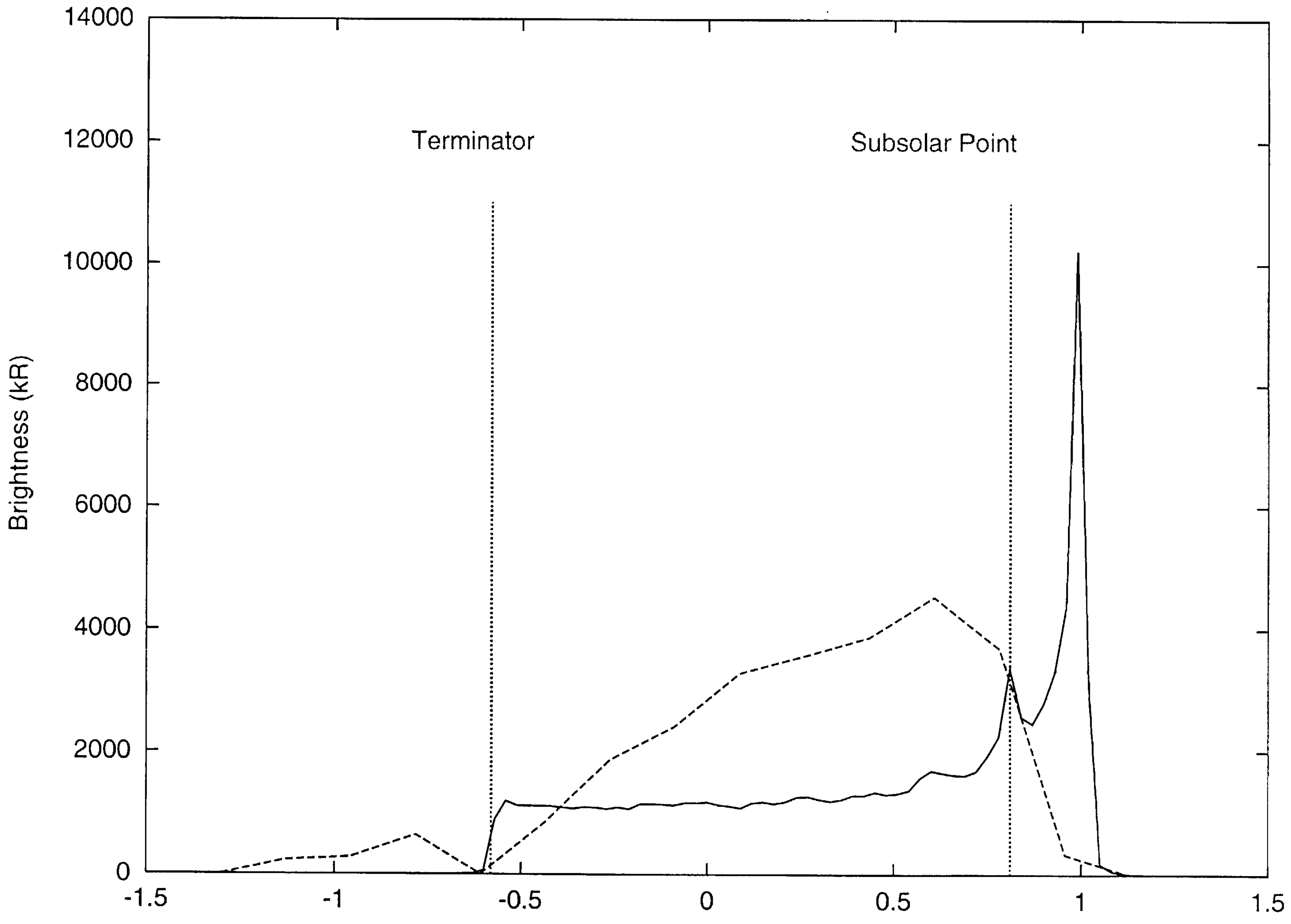

14000
12000
10000
8000
6000
4000
2000
0
Brightness (kR)
Terminator
Subsolar Point
-1.5
-1
-0.5
0
0.5
1
1.5
East-West Distance (Planetary Radii)

Figure 11b

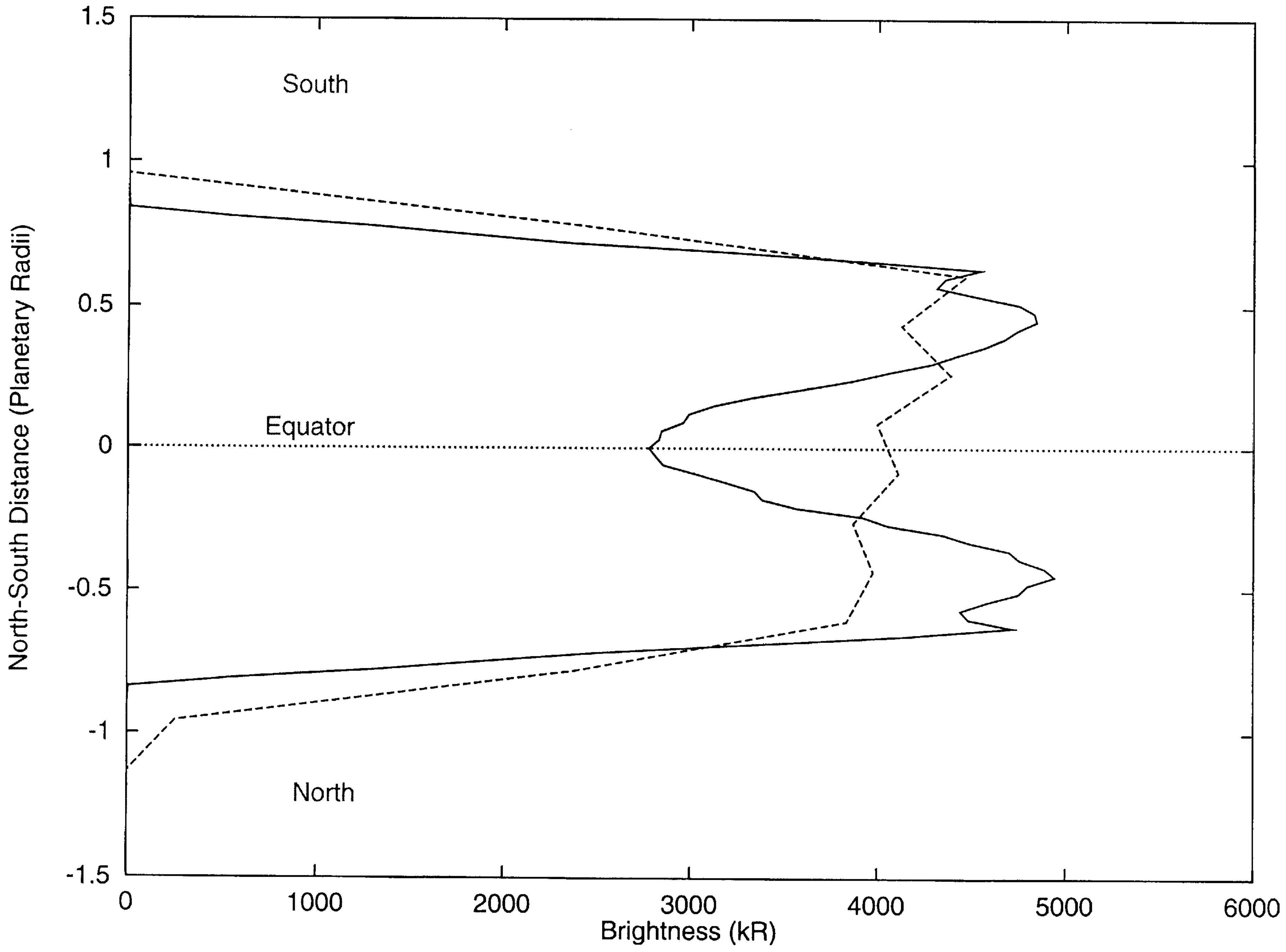
1.5
1
0.5
0
-0.5
-1
-1.5
North-South Distance (Planetary Radii)
South
Equator
North
0
1000
2000
3000
4000
5000
6000
Brightness (kR)

Figure 12a

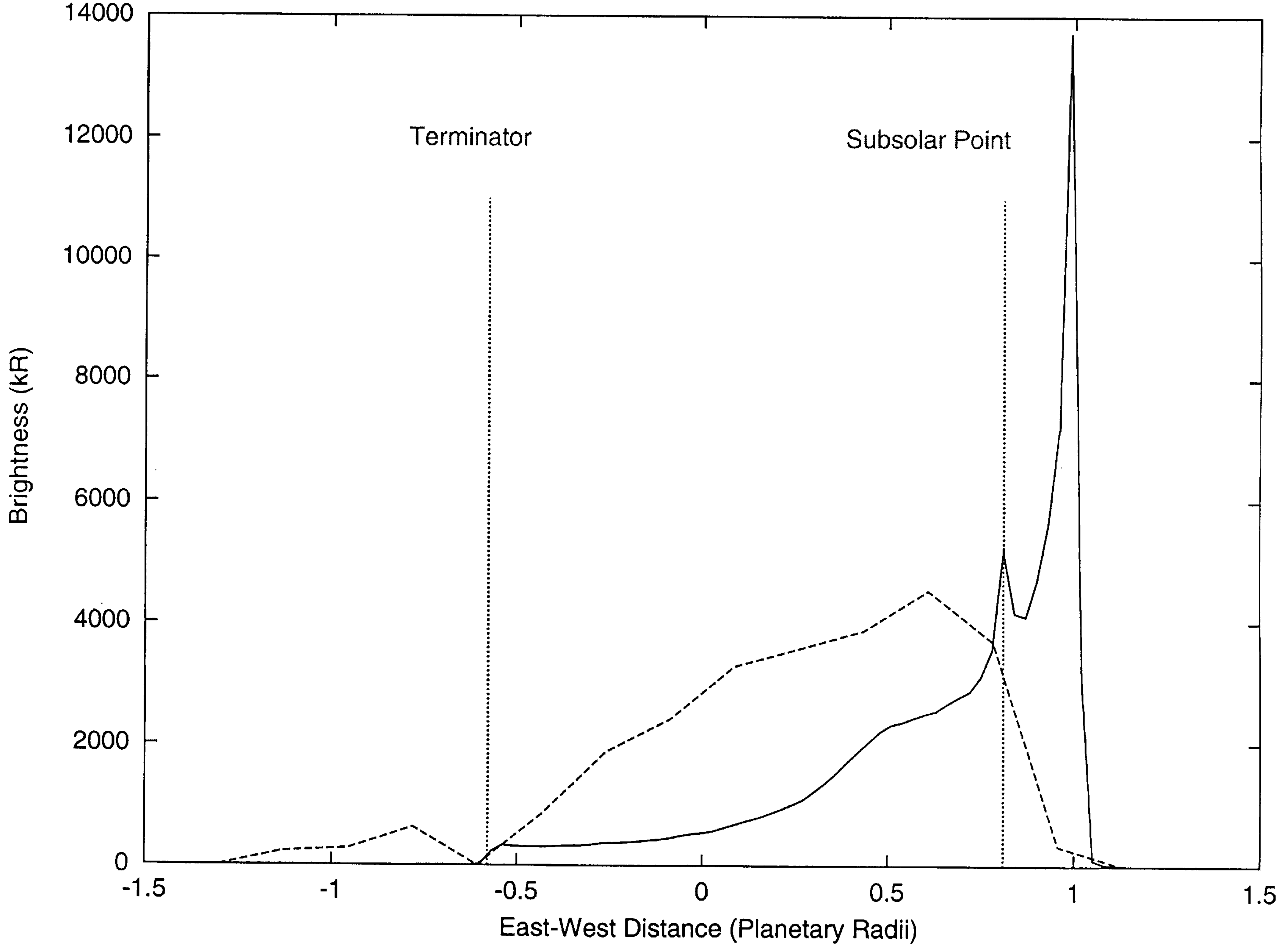
14000
12000
10000
8000
6000
4000
2000
0
Brightness (kR)
-1.5
-1
-0.5
0
0.5
1
1.5
East-West Distance (Planetary Radii)
Terminator
Subsolar Point

Figure 12b

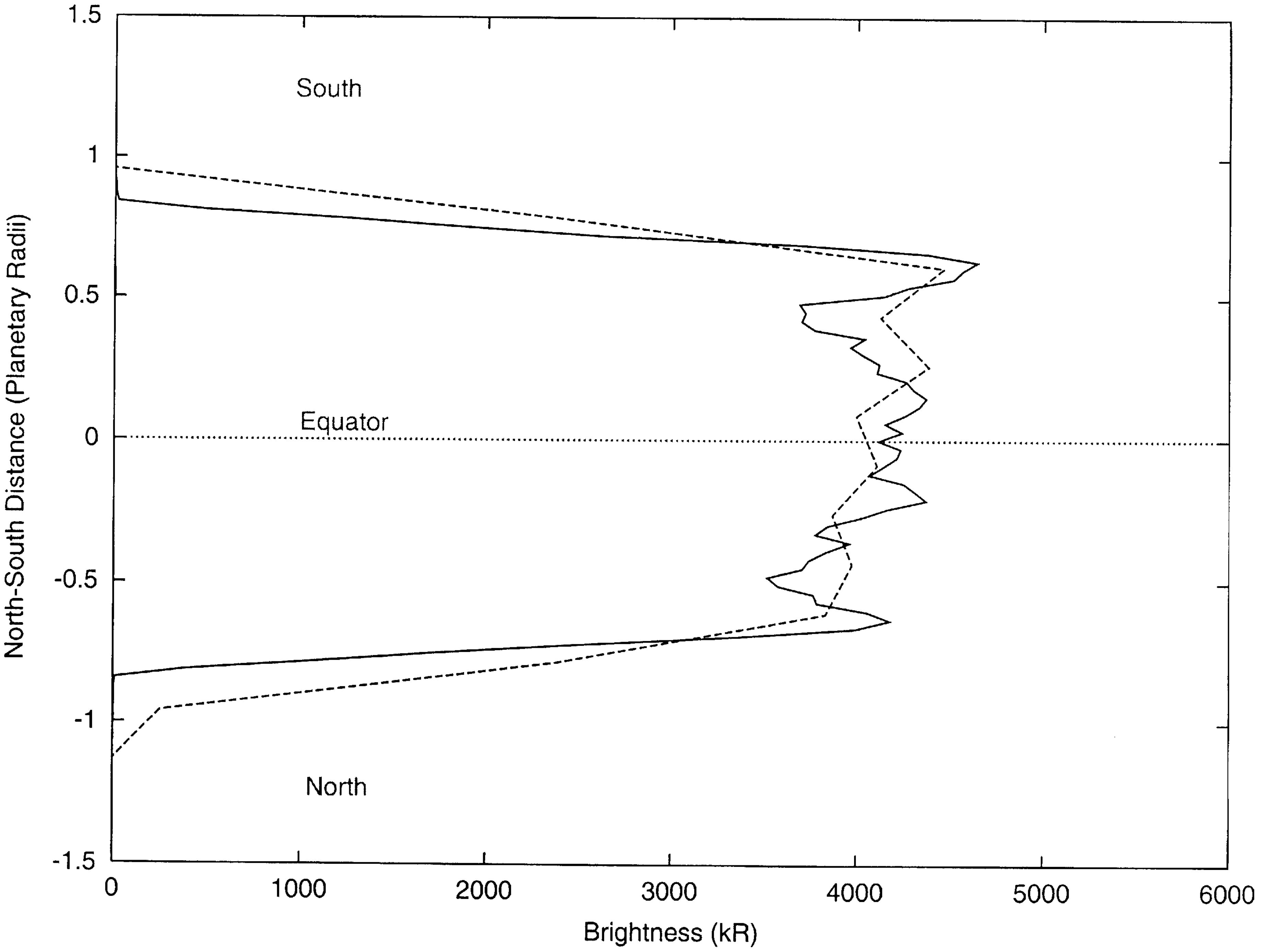
1.5
1
0.5
0
-0.5
-1
-1.5
North-South Distance (Planetary Radii)
South
Equator
North
0
1000
2000
3000
4000
5000
6000
Brightness (kR)

Figure 13a

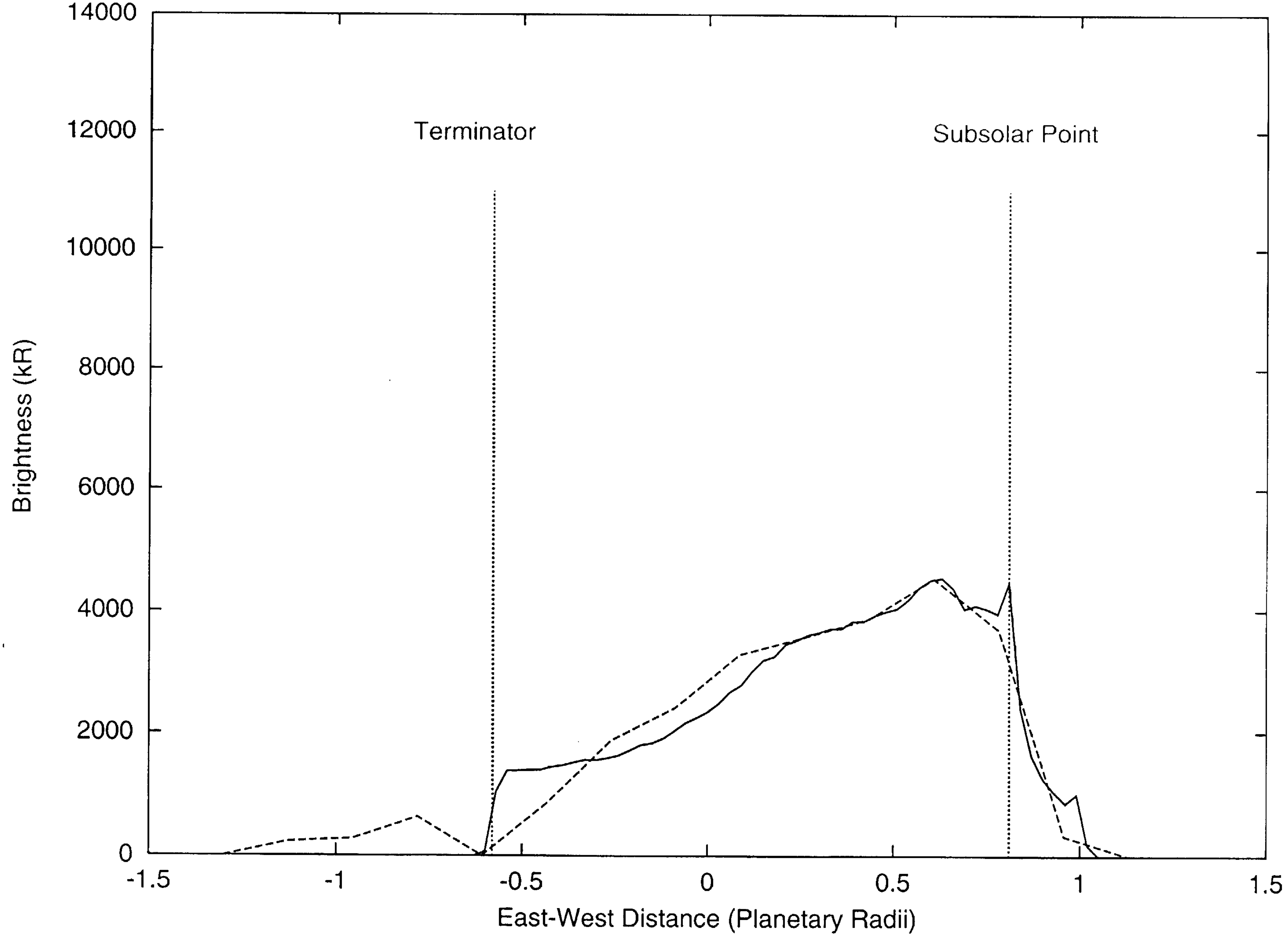
14000
12000
10000
8000
6000
4000
2000
0
Brightness (kR)
Terminator
Subsolar Point
-1.5
-1
-0.5
0
0.5
1
1.5
East-West Distance (Planetary Radii)

Figure 13b

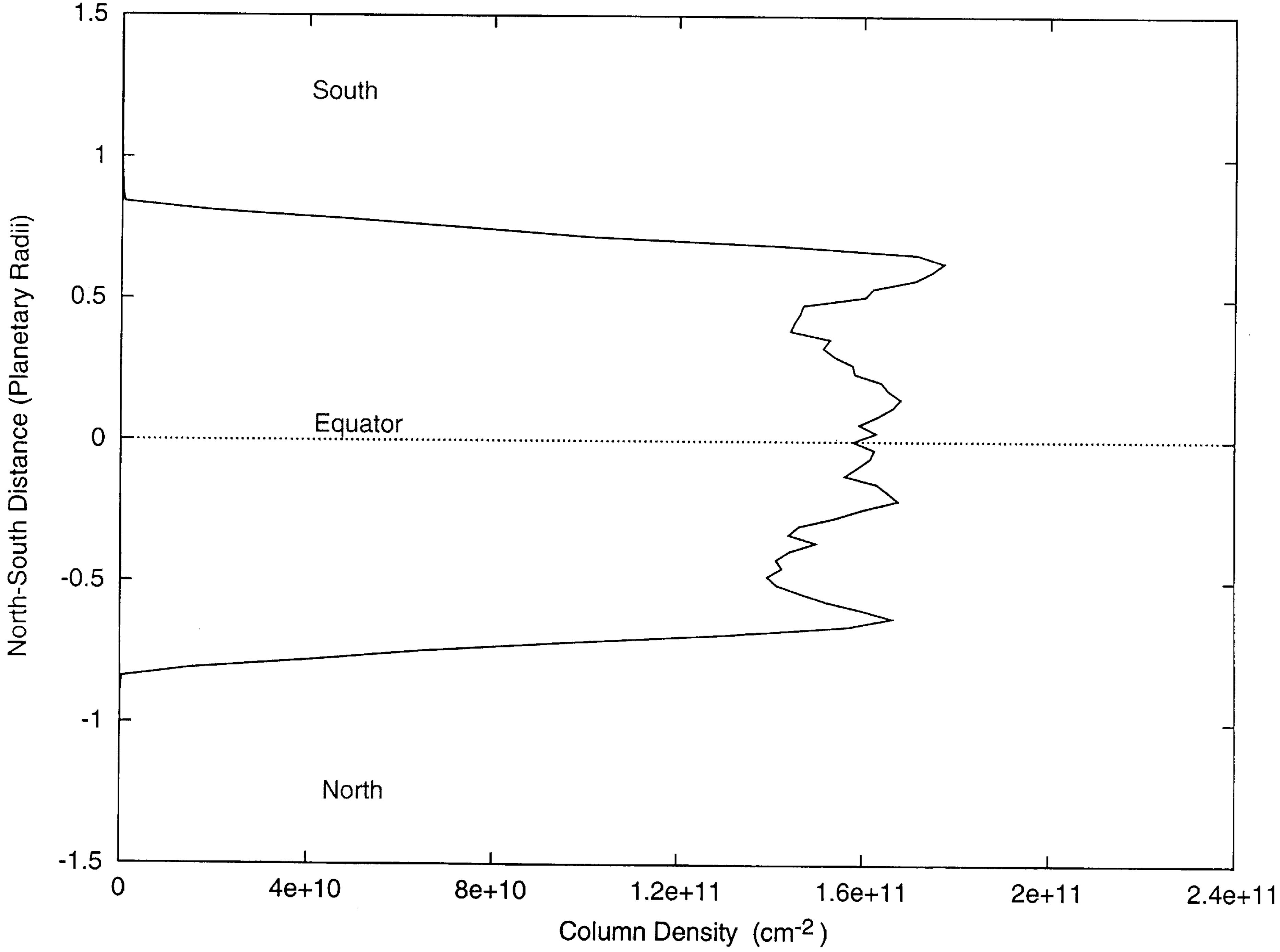

South
Equator
North
North-South Distance (Planetary Radii)
1.5
1
0.5
0
-0.5
-1
-1.5
0
4e+10
8e+10
1.2e+11
1.6e+11
2e+11
2.4e+11
Column Density (cm-2)

Figure 14a

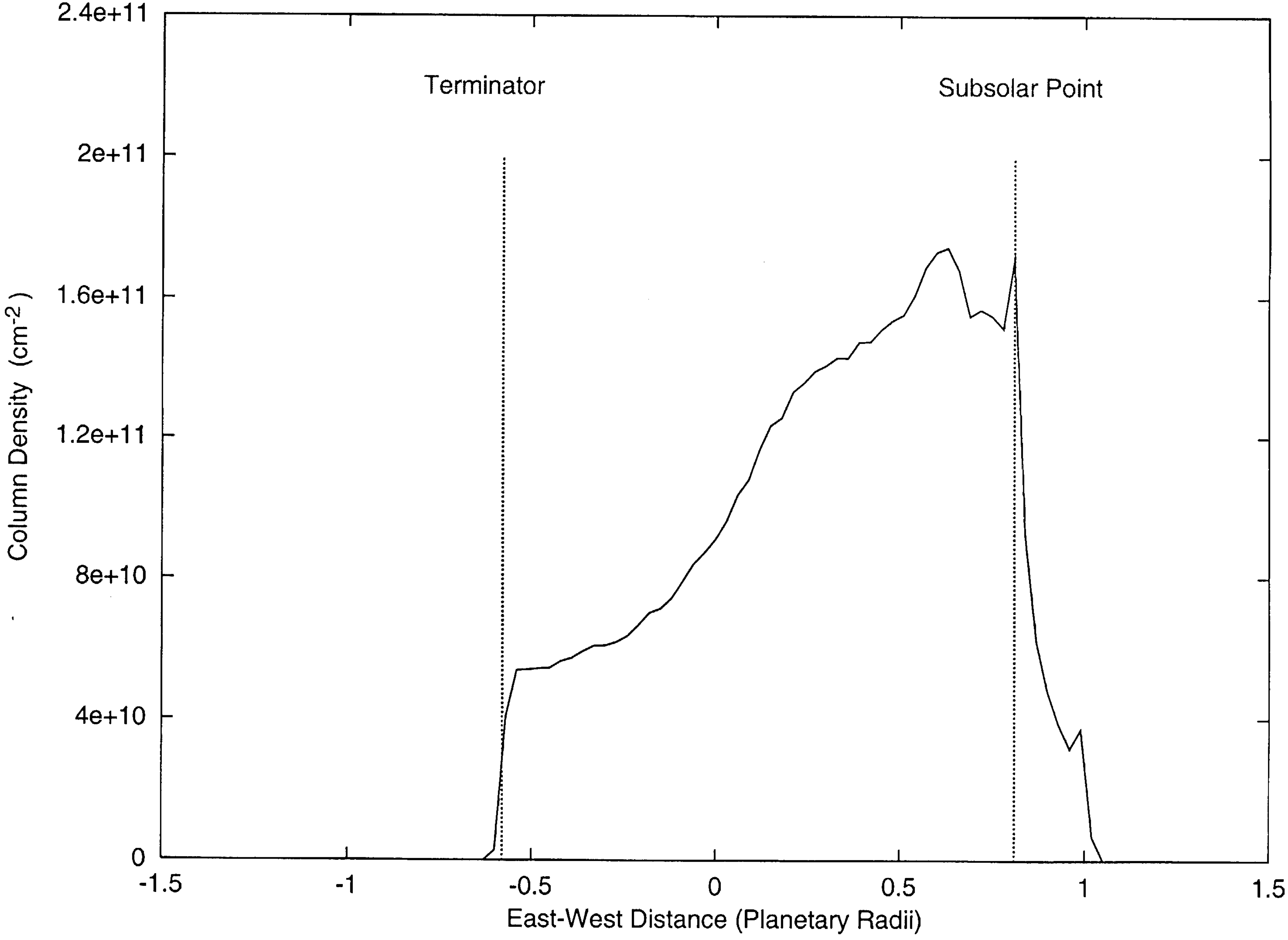
2.4e+11
2e+11
1.6e+11
1.2e+11
8e+10
4e+10
0
Column Density (cm^{-2})
-1.5
-1
-0.5
0
0.5
1
1.5
East-West Distance (Planetary Radii)
Terminator
Subsolar Point

Figure 14b

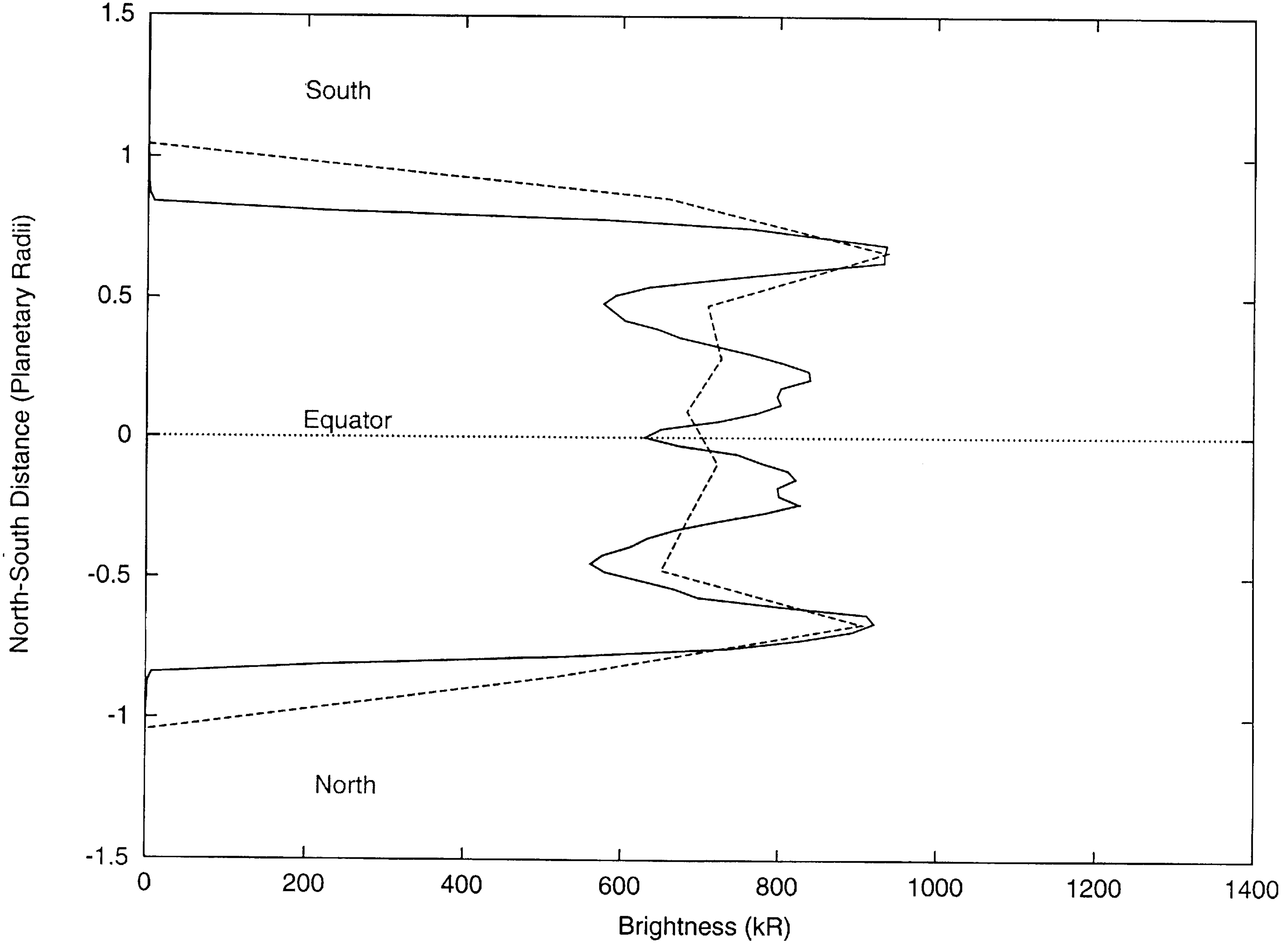
1.5
1
0.5
0
-0.5
-1
-1.5
North-South Distance (Planetary Radii)
South
Equator
North
0
200
400
600
800
1000
1200
1400
Brightness (kR)

Figure 15a

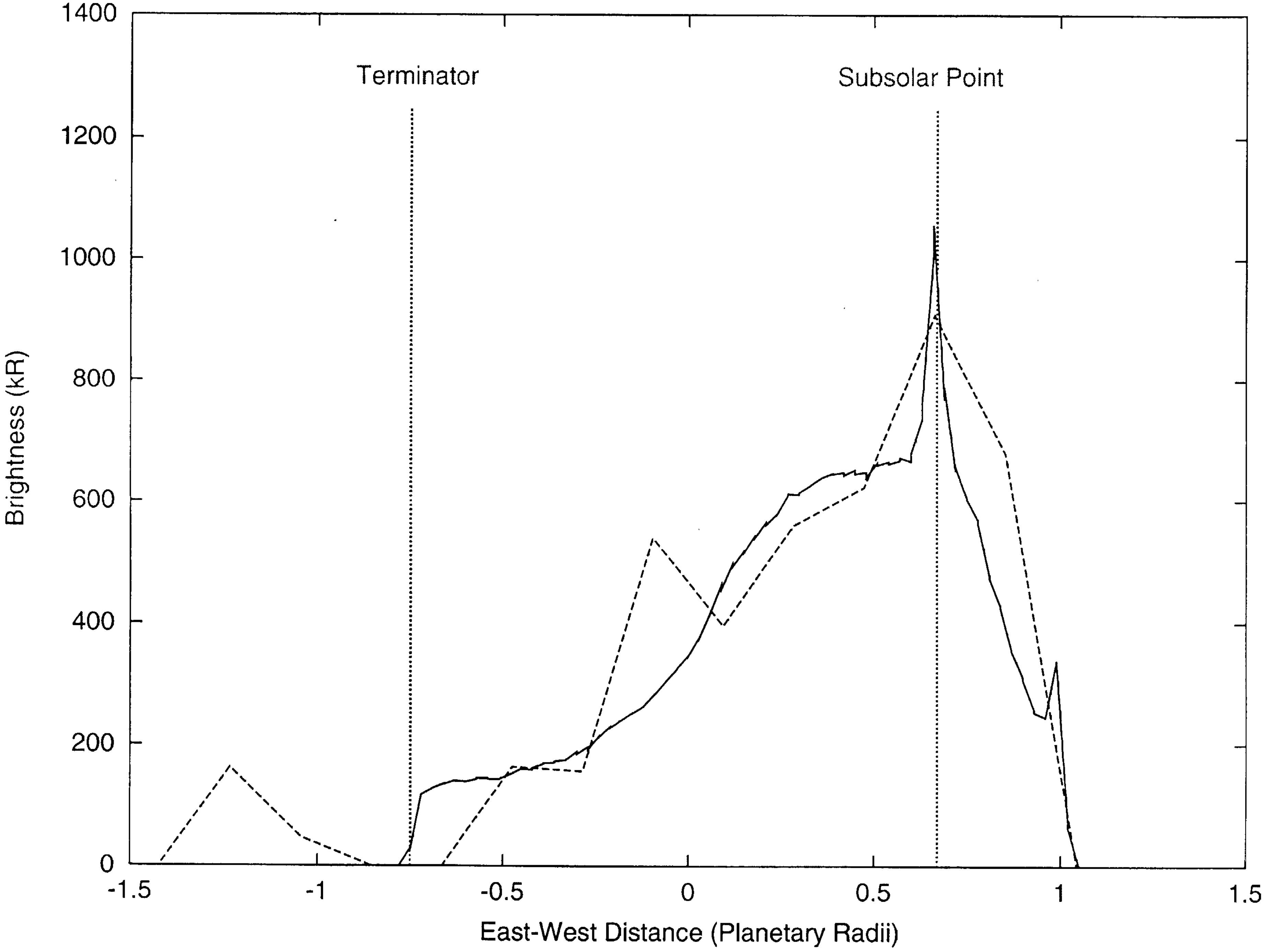
Terminator
Subsolar Point
Brightness (kR)
0
200
400
600
800
1000
1200
1400
-1.5
-1
-0.5
0
0.5
1
1.5
East-West Distance (Planetary Radii)

Figure 15b

APPENDIX A

Theoretical Overview and Modeling of the Sodium and Potassium Atmospheres of Mercury

THE ASTROPHYSICAL JOURNAL, 441:839–864, 1995 March 10

THEORETICAL OVERVIEW AND MODELING OF THE SODIUM AND POTASSIUM ATMOSPHERES OF MERCURY

WILLIAM H. SMYTH AND M. L. MARCONI
Atmospheric and Environmental Research, Inc., 840 Memorial Drive, Cambridge, MA 02139

Received 1994 February 9; accepted 1994 September 21

ABSTRACT

A general theoretical overview for the sources, sinks, gas-surface interactions, and transport dynamics of sodium and potassium in the exospheric atmosphere of Mercury is given. Information for these four factors, which control the spatial distribution of these two alkali-group gases about the planet, is incorporated in numerical models. The spatial nature and relative importance of the initial source atom atmosphere and the ambient (ballistic hopping) atom atmosphere are then examined and are shown to be controlled and coupled to a great extent by the extremely large and variable solar radiation acceleration experienced by sodium and potassium as they resonantly scatter solar photons. The lateral (antisunward) transport rate of thermally accommodated sodium and potassium ambient atoms is shown to be driven by the solar radiation acceleration and, over a significant portion of Mercury's orbit about the Sun, is sufficiently rapid to be competitive with the short photoionization lifetimes for these atoms when they are located on the sunlit surface near or within about 30° of the terminator. The lateral transport rate is characterized by a migration time determined by model calculations for an ensemble of atoms initially starting at a point source on the surface (i.e., a numerical spacetime dependent Green's function). Four animations for the spacetime evolution of the sodium (or potassium) atmosphere produced by a point source on the surface are presented on a videotape format (ApJ, 441, Part 1, No. 2, Videotape, Segment 3). For extended surface sources for sodium and potassium, the local column density is determined by competition between the photoionization lifetimes and the lateral transport times of atoms originating from different surface source locations. Sodium surface source fluxes (referenced to Mercury at perihelion) that are required on the sunlit hemisphere to reproduce the typically observed several megarayleighs of D_2 emission-line brightness and the inferred column densities of 1–2 × 10^{11} atoms cm^{-2} range from ~2–5 × 10^7 atoms cm^{-2} s^{-1}. The sodium model is applied to study observational data that document an anticorrelation in the average sodium column density and solar radiation acceleration. Lateral transport driven by the solar radiation acceleration is shown to produce this behavior for combinations of different sources and surface accommodation coefficients. The best model fits to the observational data require a significant degree of thermal accommodation of the ambient sodium atoms to the surface and a source rate that decreases as an inverse power of 1.5 to 2 in heliocentric distance.

Subject headings: acceleration of particles — planets and satellites: individual (Mercury) — videotapes

Accompanying videotape: ApJ, 441, Part 1, No. 2, Videotape, Segment 3

1. INTRODUCTION

Knowledge of the atmosphere of Mercury prior to 1985 was acquired from airglow and occulation measurements obtained by the ultraviolet experiment on the *Mariner 10* spacecraft (Broadfoot et al. 1974; Broadfoot, Shemansky, & Kumar 1976; Kumar 1976) during its three flybys of the planet (1974 March 29, 1974 September 21, and 1975 March 16). An upper limit for the gas density on the dayside surface of about 10^6 cm^{-3} was deduced and established that the atmosphere was exospheric down to the surface. Helium and atomic hydrogen were positively identified, and atomic oxygen was tentatively identified as atmospheric constituents with subsolar estimated densities of 4500 cm^{-3}, 8 cm^{-3}, and 7000 cm^{-3}, respectively (Broadfoot et al. 1976). Upper limits for the number density of Ar, CO_2, H_2O, O_2, N_2, and H_2 were also determined. The helium and hydrogen atmospheres were measured several thousands of kilometers above the surface and reflected at those altitudes surface velocity distributions that, although different, were approximately thermal in character. Airglow observations by *Mariner 10* made at higher spatial resolution, however, revealed irregular spatial structures and also the presence of a significantly cooler component of H atoms nearer (< 300 km altitude) the surface (Broadfoot et al. 1976; Shemansky & Broadfoot 1977), providing a total H surface number density of 90 cm^{-3} and perhaps reflecting a low speed signature for the atom-surface interaction.

In 1985, the dramatic Earth-based discovery (Potter & Morgan 1985) of intense (approximately several megarayleighs) sodium D-line (5890 Å, 5896 Å) emissions excited by solar resonance scattering in Mercury's atmosphere and the subsequent discovery (Potter & Morgan 1986) of similar but less bright (~80 kR) potassium-line (7665 Å, 7699 Å) emissions have provided a new and promising tool for remote study of the planet. Typical sodium and potassium sunlit column abundances are ~1–2 × 10^{11} atoms cm^{-2} and ~1 × 10^9 atoms cm^{-2}, respectively, and are comparable to (or less than) the estimated sunlit helium column abundance of ~3 × 10^{11} atoms cm^{-2} (Goldstein, Suess, & Walker 1981) so that the atmosphere is still exospheric. Since the discovery observations, a number of additional observations have been published for sodium (Potter & Morgan 1987; Killen, Potter, & Morgan 1990; Potter & Morgan 1990) and potassium (Sprague 1990). Very high spectral resolution line profile data for sodium (Potter & Morgan 1987) suggested that a significant fraction of the sodium atmosphere is approximately thermal in nature and hence possibly accommodated to the surface temperature since the spectral half-width of the measured line profile had a corresponding velocity width close to the surface temperature (i.e., ~500 K or a mean speed of ~0.6 km s^{-1}), but the possible presence of a small amount of high kinetic temperature sodium could not be ruled out. If the bulk of the atoms is then energetically characterized by the surface temperature, this would imply subsolar scale heights for sodium and potassium atoms of 56–69 km and 33–40 km, respectively, well within the nominal magnetopause subsolar-standoff altitude of 1460 km (Ness et al. 1974). Along the one-dimensional observing slit used in these earlier measurements, spatial variations in the sodium (Killen et al. 1990) and potassium (Potter & Morgan 1986) emission brightnesses and hence corresponding abundances were observed. For the brighter sodium emission, for which there are considerably more observations than for potassium, these spatial variations were seen to change on a timescale of less than 1 day (Killen et al. 1990) with an average column density that is anticorrelated (Potter & Morgan 1987) with solar radiation acceleration, which for sodium is large and modulated by more than a factor of 10 by Mercury's elliptical motion about the Sun (Smyth 1986a). This anticorrelation of the column abundance and solar radiation acceleration has been suggested to be caused by a modulation in the solar radiation acceleration–driven lateral transport of sodium atoms to the night side of the planet (Smyth 1986b, 1989; Ip 1986, 1990) and will be explored further in this paper.

More recently, excellent and particularly revealing two-dimensional images of the sodium brightness (Potter & Morgan 1990; Morgan & Potter 1992) and the potassium brightness (Morgan & Potter 1992) have been obtained. These monochromatic images show planet-wide changes in the brightness distributions with one or two localized regions increasing or decreasing on a timescale of at least 1 day (the time between successive images). These images have brought into focus, unambiguously, what had been only partially understood from the earlier one-dimensional and slit-averaged data. Potter & Morgan (1990) concluded that these spacetime variable images provided evidence for magnetospheric-driven (perhaps substorm related) ion sputtering of sodium and potassium atoms from the surface. Alternatively, these bright spots have more recently been suggested as morning temperature-dependent degassing of nonuniform night-enhanced regolith (Sprague 1992). A recent review (Potter 1993) of all of the observational data for sodium and potassium, however, shows that the time-varying bright spots are also distributed near the evening portion and not exclusively located near the morning portion of the planet. Earlier one-dimensional slit observations for potassium (Sprague, Kozlowski, & Hunten 1990) related measured enhancements to an increased diffusion of alkali atoms from well fractured crust and regolith associated with the Caloris impact basin, but the idea of an interior diffusion source (Tyler, Kozlowski, & Hunten 1988; Sprague 1990) has been seriously challenged (Killen 1989; Killen, Potter, & Morgan 1991; Shemansky & Morgan 1991; Killen & Morgan 1993). The spacetime evolution of a localized surface source and its dependence on a variety of parameters in creating a bright spot in the atmosphere will be explored in comparative animation sequences generated by model simulations.

In this paper, a theoretical overview is first presented in § 2 to depict the character and to evaluate the relative importance of various physical processes in shaping the sodium and potassium atmospheres of Mercury. This detailed knowledge is then incorporated in models for the sodium and potassium atmospheres in § 3. In § 4 the models are applied to exploratory studies, modeling analysis studies of the sodium atmosphere, and to animation sequences presented on a videotape format (ApJ, 441, Part 1, No. 2, Videotape, Segment 3). Finally, a summary with concluding comments is given in § 5.

2. THEORETICAL OVERVIEW

2.1. *Introduction*

Since the atmosphere of Mercury is essentially exospheric in nature, gas-phase collisions are negligible. This simple fact has a profound consequence, namely, that Mercury has multi-atmospheres, with each separate atmosphere forming independently and hence each having the capacity of being very different. These differences are determined by the unique properties of each particular gas, the nature of the sources and sinks for that gas, and the interactions of that gas with the surrounding environment. Thus, atoms that are liberated from the surface by some source mechanism and are initially gravitationally bound will later impact the surface and move independently from point to point on the surface by ballistic hops. The general situation is illustrated in Figure 1. In addition to the source characteristics, the number and shape of these ballistic hops are determined by (1) the relevant forces acting on each atom, (2) the nature of the gas-surface interactions, and (3) the various loss processes that are operative. The relevant forces are the gravitational field of the planet and the solar radiation pressure acceleration experienced by the atoms. For sodium and potassium, solar radiation acceleration is very large and depends upon the radial velocity of the atom with respect to the Sun because of the Fraunhofer absorption features in the solar spectrum. The gas-surface interactions are determined by various physical and chemical processes that are not well understood but that at least depend on the local surface temperature and composition (Shemansky & Broadfoot 1977; Hunten, Morgan, & Shemansky 1988; Shemansky 1993). The processes determine the probability that an atom upon encountering the surface will stick to it for a long time or, alternatively, will rebound nearly instantaneously from it with a kinetic energy that is accommodated to some degree with the local surface temperature. The loss processes for atoms in the sunlit hemisphere (which are the only atoms remotely observed at Earth through their emission lines excited by solar resonance scattering) include dayside surface capture, gravitational escape, photoionization followed by magnetospheric convection, and lateral transport to the nightside. Some fraction of the ions that undergo magnetospheric convection will not be lost from the body but will be recycled by collision with the surface and be captured and, if sufficiently energetic, liberate other atoms from the surface by ion sputtering.

Atoms that are liberated from the surface by various source mechanisms are called "source atoms" and may be thermal or nonthermal in nature. Source atoms that encounter the surface and have one or more additional ballistic hops are called "ambient atoms" and form the bound component of the atmosphere. These two components of the atmosphere were introduced by Hunten et al. (1988) to clarify the role of the initial source and the gas-surface interactions in forming an exospheric atmosphere and have since been generally adopted in

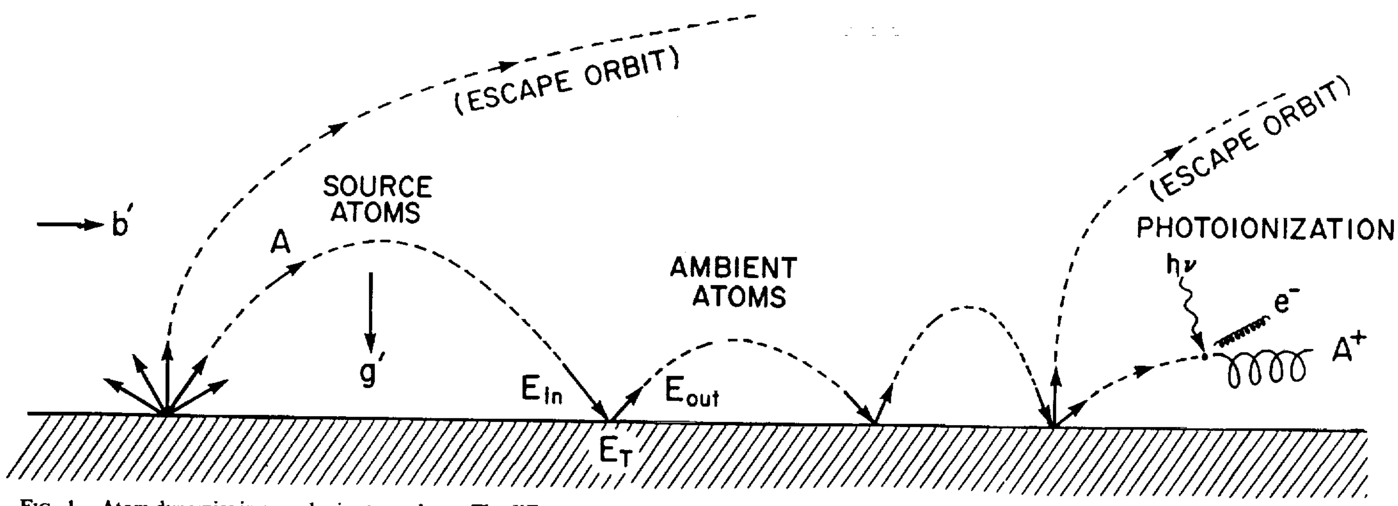

FIG. 1.—Atom dynamics in exospheric atmospheres. The different trajectories of source atoms liberated from the surface (at the left) are shown under the influence of the effective local gravity (g′), the component of solar radiation acceleration (b′) parallel to the surface, gas-surface encounters, and photoionization.

the literature. Source atoms that initially have sufficient energy to escape gravitationally from the body (or ambient atoms that eventually gain sufficient energy to escape) will form an atmospheric coma. Because of the action of solar radiation acceleration, the sodium and potassium comae will have a sunward neutral pause and an antisunward tail structure similar to that of a comet coma as illustrated for sodium by Smyth (1986a) and Ip (1986). The local vertical density structure of the atmosphere is basically determined by the relative populations of the ambient atoms and the source atoms and the degree of thermal accommodation achieved by the ambient atoms as they migrate on the surface. The density distribution about the body is basically determined by the longitudinal, latitudinal, and time-dependent nature of the source mechanisms and the competition between the local lateral transport time and the loss lifetime of the atoms. The general situation is shown in Figure 2. Atoms reside in three different reservoirs: an external reservoir, an atmospheric reservoir, and a surface reservoir. As illustrated in Figure 2, the nature of the atmosphere is determined by the relative importance of processes that control the interchange between the atmospheric reservoir and the external and surface reservoirs. Source atoms for the atmospheric reservoir are supplied by various external and surface source mechanisms and will generally have both escape and ballistic components. If the source has only an escape component, the atmospheric structure is rapidly determined, and the process in Figure 2 terminates at point 1. If a ballistic component exists, the ballistic atoms may be captured by the surface (i.e., stick to the surface) upon impact. If all ballistic atoms stick to the surface, the atmospheric structure is established totally by the source atoms, and the process is terminated at point 2. If, however, the ballistic component is not captured (or only partially sticks to the surface), an ambient atmosphere is produced. Subsequent interactions of ambient atoms with the surface or with solar radiation may cause some of these atoms to escape (point 3). Energetic ambient atoms from the dayside atmosphere on long ballistic orbits may populate the nightside atmosphere directly. Less energetic ambient atoms in the dayside (nightside) atmosphere will populate the nightside (dayside) atmosphere by lateral transport that may be greatly enhanced (retarded) by solar radiation acceleration. The remaining ambient atoms migrate on the surface and produce the two-dimensional structure of the atmosphere. Some fraction of atoms in the nightside atmosphere may also be captured by the surface and returned to the dayside atmosphere by the rotation of the planet (point 5). Atoms in the dayside or nightside atmosphere may undergo ionization (point 4) and be either lost from the planet by magnetospheric convective loss or be recycled to the planet by surface capture (point 6). The spacetime-dependent nature of the source mechanisms and the nature of the gas-surface interactions for Mercury remain the central quantities that must be deduced unambiguously from observational data for sodium and potassium.

The four primary factors—sources, sinks, gas-surface interactions, and transport dynamics—that control the spatial distribution of sodium and potassium in the atmosphere of Mercury will now be briefly discussed. Although these factors are conceptually distinct, they are coupled in observational brightness data for the atmospheres and are not easily separated uniquely. It is therefore particularly important to understand these factors individually and to include their spacetime dependencies properly in models in order to interpret correctly various atmospheric observations.

2.2. *Sources*

Possible sources for sodium and potassium in Mercury's atmospheres have been discussed in a number of papers in the last 10 years and include those by Potter & Morgan (1985); Smyth (1986a); McGrath, Johnson, & Lanzerotti (1986); Ip (1987); Cheng et al. (1987); Morgan, Zook, & Potter (1988, 1989); Tyler et al. (1988); Hunten et al. (1988); Killen (1989); Killen et al. (1990); Sprague (1990); Sprague et al. (1990); Potter & Morgan (1990); Shemansky & Morgan (1991); Sprague (1992); and Killen & Morgan (1993). The most recent and comprehensive review for the source mechanisms for Mercury's sodium atmosphere by Killen & Morgan (1993) presents four major conclusions. First, the most likely mechanism for supply of sodium to the surface is the creation of fresh regolith from infall material (not upward diffusion or venting from within the planet). Second, for a likely sodium regolith abundance of 0.4% by mass (i.e., similar to lunar highlands composition), the estimated rate of creation of fresh regolith is a factor of 3 too small to balance the steady state sodium rate assuming 50% recycling of photoions. If, however, the relative

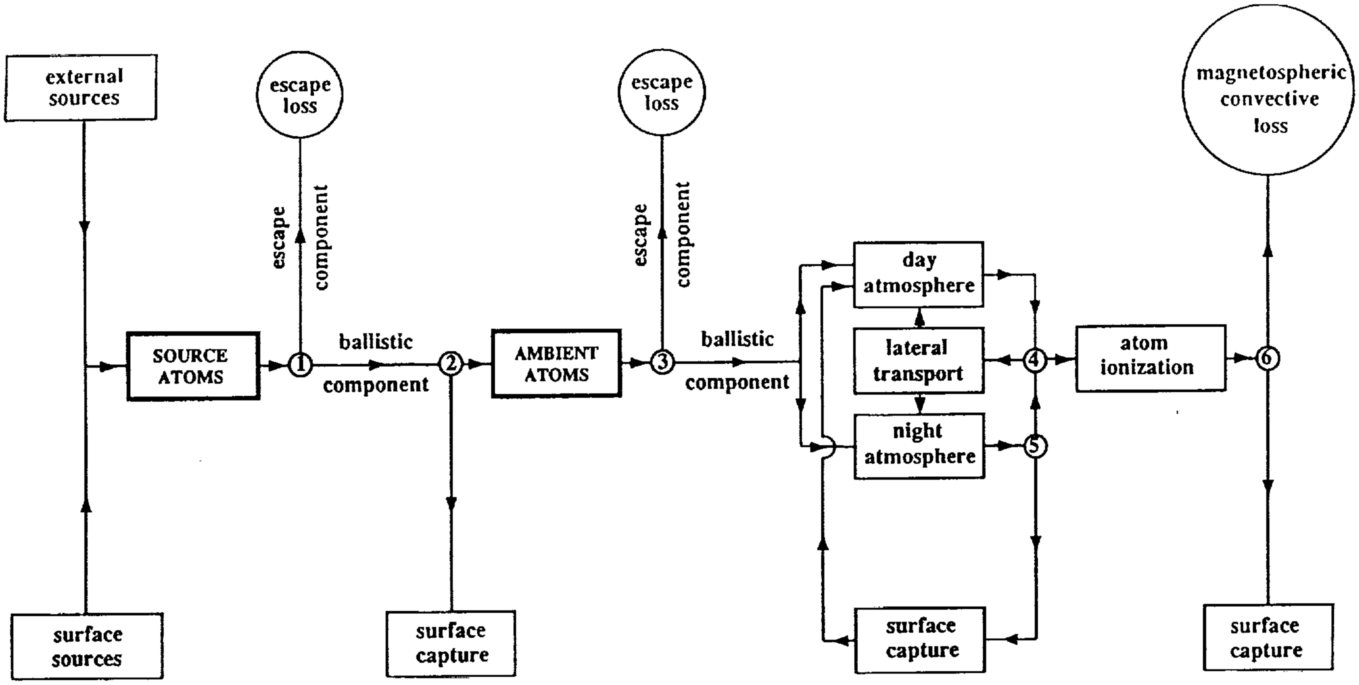

FIG. 2.—Interchange of gas between external, atmospheric, and surface reservoirs. The development of an exospheric atmosphere depicted pictorially in Fig. 1 is shown in a more interactive physical manner. See text for discussion.

abundance of sodium in the crust is more terrestrial in nature (i.e., ~1%–2%), then the regolith overturn is sufficient to balance the steady state sodium-loss rate. Third, the supply of sodium atoms to the atmosphere by impact vaporization driven by infalling micrometeoroides is typically only a few percent of the required steady state rate ($\sim 10^{25}$ atoms s^{-1}). Fourth, given our lack of knowledge about photodesorption yields from the surface, ion fluxes in the atmosphere, and the state of the magnetosphere, it is not possible at present to estimate accurately the surface source rates to the atmosphere for either ion sputtering or photodesorption, although their maximum estimated rates are sufficient to maintain the required steady state rate.

2.3. *Sinks*

The lifetime of sodium and potassium atoms in the sunlit atmosphere is short and dominated by photoionization. Because of the large eccentricity (0.2056) of the planetary orbit about the Sun, the Sun-Mercury distance changes by a factor of 1.52, and the photoionization lifetimes change by a factor of 2.30 and range from 1.4–3.3 hr for sodium and 0.97–2.2 hr for potassium. The next most important lifetime limiting process for sodium and potassium is electron impact ionization in the solar wind that varies from 23–64 hr for sodium and from 15–45 hr for potassium. The ambient atmosphere, however, is almost always largely shielded (~94% of the time; Goldstein et al. 1981) from the direct interactions with the variable conditions of the solar wind by the planetary magnetic field which forms a magnetopause at a nominal subsolar altitude of 1460 km (0.6 Mercury radii).

2.4. *Gas-Surface Interactions*

The gas-surface interactions are determined by various physical and chemical processes that can be rather complex and are not well understood. The subject has been discussed for Mercury by Shemansky & Broadfoot (1977) and more recently for sodium and potassium by Hunten et al. (1988) as well as Shemansky (1993). Physical adsorption is generally described by an energy accommodation coefficient β and by an atom residence time for adsorption that are dependent on surface composition and highly dependent on the surface temperature. The effective energy accommodation coefficient β used in this paper is defined by

$$\beta = \frac{(E_{\text{out}} - E_{\text{in}})}{(E_T - E_{\text{in}})} , \qquad (1)$$

where the energy of the atom (see Fig. 1) is E_{in} before impact and E_{out} after impact, and where the thermal energy of the surface is donated by E_T. In the atmospheric model described in § 3, this coefficient includes any process (e.g., single and multicollisional physical adsorption encounters with the surface) that partially thermalizes the atom and then allows it to exit the surface in a residence time for physical adsorption that is typically much shorter than a local ballistic timescale. The energy accommodation coefficient is defined so that $\beta = 0$ for 0% surface accommodation (elastic bounce) and $\beta = 1$ for 100% surface accommodation.

For the ideal case of a 600 K α quartz flat surface, the value of the energy accommodation coefficient for a single collisional encounter event with the surface has been estimated to be 0.62 for sodium and 0.26 for potassium (see Table IV in Hunten et al. 1988). These values imply that sodium and potassium will likely have a significant nonzero value of the energy accommodation coefficient that may be of the order of several tenths or more so that these atoms will likely accommodate to the surface of Mercury in a few bounces, which is generally consistent with the velocity information in the sodium line profile observed by Potter & Morgan (1987). As discussed by Hunten et al. (1988), the residence times for physical adsorption depend exponentially on the temperature and increase rapidly as the temperature decreases. For surface temperature of 200 K, 100 K, and 80 K, the residence times for single-collisional physical adsorption are 3.6×10^{-7} s, 0.71, s, and 1000 s for sodium and 2.0×10^{-7} s, 0.16 s, and 150 s for potassium, respectively. These residence times are therefore an extremely small fraction of a second for surface temperatures typical of the sunlit hemisphere of Mercury (where the subsolar temperature varies between 575–708 K) so that the surface reservoir time for the atom is insignificant compared to a ballistic hop time. For nightside temperatures which may be a little cooler than 100 K, the residence times rapidly become much larger than 1 s and can then begin to compete more favorably with the ballistic hop times of atoms so that the nightside surface reservoir begins to capture the nightside ambient atoms. The effect of the long resident times for physical adsorption on cooler surface and the even more complex chemical adsorption (or other effective bonding of atoms to the surface) on hot or cooler surfaces will be collectively described in the atmospheric model in § 3, by a surface-sticking coefficient which is the probability that an atom upon encountering the surface will stick to it. The introduction of both the effective energy accommodation coefficient and the sticking coefficient provides the flexibility to cover a broad range of appropriate physical cases of interest, although it is realized that the two coefficients are not physically independent and must be specified in proper relationship.

2.5. *Transport Dynamics*

The transport dynamics of sodium and potassium atoms in the Mercury atmosphere are dependent upon the acceleration of gravity and solar radiation pressure produced by solar resonance scattering of sodium in the *D*-emission lines (5890 Å, 5896 Å) and by solar resonance scattering of potassium in their corresponding emission lines (7665 Å, 7699 Å). Solar radiation acceleration can have three major effects on the transport dynamics of sodium and potassium atoms. It can (1) cause source atoms to escape the planet even though their velocities are well below the two-body escape speed of the planet, (2) cause source atoms to be carried in one long ballistic trajectory to the nightside of the planet, or (3) drive a lateral (antisunward) transport of the ambient atoms along the surface. The importance of the third effect depends upon the relative magnitude of the solar radiation acceleration and gravity experienced by the atoms, while the importance of the first two effects depends, in addition, on the initial velocity of the source atoms. As an example in the lunar sodium atmosphere, solar radiation acceleration, which is at most a few percent of surface gravity, is not large enough to reduce the antisunward transport time for ambient sodium atoms to a value competitive with the photoionization lifetime so that the local density is determined by a balance of the local source rate and the photoionization lifetime (Smyth & Marconi 1995). At Mercury, however, the solar radiation acceleration for sodium and potassium varies significantly as Mercury moves about the Sun on its elliptic orbit shown in Figure 3 and may be comparable to the surface gravity over a significant portion of this orbit, as discussed below. The immediate consequence of this is that the typical transport time for accommodated ambient sodium atoms of $\sim 10^6$ s, estimated by Hunten et al. (1988) neglecting radiation acceleration, is reduced by as much as a factor of ~ 100 by including radiation acceleration. This much smaller transport time for accommodated ambient atoms, to be discussed later, is then competitive with the photoionization lifetime over a significant portion of the planetary orbit and hence provides an additional factor to balance the local source rate and hence to determine the local gas density. A similar situation also occurs for solar radiation acceleration and the potassium atmosphere of Mercury.

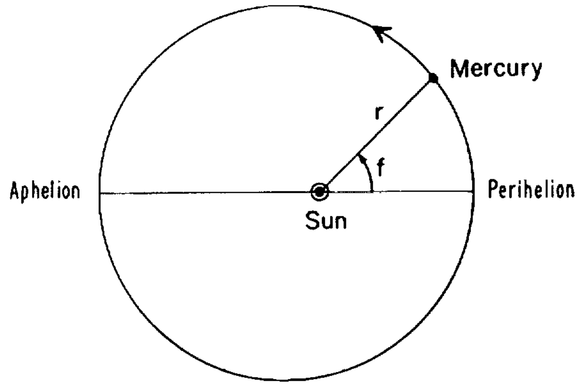

FIG. 3.—Orbit of Mercury. The orbit of Mercury about the Sun is shown to scale. The heliocentric distance *r* and the true anomaly angle *f* of Mercury are indicated.

As Mercury moves from perihelion to aphelion (i.e., from a true anomaly angle f of 0° to 180°, see Fig. 3), not only does the planet-Sun distance change by a factor of 1.52, but the Mercury-Sun radial velocity also varies from 0 km s^{-1} (at $f = 0°$) to ~ 10 km s^{-1} (at $f = 90°$) to 0 km s^{-1} (at $f = 180°$) again. This variation of the Mercury-Sun radial velocity alone modulates the amount of Doppler shift out of the solar Fraunhofer features and hence the solar resonance scattered brightness available to an atom in Mercury's atmosphere by an order of magnitude, as illustrated for sodium in Figure 4. By combining these two factors, the solar radiation acceleration varies by more than an order of magnitude for sodium and potassium, as shown in Figure 5. For sodium, the solar radiation acceleration varies from a maximum value of ~ 200 cm s^{-2} (i.e., $\sim 54\%$ of surface gravity) at true anomaly angles of $\pm 64°$ to a minimum value of 12.5 cm s^{-2} (i.e., 3.4% of surface gravity) at aphelion (true anomaly angle of 180°). For potassium, the solar radiation acceleration varies from a maximum value of ~ 293 cm s^{-2} (i.e., $\sim 79\%$ of surface gravity) at true anomaly angles of $\pm 47°$ to a minimum value of 24.5 cm s^{-2} (i.e., 6.6% of surface gravity) at aphelion. For the maximum value of solar radiation acceleration, the true anomaly angles of Mercury for potassium are closer to perihelion than for sodium since the solar Fraunhofer features above the Earth's atmosphere for potassium, as determined for us by Kurucz (1982), are more narrow than for sodium. The more narrow features cause the solar intensity to increase more rapidly and hence to compete closer to perihelion more favorably with the decreasing heliocentric factor. The relative importance of gravity and solar radiation pressure in determining the dynamical timescales of atom orbits in the atmosphere and their competition with the loss processes for these atoms are therefore highly dependent upon the true anomaly angle of the planet.

3. MODELS FOR THE SODIUM AND POTASSIUM ATMOSPHERES

Models for the sodium and potassium atmospheres of Mercury have been developed which incorporate the information discussed in the theoretical overview section above. The models are numerical and Monte Carlo in nature and are

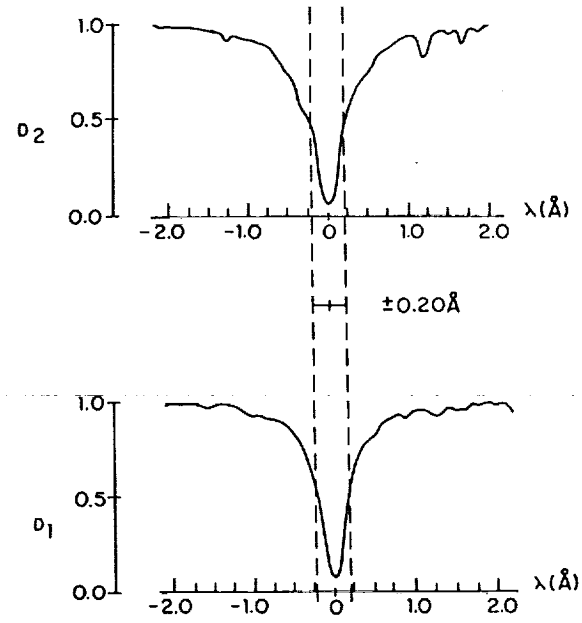

FIG. 4.—Solar Fraunhofer absorption features for the sodium D_2 and D_1 emission lines. The shapes of the two Fraunhofer features are shown, where the vertical scale is the fraction of the solar continuum brightness and the horizontal scale is the relative wavelength in angstroms. The zero on the wavelength scale is the rest wavelength position of the line (i.e., for zero radial velocity relative to the Sun). The dashed vertical lines indicate the maximum Doppler shift from the rest wavelength position achieved by the maximum radial motion (± 10.06 km s^{-1}) of Mercury in its orbit, which occurs at a true anomaly angle of ±90°.

appropriate for studying the importance of various physical processes and for simulating and analyzing various observational data acquired by ground-based facilities for the solar resonance scattered emission brightnesses in the D-lines of sodium atoms (5890 Å, 5896 Å) and potassium atoms (7665 Å, 7699 Å). The model calculates the three-dimensional sodium and potassium densities about the planet and also the projected two-dimensional column densities as well as the solar resonance scattered image brightnesses of the emission lines on the sky viewing plane. The dependence of the solar resonance scattered brightness on the instantaneous radial motion of each atom with respect to the Sun (which varies because of the solar Fraunhofer features) is included in the calculation, and only single scattered photon events in the optically thin limit are currently considered. For potassium emissions, this treatment is appropriate since the zenith and horizontal columns are optically thin. For the sodium emissions, the zenith (radial) column optical depth is estimated by Killen et al. (1990) to be ~1 somewhat away from the subsolar point, and the horizontal column optical depth can be several times larger, depending on the angular and vertical distributions of the atmosphere. Optically thick corrections for detailed radiative transfer calculations for sodium, which will therefore reduce the solar intensity somewhat below the optically thin levels considered here, will be addressed in future modeling studies. For emission brightness and gas density calculations, the model can adopt an initial source flux velocity-distribution on the surface of the body that is both spatially (i.e., longitude and latitude) and time dependent.

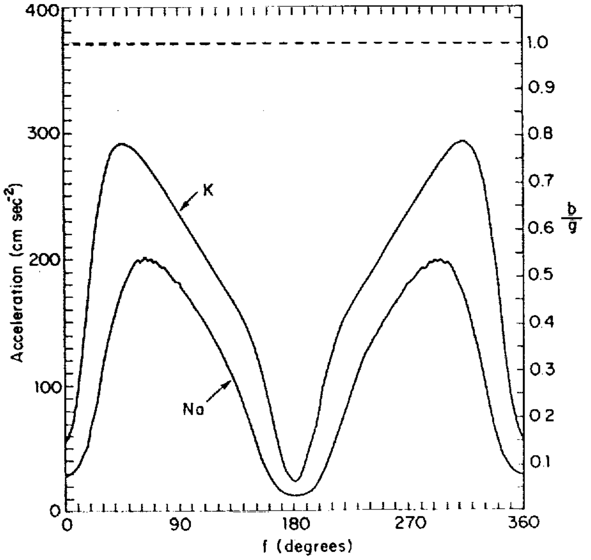

FIG. 5.—Solar radiation acceleration of sodium and potassium atoms at Mercury. The radiation acceleration experienced by stationary Na and K atoms in Mercury's atmosphere owing to solar resonance scattering in the sodium (5890 Å, 5896 Å) lines and the potassium (7665 Å, 7699 Å) lines is shown in absolute and surface gravity units as a function of true anomaly angle f for the planet on its elliptical orbit about the Sun.

The density of the exospheric atmosphere is calculated by following the trajectories of a large number of atoms that have initial conditions on the surface determined by an adopted source mechanism and that have collisions only with the surface (Smyth 1986a). The individual atom orbits are determined by numerically integrating the equations of motion using a fourth-order Runge-Kutta method with small but dynamically determined time steps and include the gravity of the Sun, the radially dependent acceleration of the gravity of the planet, and the antisunward directed solar radiation acceleration experienced by these atoms as they undergo solar radiation scattering in their emission lines. The gravity of the Sun contributes small centrifugal and Coriolis terms because of the motion of the planet about the Sun but is otherwise not directly significant near Mercury since the planet-Sun Lagrange radius (i.e., the average radial distance from the planet of the L1 and L2 Lagrange points where the solar, planetary and centrifugal forces balance) is large and varies between ~72 and ~109 planetary radii as Mercury moves from perihelion to aphelion. The dependence of the radiation pressure acceleration on the instantaneous radial velocity of each atom with respect to the Sun is included as well as the shadow of the Sun cast by the planet. This instantaneous radial velocity includes both the (generally larger) planet-Sun radial velocity which gives rise to the solar radiation acceleration shown in Figure 5 and the (generally smaller) Sun-planet component of the instantaneous atom-planet velocity which alters to some extent the value of the solar radiation acceleration shown in Figure 5. When the atom orbit encounters the surface of the body, its gas-surface interactions are described by a sticking coefficient (i.e., minimum value: 0 = no sticking; maximum value: 1 = 100% sticking) and the energy accommodation coefficient β (i.e., minimum value: 0 = no accommodation; maximum value: 1 = 100% accommodation to the local surface temperature). The two coefficients may be specified in different combinations to simulate a variety of physical and chemical conditions. If the atom bounces on the surface (i.e., if the sticking coefficient is not unity), its velocity vector is directed upward with a randomly selected angle and with a velocity magnitude (i.e., corresponding energy $E_{\rm out}$ in eq. [1]) appropriate to its accommodation coefficient, where E_T is given by the most probable energy of a Maxwell-Boltzman velocity distribution at the local surface temperature. The trajectory calculation is then continued with these new initial conditions. In the density calculation, the photoionization lifetime of the atom as it moves on its trajectory is also included, taking into account the Sun's shadow.

4. APPLICATION OF THE MODELS

4.1. *Modeling Studies for Source Atoms*

The escape of sodium and potassium source atoms from the atmosphere can be greatly enhanced by the action of solar radiation acceleration. At the surface of the planet, the two-body gravitational escape speed of 4.25 km s^{-1} is much larger than the average speeds of ambient atoms accommodated to the subsolar surface temperature, which range from 0.72 to 0.64 km s^{-1} for sodium and from 0.55 to 0.49 km s^{-1} for potassium as Mercury moves from perihelion to aphelion. For sodium, the contribution of source atoms to the atmosphere for maximum and minimum solar radiation acceleration conditions is shown as a function of the speed of the atoms in Figure 6 as given by Smyth (1986a). For the maximum value of solar radiation acceleration, sodium atoms begin to escape at speeds of $\sim$2.0 km s^{-1} while at the minimum value, sodium only escapes for speeds somewhat in excess of 3 km s^{-1}, which are much closer to the two-body gravitational escape speed of 4.25 km s^{-1}. The cases of maximum solar radiation acceleration for sodium and potassium are compared in Figure 7. In contrast to sodium atoms that begin to escape at speeds of $\sim$2.0 km s^{-1}, potassium atoms begin to escape at speeds of $\sim$1.6 km s^{-1} or less. Many source atoms (and also many nonthermal ambient atoms, if they exist) with speeds considerably below the two-body gravitational escape speed of 4.25 km s^{-1} will then be able to escape the planet and produce a comet-like coma.

The spacetime modulation of the bound source atom trajectories as a function of the true anomaly angle of Mercury also changes their surface impact locations and hence changes the initial surface distribution of the ambient atoms created. The effective potential for sodium atoms in Mercury's atmosphere as given earlier by Smyth (1986a) and their corresponding spacetime distribution of bound and escaping source atoms about the planet for an initial atom speed of 2.6 km s^{-1} are illustrated in Figure 8. This spacetime modulation clearly alters the number of ambient atoms that are created in a selected spatial region of the atmosphere by the source atoms. For source atoms ejected uniformly from the sunlit hemisphere with a speed of 2.6 km s^{-1}, a comparison of the sodium column density and the corresponding D_2 emission brightness (assuming optically thin conditions and no ambient atom atmosphere) for three different values of the solar radiation acceleration is shown in Figure 9. A direct and significant population of the nightside sodium column density of the planet by dayside source atoms is absent for the planet at aphelion (minimum solar radiation acceleration), very evident for the planet at a true anomaly angle of 228° (intermediate solar radiation acceleration), and largely escaping for the planet at a true anomaly angle of 270° (near maximum solar radiation acceleration). In the intermediate case, the significant bound nightside density is caused by sodium atoms that enter the planetary shadow without sufficient velocity to escape the planetary gravity when the solar radiation acceleration abruptly drops to zero in the shadow region. The remote detection of the nightside sodium column density in the D_2 emission line is, however, completely masked because of the planetary shadow in the first two positions of the planet and is only weakly seen in the third position of the planet because a small fraction of the escaping sodium atoms extends spatially beyond the planetary shadow. The initial spatial source distribution for ambient atoms created on the surface by the source atoms is different in the three cases and will lead to a different density distribution for the ambient atom atmosphere as the ambient atoms migrate about on the surface.

For the ambient atom atmospheric density to dominate over the source atom atmospheric density, the number of ballistic hops needs to be much larger than unity (i.e., sticking would needs to be unimportant). The range of ballistic hop (flight) times and maximum altitudes achieved for sodium and potassium atoms ejected radially from the surface at the subsolar point is given in Table 1 for their most probable speed at aphelion (only 11% smaller than at perihelion) and also for a nonthermal speed of 2.6 km s^{-1}. The minimum altitudes and hop times correspond to a true anomaly angle of 296° for sodium and 313° for potassium where the solar radiation acceleration is largest, while the maximum altitudes and hop times correspond to a true anomaly angle of 180° (aphelion) where the solar radiation acceleration is a minimum. The photoionization lifetimes vary from a value of 1.75–3.29 hr for sodium and 1.09–2.24 hr for potassium as the solar radiation acceleration varies from its maximum to its minimum value. In Table 1, the ballistic hop times for the thermal atoms imply that sodium will have $\sim$28–34 hops and that potassium will have $\sim$26–32 hops in one photoionization lifetime, whereas the ballistic hop times for the nonthermal atoms imply that sodium will have $\sim$5–6 hops and that potassium will have $\sim$3–4 hops. If the ambient atoms readily accommodate to the surface temperature as expected for the hot subsolar hemisphere and if surface sticking is not important, the ambient atoms should dominate the source atoms in their contribution to the density of the sunlit atmosphere. This situation would then be consistent with the sodium line profile observation of Potter & Morgan (1987). In contrast, if sticking were important and the

TABLE 1

SUBSOLAR ALTITUDE AND BALLISTIC FLIGHT TIME OF Na AND K ATOMS

Atom	Surface Ejection Speed (km s^{-1})	Source	Maximum Altitude (km)	Ballistic Flight Time (s)
Na......	0.6449	Thermal (MP)	36–55	227–343
	2.6000	Nonthermal	653–1310	1080–2330
K	0.4945	Thermal (MP)	18–31	149–251
	2.6000	Nonthermal	556–1150	897–2027

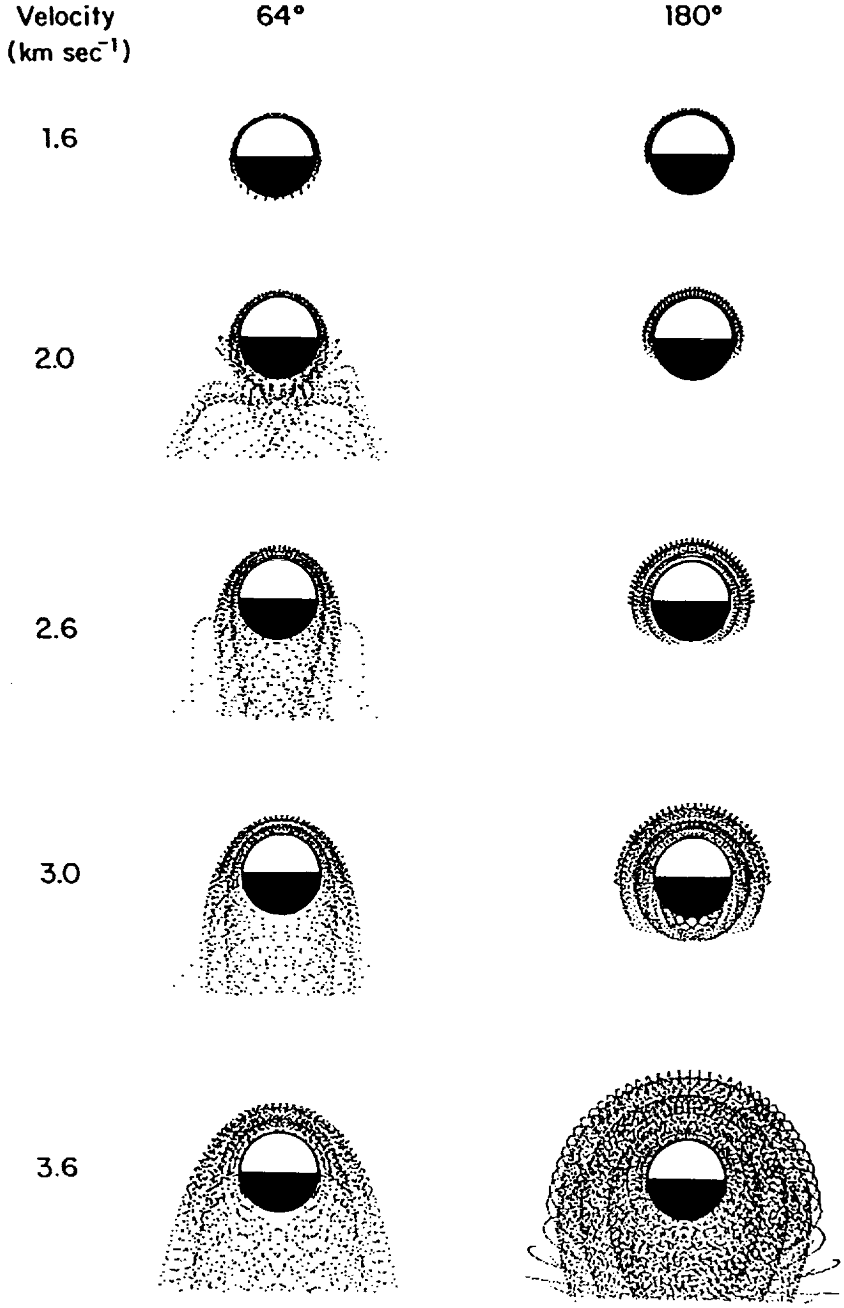

FIG. 6.—Comparison of the spatial character of sodium at maximum and minimum solar radiation acceleration conditions. The shape and size of the atmosphere for five ejection speeds are shown in dot plot representation for the true anomaly angle of the planet at 64° (maximum solar radiation acceleration) and 180° (minimum solar radiation acceleration). Atoms are ejected isotropically from the sunlit equator of the planet. A dot occurs at a time interval of 225 s along each of the 259 atom trajectories used in the simulation. For the field of view selected, flight times of most nonplanet colliding trajectories were 1–3 hr, with a maximum value of 4 hr imposed. Ballistic trajectories were terminated upon colliding with the surface.

source atoms were somewhat thermal in nature, it would then be difficult to distinguish source atoms from ambient atoms in the observational data, although a much larger upward atom flux would be required to sustain a pure source-atom atmosphere.

The spacetime modulation of source atoms about the planet also provides a spacetime varying heavy ion source for the planetary magnetosphere since the dynamical flight times for sodium and potassium atoms are comparable with their short photoionization times. For sodium, two different spatial distributions for the source atom atmosphere are shown and compared with the nominal location of the magnetopause (i.e., subsolar altitude of 1460 km) and the bow shock in Figure 10. It is immediately obvious that the spatial distribution of the instantaneous heavy ion creation rates will be very different for these two different locations of the planet in its orbit. The ultimate fate of these heavy ions as they undergo magnetospheric convection is not well understood (Ip 1987, 1993), but a significant fraction of these ions, which are accelerated in the planetary magnetic and electric fields, will likely collide with

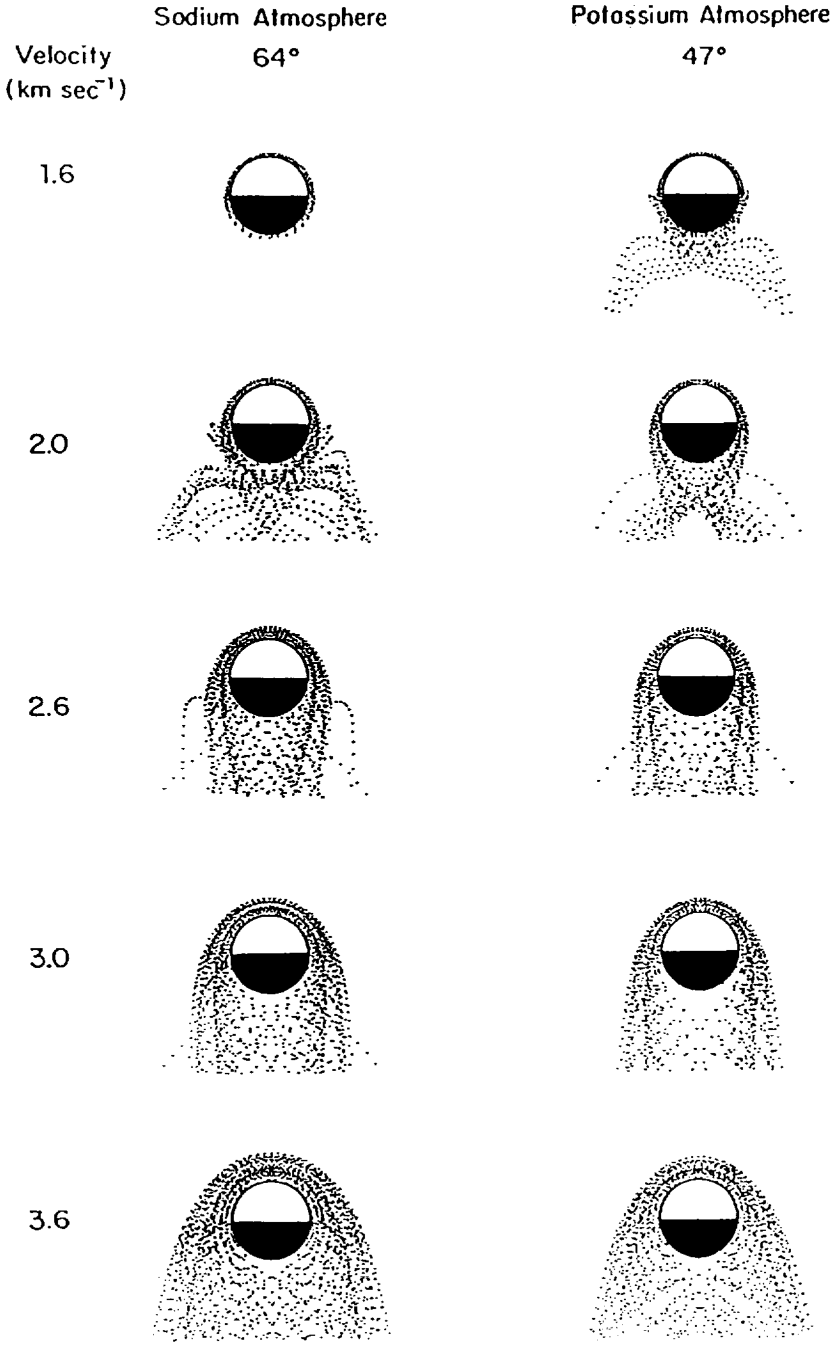

FIG. 7.—Comparison of the spatial character of the sodium and potassium atmospheres of Mercury at maximum solar radiation acceleration conditions. The shape and size of the atmosphere for five ejection speeds are shown at a true anomaly angle of 64° for sodium and at a true anomaly angle of 47° for potassium. Source conditions and description are the same as in Fig. 6.

the surface while the remaining ions will be lost to the solar wind. If sufficiently energetic, the heavy ions that encounter the surface may liberate neutrals by ion sputtering and hence become part of the mechanism for producing the source atoms.

4.2. *Modeling Studies for Sodium Ambient Atoms*

For sodium, the only observation (Potter & Morgan 1987) for the high-resolution spectrum of the D_2 emission line (5890 Å) suggests that a significant fraction of the atmosphere is likely to be nearly thermal and hence may be dominated by ambient atoms. For the sodium atmosphere, the zenith column density has also been shown to be anticorrelated with the solar radiation acceleration by Potter & Morgan (1987). This anticorrelation has been identified with an antisunward lateral transport of ambient atmosphere sodium atoms toward the terminator and into the nightside of the planet driven by the variable solar radiation acceleration (Smyth 1986b, 1989; Ip 1986, 1990). In its most basic physical description, this situation may be viewed as a relative competition between the photoionization lifetime and the lateral (antisunward) migra-

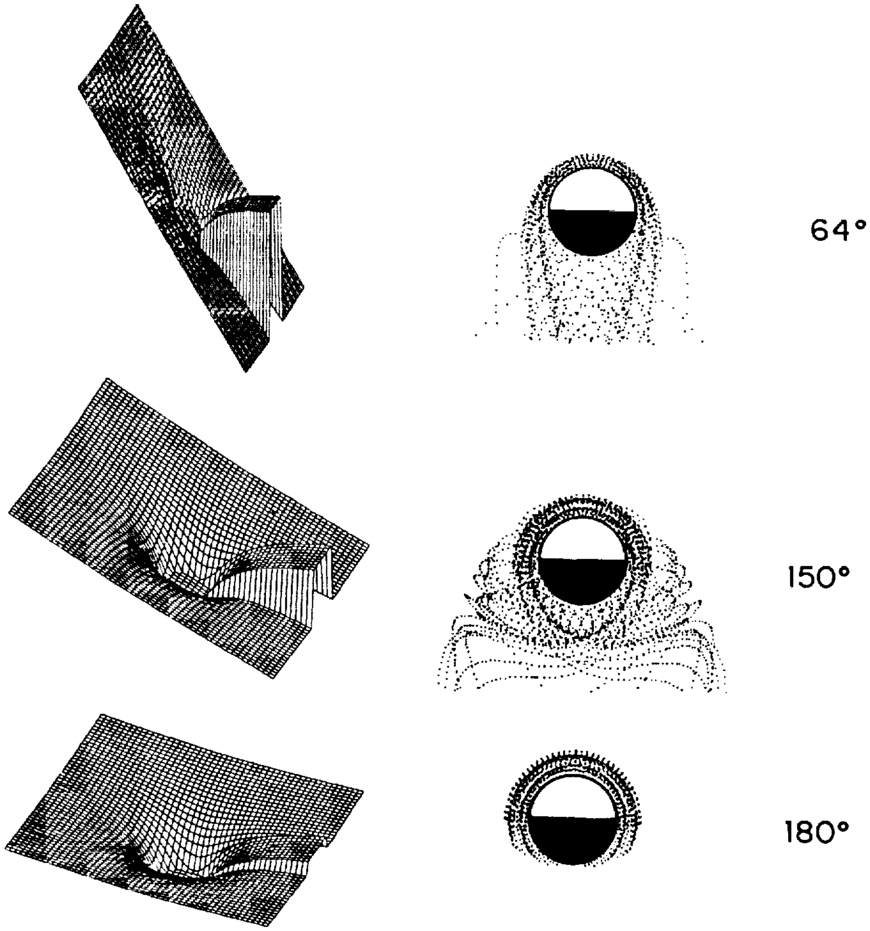

FIG. 8.—The effective potential and atmosphere for sodium. The effective potential (Smyth 1986a) for sodium is compared to the changing spatial character of the source atom atmosphere depicted in the dot plot format for the three indicated true anomaly angles. The initial velocity of the sodium atoms ejected isotropically in the plane of the page from the sunlit limb is 2.6 km s^{-1}. The dot plot description is the same as in Fig. 6.

tion time of sodium atoms which then determines the local gas density. For accommodated ambient atoms near the subsolar point, the acceleration of gravity and the radial component of the solar radiation acceleration mostly add, while the component of solar radiation acceleration tangent to the surface is nearly zero. The local height of the atmosphere will therefore be depressed as noted in Table 1, and the lateral (antisunward) transport driven by the solar radiation acceleration will be its weakest and hence least capable of competing with the photoionization lifetime. For accommodated ambient atoms in the sunlit hemisphere but more distant from the subsolar point, the direction of the solar radiation acceleration will be more nearly tangent to the surface, and hence the lateral transport rate toward the terminator will be larger and hence more capable of competing with the photoionization lifetime. The ability of the lateral transport rate (or more simply a lateral migration time to the terminator) to compete with the photoionization lifetime as a function of the surface location and the true anomaly angle of the planet is explored below in order to investigate more fully the observed anticorrelation.

4.2.1. *Migration Times to the Terminator*

The average migration time to reach the terminator for an ensemble of atoms ejected isotropically with an initial velocity of 1 km s^{-1} from a point source on the surface located an angle Φ from the subsolar point has been calculated for sodium and potassium using the model described in § 3. These model calculations for the ambient atom atmosphere in the sunlit atmosphere have been undertaken for a range of the energy accommodation coefficients but with no sticking of atoms to the surface (i.e., the sticking coefficient is zero) and for different true anomaly angles of Mercury in order to include the variation of the solar radiation acceleration. Selected average migration times, given primarily for sodium atoms, are summarized in Table 2 and provide a focused overview of the effects of solar radiation acceleration.

The limiting case for the fastest migration times is obtained for the unrealistic but most energetic gas-surface interaction where there is no surface accommodation (i.e., elastic bouncing on the surface, $\beta = 0$). This limiting case is important because it documents the unimpeded impact of solar radiation acceleration and establishes a control case for the more realistic cases where $\beta \neq 0$. For sodium, the migration times for $\beta = 0$ are listed in Table 2 for six selected true anomaly angles and include the case of maximum solar radiation acceleration ($f = 64°$) and the case of minimum solar radiation acceleration ($f = 196°$) which is achieved for atoms with values of Φ somewhat removed from the subsolar point, where the antisunward motion of sodium atoms in the atmosphere is canceled by a small sunward motion of the planet. As expected, the migra-

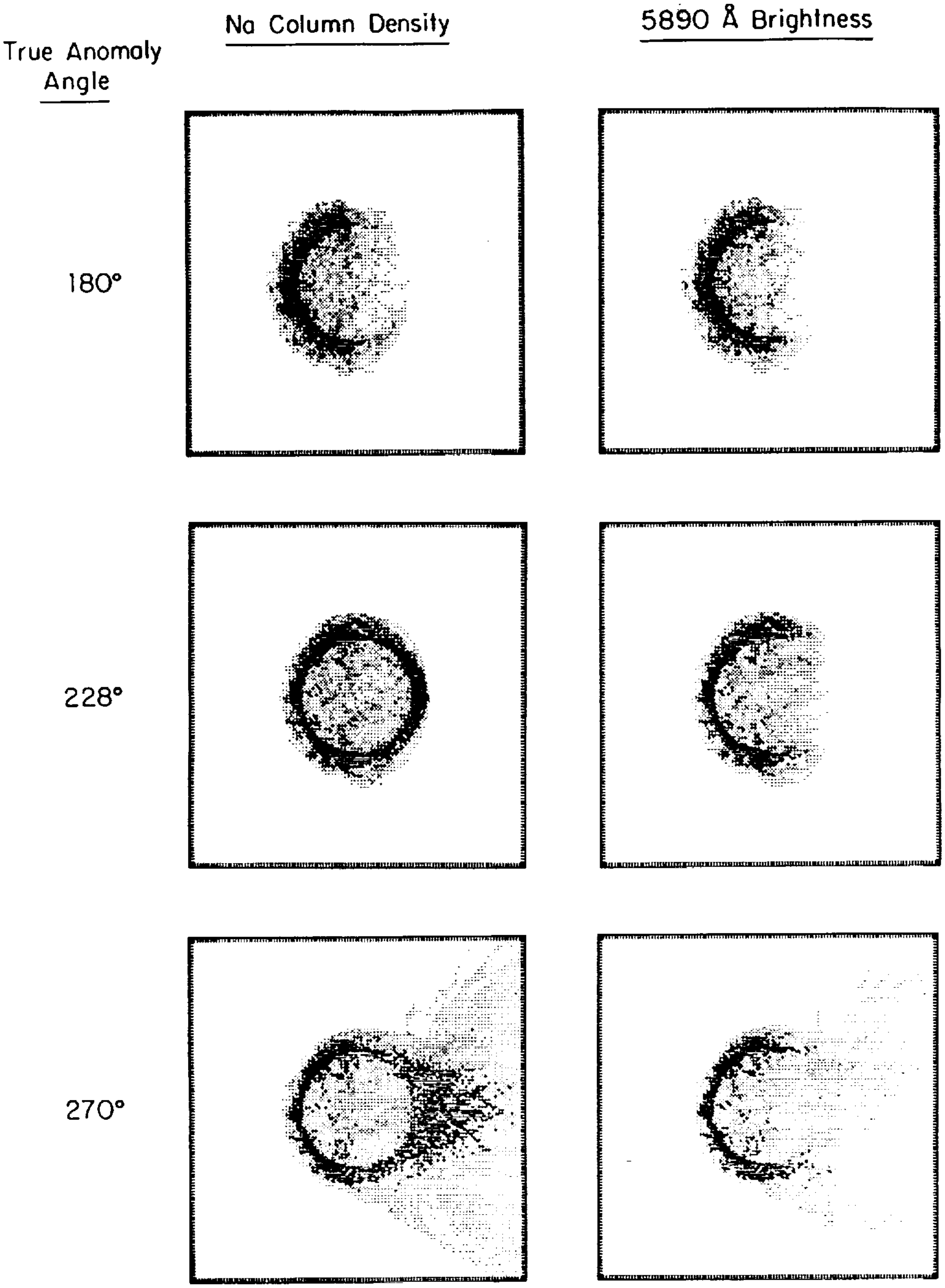

FIG. 9.—Model calculation for the sodium atmosphere of Mercury. The sky-plane sodium column density and D_2 emission brightness are compared in a shaded plot format (dark is more dense/intense) for three true anomaly angles of Mercury, where the radiation acceleration is 12.45 cm s^{-2} (a minimum at 180°), 101.34 cm s^{-2} (moderate at 228°), and 180.86 cm s^{-2} (near maximum at 270°). Sodium is ejected isotropically from the sunlit hemisphere (toward the left) at 2.6 km s^{-1}. Atom trajectories upon collision with the surface are terminated so as to illustrate the spatial distribution created only by the initial source atoms. The effect of the planetary shadow on the D_2 emission brightness is readily apparent.

tion time decreases as the solar radiation acceleration increases, with values for atoms starting at the subsolar point differing by a factor of ~ 10 and values for atoms starting nearer the terminator differing by a factor of ~ 20. From Table 2, it is clear that either near aphelion or perihelion, where the solar radiation acceleration is weak, the migration times for sodium are only competitive with the photoionization lifetime very near the terminator (i.e., very near $\Phi = 90$). However, for a wide range of true anomaly angles about 64°, where the solar radiation acceleration is a maximum, it is clear that the migration time of sodium is quite competitive with the photoionization lifetime over all of the sunlit surface, including the subsolar point (i.e., $\Phi = 0$).

The effect of more realistic, nonzero values for the energy accommodation coefficient β is to moderate the antisunward transport rate produced by the solar radiation acceleration. An

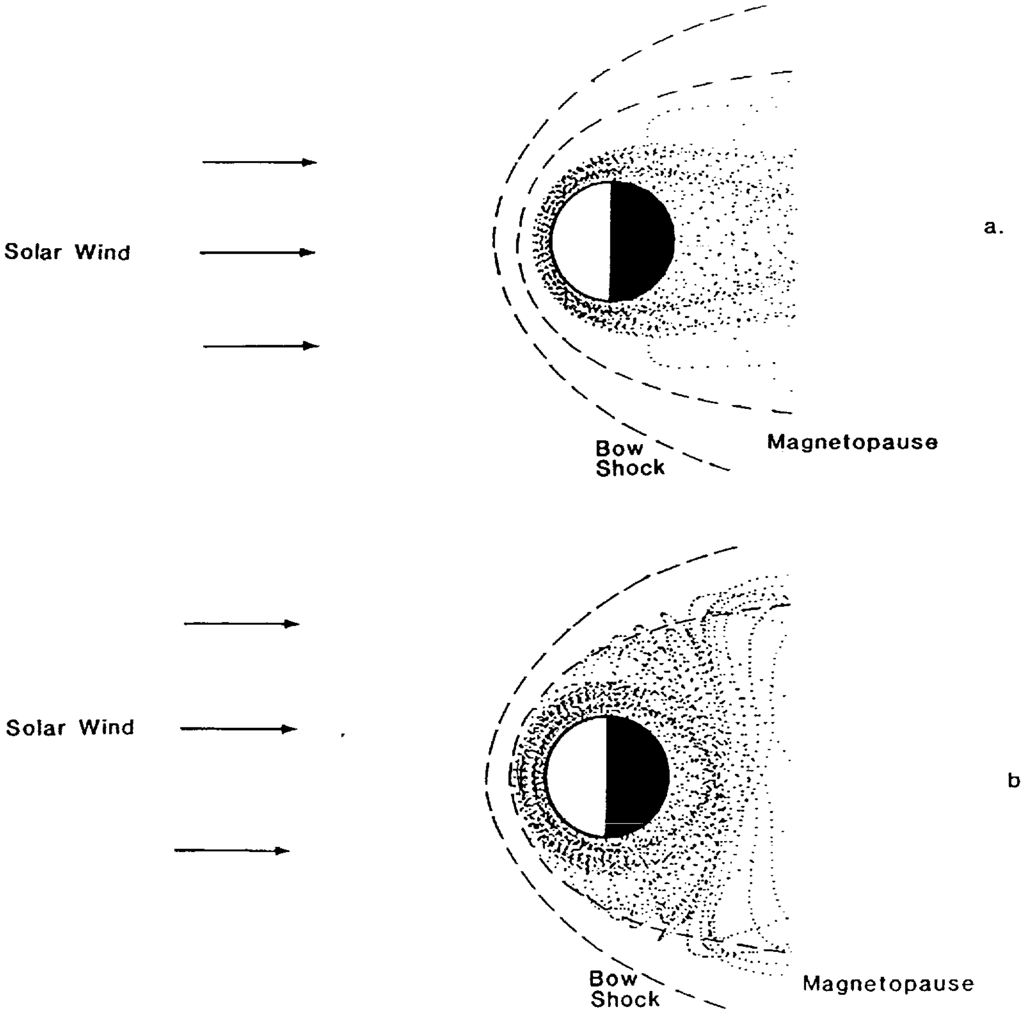

FIG. 10.—Comparison of the sodium source atom atmosphere and the magnetosphere of Mercury. The spatial extent of the source atom atmosphere and the nominal location of the planetary magnetopause and bow shock are shown to scale for Mercury at a true anomaly angle of 64° in (*a*) and 150° in (*b*). The initial velocity of the sodium atoms ejected isotropically in the plane of the page from the sunlit limb is 2.6 km s^{-1}. The dot plot description is the same as in Fig. 6.

TABLE 2

MIGRATION TIMES FOR THE AMBIENT ATOM ATMOSPHERE

	MIGRATION TIME TO THE TERMINATOR (hr)				PHOTOIONIZATION LIFETIME (hr)	TRUE ANOMALY ANGLE
SPECIES	($\Phi = 0°$)	($\Phi = 30°$)	($\Phi = 60°$)	($\Phi = 80°$)		
			$\beta = 0.0$			
Na......	10.8	10.7	6.4	2.0	1.4	0°
Na......	2.9	2.6	1.8	0.79	1.5	30
Na......	2.8	1.7	0.93	0.41	1.7	64
Na......	3.7	3.0	1.6	0.54	2.8	134
Na......	14.9	13.0	8.0	3.9	3.3	180
Na......	31.9	29.0	16.0	7.4	3.2	196
K.......	2.6	1.8	0.83	0.33	1.1	47
			$\beta = 0.5$			
Na......	10.0	6.2	2.2	0.58	1.7	64
K.......	12.5	5.7	1.8	0.53	1.1	47
			$\beta = 1.0$			
Na......	11.7	7.2	3.0	0.96	1.7	64
K.......	14.6	7.1	3.0	0.73	1.1	47

increase in the energy accommodation coefficient causes the migration times to increase since the atom can no longer accumulate the effective potential energy that it acquires in the elastic case as it moves away from the subsolar point (see the potential curves in Fig. 8). As indicated for $\beta = 0.5$ and $\beta = 1.0$ in Table 2 and also graphically in Figure 11, the migration time for sodium is now competitive with the photoionization lifetime for ambient atoms which originate near or within about 30° of the terminator when Mercury is located at a true anomaly angles of 64°, where the solar radiation acceleration is a maximum. When the point source of ambient atoms is closer to the subsolar point (Φ somewhat less than 60°), the moderation effect of the nonzero energy accommodation coefficient causes the migration time to increase sufficiently so as to be unable to compete with the photoionization lifetime. It should be emphasized that in the absence of solar radiation acceleration, the migration times (which would then be only weakly driven in the antisunward direction by the surface temperature gradient) are quite large on the sunlit hemisphere and are incapable of competing with the photoionization lifetime. For Mercury located at a true anomaly angle of 64°, for example, the sodium migration times for no radiation acceleration and for a source point located at $\Phi = 30°$ and $\Phi = 60°$ are, respectively, 120 hr and 99 hr for $\beta = 0.5$ and 143 hr and 102 hr for $\beta = 1.0$. These migration times are larger than the corresponding migration times in Table 2 (which include solar radiation acceleration) by a factor, respectively, of 19 and 45 for $\beta = 0.5$ and by a factor, respectively, of 20 and 34 for $\beta = 1.0$. These migration times for no solar radiation acceleration are, however, a factor of ~ 2 to 3 times smaller than the typical migration times $\sim 10^6$ s (i.e., 280 hr) estimated by Hunten et al. (1988) and based on a simple random walk expression that ignored the solar radiation acceleration and the surface temperature gradient.

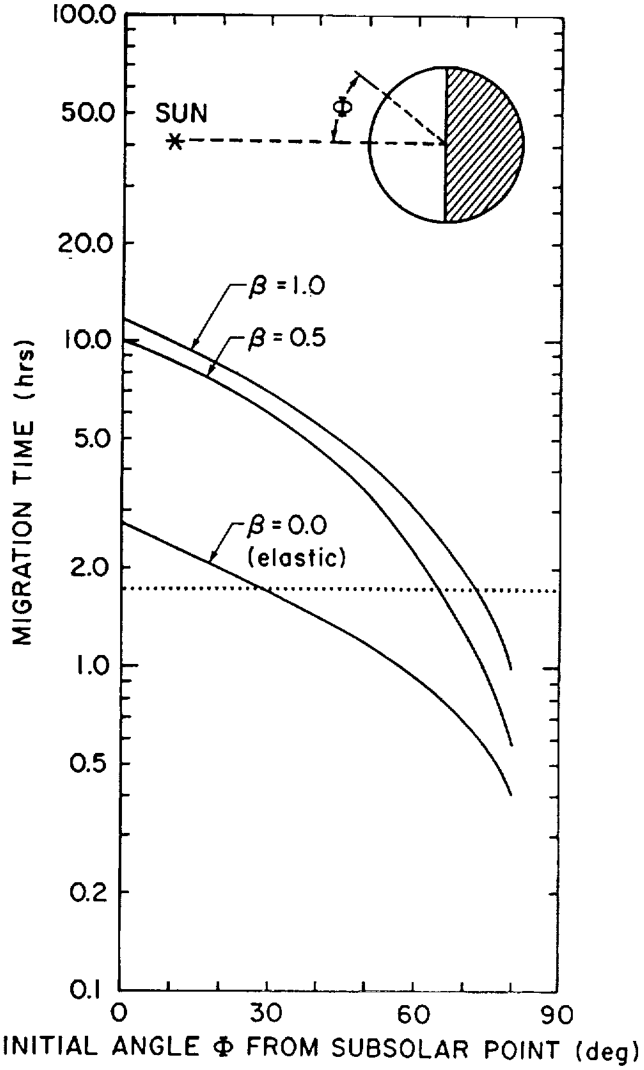

FIG. 11.—Migration time of sodium atoms to the terminator. The migration time to the terminator for an ensemble of atoms initially starting as a surface point source at an angle Φ from the subsolar point is shown for a true anomaly angle of 64° (maximum solar radiation acceleration case) and for three different values of the energy accommodation coefficient β. Atoms are initially emitted isotropically from the surface source point with a speed of 1 km s^{-1} and acquire a random upward directed velocity vector upon bouncing on the surface. The dotted line indicates the value of the photoionization lifetime for sodium at Mercury for the true anomaly angle of 64°.

For ambient potassium atoms, a similar competitive pattern to that of sodium exists between the migration time and the photoionization lifetime, although the migration times in Table 2 are given only for the maximum solar radiation case ($f = 47°$). For potassium, however, the competition between the migration time and the photoionization lifetime is actually a little less severe than for sodium because the shorter migration times for potassium produced by the larger solar radiation acceleration are more than compensated by the significantly shorter potassium photoionization lifetime.

For the optimal (and typical) viewing geometry of Mercury from Earth, where the Earth-planet-Sun angle is near 90°, an angle Φ of 60° is already halfway from the subsolar point to the terminator in the projected sky-plane view of the planet (see the insert in Fig. 11). In this case, most of the projected sky-plane area of the planet's sunlit atmosphere occurs for the angular region $60° \leq \Phi \leq 90°$, where the migration time and the lifetime can be competitive. This angular region is the same as sampled by the north-south observing slit of Potter & Morgan (1987). Migration times for sodium atoms from $\Phi = 60°$ to the terminator have therefore been calculated as a function of the true anomaly angle of Mercury and are shown in Figure 12 for different values of the energy accommodation coefficient. Examination of Figure 12 shows that even for $\beta = 0.5$ to $\beta = 1.0$ the migration time is competitive with the photoionization lifetime over a significant range of the true anomaly angle of Mercury about ±64°. This competition then provides a natural mechanism to explain the anticorrelation in the solar radiation acceleration and the sodium column density observed by Potter & Morgan (1987) using a north-south slit on the sunlit planet near (and parallel to) the terminator.

For that portion of the planet from $\Phi = 60°$ to the terminator, the variation of the sodium column density and emission brightness with true anomaly angle does not only depend upon the migration time and the lifetime of sodium shown in Figure 12, but also upon how the sodium source varies with the true anomaly angle. Four different variations for the source are shown in Figure 13 normalized to unity at a true anomaly angle of zero. The impact vaporization source as determined by Morgan (1989), which varies more than the inverse square heliocentric distance source, depends upon both the heliocentric distance and the orbital velocity of Mercury. An approximate expression for the average zenith column density

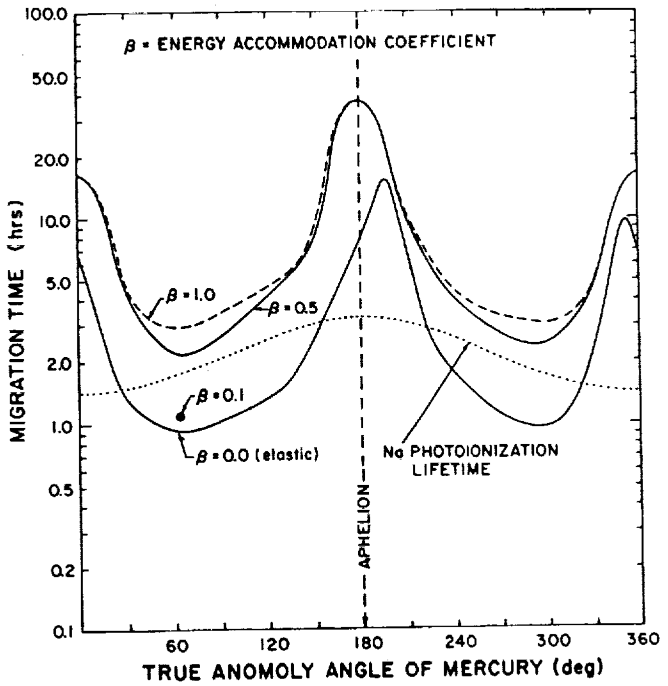

FIG. 12.—Migration time of sodium atoms from $\Phi = 60°$ to the terminator. The migration time is shown as a function of the true anomaly angle of Mercury for three values of the energy accommodation coefficient β by the two solid lines and the dashed line. The sodium photoionization lifetime is shown by the dotted line for comparison.

of sodium $\bar{N}$ and the associated average D_2 emission column brightness $\bar{I}$ for the spatial region from $\Phi = 60°$ to the terminator can be related to the surface source flux ϕ, the photoionization lifetime τ, and the migration time t_M as follows:

$$\bar{N} = \phi\tau(1 - e^{-t_M/\tau}) , \quad (2)$$

$$\bar{I} = g_{D_2}\phi\tau(1 - e^{-t_M/\tau}) , \quad (3)$$

where g_{D_2} is the optically thin g-value, i.e., the number of D_2 photons emitted per atom per second from the line-of-sight gas column as determined by solar resonance scattering for the instantaneous radial motion between Mercury and the Sun.

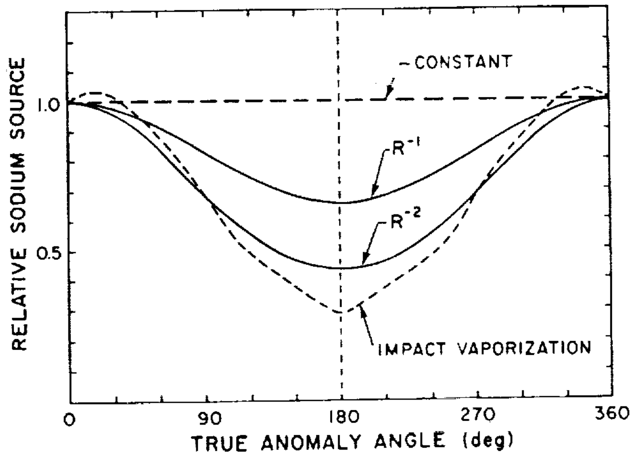

FIG. 13.—Orbital variations of four sources for sodium. The relative variation of the four different sources as a function of the true anomaly angle of Mercury is shown. The impact vaporization source was provided by Morgan (1989).

4.2.2. *Constant Source*

For a constant source (i.e., ϕ = constant), the sodium column density and D_2 emission brightness calculated from the expressions (2) and (3) above are shown in Figure 14. The sodium surface source flux ϕ has been chosen to be 2.0×10^7 atoms cm^{-2} s^{-1} in order to obtain the approximate value and range of the measured D_2 brightness and its inferred sodium column density. In the upper portion of Figure 14 for $\beta = 0$, the minimum column density occurs at true anomaly angles of 64° and 296° where the solar radiation acceleration is maximum, and the maximum column density occurs at a true anomaly angle of 196° where the solar radiation acceleration (including the antisunward motion of the elastic bouncing atoms) is minimum and where the photoionization lifetime is near its maximum. The column density has a maximum-to-minimum ratio of ~4.4. For energy accommodation coefficients of $\beta = 0.5$ and $\beta = 1.0$, the overall variation of the column density is diminished to about a factor of ~2.4 and ~2.3, respectively, which is more in accord with the overall factor of about 2 observed by Potter & Morgan (1987). The maximum column density for both of these latter cases occurs at aphelion where the photoionization lifetime is maximum. Most of the column density change from perihelion to aphelion occurs because of the factor of 2.30 in the photoionization lifetime. At a true anomaly angle of 64°, the column density minimum for $\beta = 0.5$ is small and for $\beta = 1.0$ has almost vanished entirely, so that the column density profile is somewhat constant over half of the true anomaly range (i.e., from −90° to +90°). This somewhat constant behavior occurs because the increasing photoionization lifetime and hence potential residence time for atoms in the atmosphere (as the true anomaly angle departs from zero) is effectively offset by an increasing transport loss of atoms to the nightside of the planet. This more nearly constant column density for $\beta = 0.5$ and $\beta = 1.0$ produces an enhancement in the D_2 emission brightness in comparison to the $\beta = 0$ case, as can be seen in the lower portion of Figure 14. In addition to variations in the column density, the D_2 emission brightness profiles also include the heliocentric-distance and radial velocity–dependent g-value. The D_2 brightness peaks at a true anomaly angle of 90° and 270° (except for the peculiar elastic $\beta = 0$ case) since the radial velocity–dependence of the g-value peaks at ±90° and the heliocentric dependence of the photoionization lifetime and the g-value cancel for a constant flux. This cancellation caused the D_2 brightness at perihelion and aphelion to be very nearly the same even though the column density has its maximum value near (or at) aphelion.

4.2.3. *Inverse Square of the Heliocentric Distance Source*

Similar results to those in Figure 14 are given in Figure 15 for a surface source that depends upon the inverse square of the heliocentric distance R:

$$\phi = \phi_0(R_p/R)^2 , \quad (4)$$

where R_p is the heliocentric distance of Mercury at perihelion. The column density and D_2 emission brightness in Figure 15 are determined for $\phi_0 = 4.6 \times 10^7$ atoms cm^{-2} s^{-1} in order to obtain the approximate range of brightness specified by the observations. This source, which is appropriate for photosputtering or ion sputtering, is particularly interesting since the quantity $\phi\tau$ is constant in the expression (2) for $\bar{N}$ so that the column density depends only upon the ability of the transport loss to alter the residence time of a sodium population that

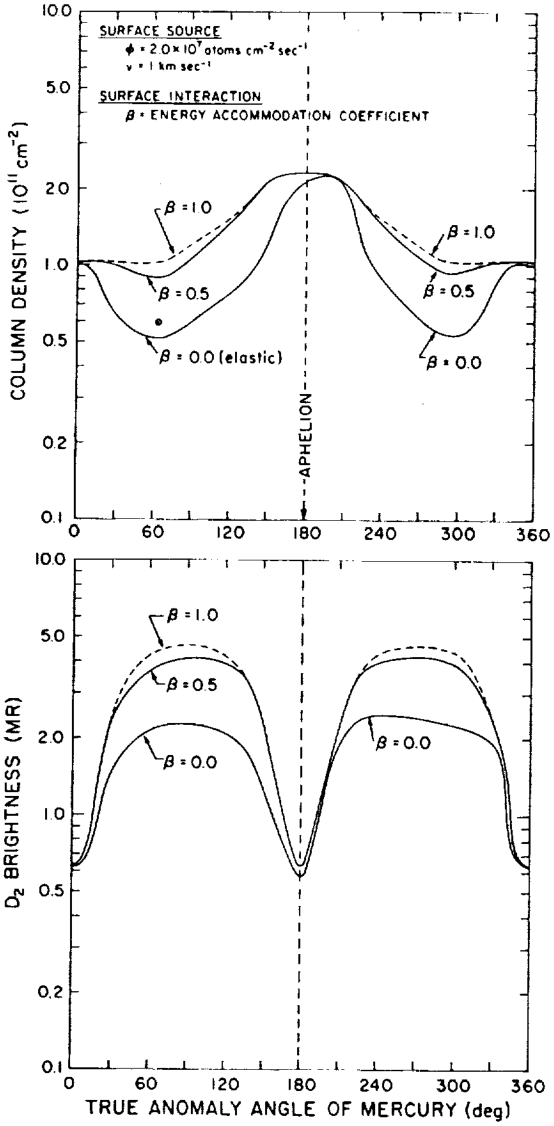

FIG. 14.—Model simulation for the sodium atmosphere from $\Phi = 60°$ to the terminator. The model simulation shows the dependence of the sodium column density and D_2 brightness on the true anomaly angle of Mercury for the constant surface source indicated and the migration time and photoionization lifetime given in Fig. 12.

would otherwise be constant. The column density profiles in Figure 15 have nearly the same maximum values near perihelion (0°) and aphelion (180°) where the slow transport cannot appreciably affect the sunlit constant sodium population before it is photoionized. The column density profiles have broad minima centered near true anomaly angles of 90° and 270°. The minima are centered near 90° and 270° because the heliocentric distance dependences of the solar radiation acceleration and the photoionization lifetime approximately cancel, leaving in the migration time the velocity dependence of the solar radiation acceleration which is maximum at these two true anomaly angles. For elastic atom collisions with the planetary surface ($\beta = 0$), the column density varies by a factor of ~ 2.5. For the nonzero energy accommodation coefficients, however, this variation is reduced significantly because of the longer migration times. For $\beta = 0.5$ and $\beta = 1.0$, the column density variation is small and only ~ 1.4 and ~ 1.2, respectively. These higher column densities for the larger values of β produce a larger D_2 sodium brightness as indicated in the lower portion of Figure 15. The D_2 brightness peaks at a true anomaly angle of 64° and 296° (except for the peculiar elastic $\beta = 0$ case) since $\phi\tau$ is constant and the combined radial-velocity and the heliocentric-distance dependence of the g-value peaks at $\pm 64°$. In contrast to Figure 14, the minimum D_2 brightness in Figure 15 at aphelion is ~ 2.3 times smaller than at perihelion since the column density is essentially the same and the g-value has its full R^{-2} dependence.

4.2.4. *Impact Vaporization Source*

Similar results to those in Figures 14 and 15 are given in Figure 16 for a surface source that has the true anomaly angle dependence denoted by $S(f)$ for the impact vaporization source given in Figure 13:

$$\phi = \phi_0 S(f)\,. \tag{5}$$

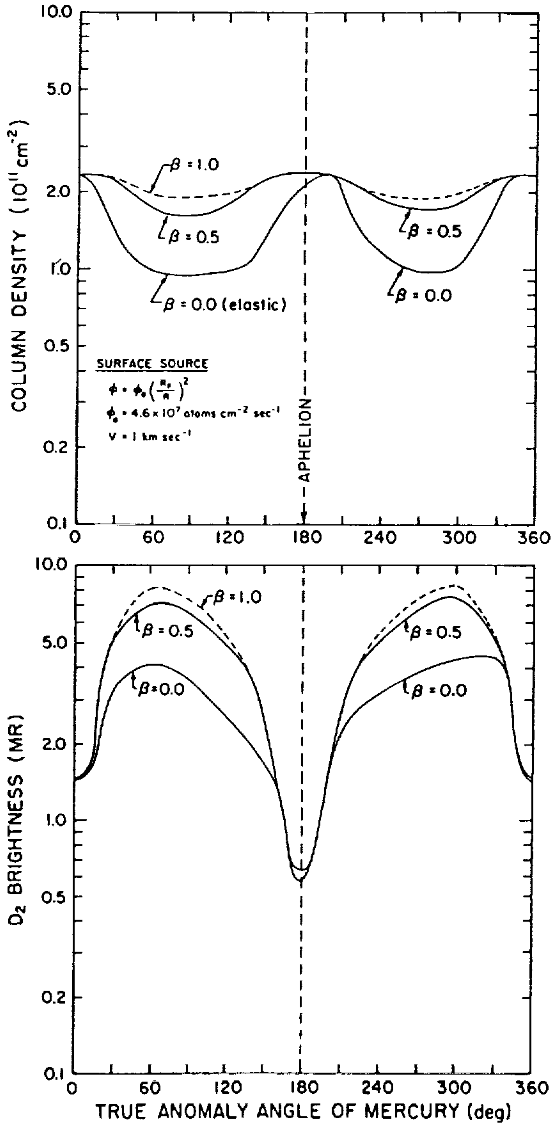

FIG. 15.—Model simulation for the sodium atmosphere from $\Phi = 60°$ to the terminator. The model simulation shows the dependence of the sodium column density and D_2 brightness on the true anomaly angle of Mercury for the R^{-2} source indicated and the migration time and photoionization lifetime given in Fig. 12.

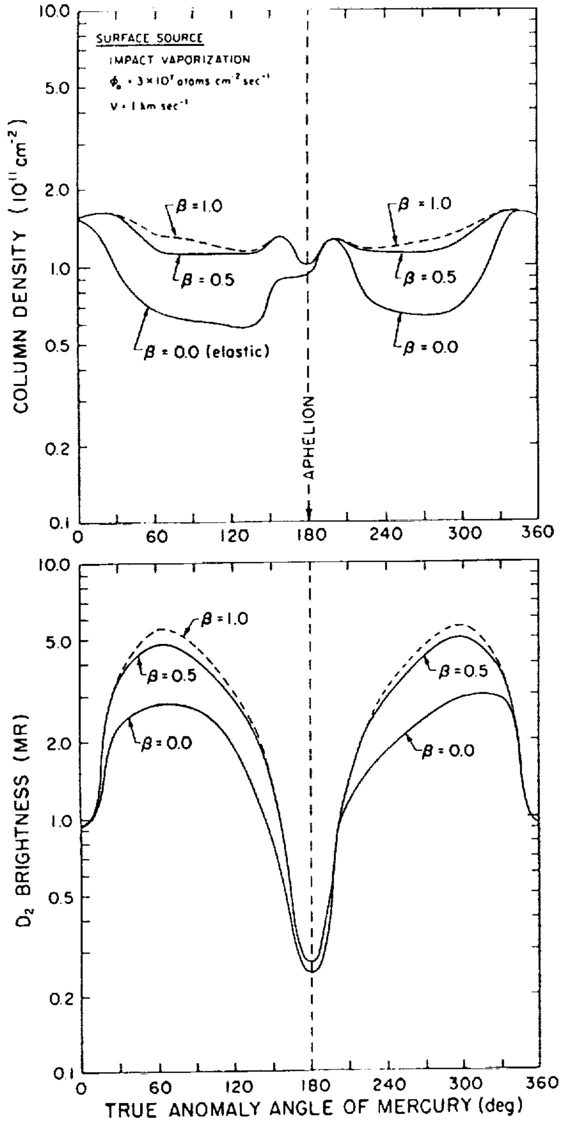

FIG. 16.—Model simulation for the sodium atmosphere from $\Phi = 60°$ to the terminator. The model simulation shows the dependence of the sodium column density and D_2 brightness on the true anomaly angle of Mercury for the impact vaporization source indicated (ϕ_0 is the atom surface flux at $f = 0°$) and the migration time and photoionization lifetime given in Fig. 12.

The column density and D_2 emission brightness in Figure 16 are determined for $\phi_0 = 3.0 \times 10^7$ atoms cm^{-2} s^{-1} in order to obtain the approximate range of the observed brightness values. In the upper portion of Figure 16 for $\beta = 0$, the column density has a maximum value at a true anomaly angle of ~350°, where the source is near its maximum and where the lateral transport is slow because the migration time (see Fig. 12) has a relative maximum. For $\beta = 0$, the column density has minimum values at true anomaly angles of ~130° and ~270°. These minima are caused by the combination of a symmetric decreasing gas source about aphelion and the rapid but asymmetric nature of the lateral transport rate which has its two relative maxima (i.e., the relative minima for the migration time) at two different true anomaly angles between perihelion and aphelion (see Fig. 12). For $\beta = 0.5$ and $\beta = 1.0$, the lateral transport rate is diminished, and the column density now has a minimum value at aphelion since the impact vaporization source decreases more steeply than a R^{-2} source and hence more than compensates for the increasing R^2 dependence of the residence time of a sodium atom because of the photoionization lifetime. For $\beta = 0.5$ and $\beta = 1.0$, the maximum column density occurs near perihelion where the source is a maximum (see Fig. 13). For both cases, the variation of the column density is a factor of ~1.6. The more nearly constant column density for $\beta = 0.5$ and $\beta = 1.0$ produces an enhancement in the D_2 emission brightness in comparison to the $\beta = 0$ case as can be seen in the lower portion of Figure 16. The D_2 brightness peaks at a true anomaly angle near 64° and 296° where the g-value is maximum (except for the peculiar elastic $\beta = 0$ case). The minimum D_2 brightness at aphelion is ~3.5 times smaller than at perihelion. This ratio is even larger than the ~2.3 ratio in Figure 15 because of the larger variation in the impact vaporization source (see Fig. 13).

4.2.5. *Sodium Column Density versus Solar Radiation Acceleration*

For sodium, the zenith (i.e., radial) column densities were deduced by Potter & Morgan (1987) from their observed D_1 and D_2 brightness data acquired using a north-south slit on the sunlit planet near (and parallel to) the terminator. Their deduced column densities, together with the times of the observations and the corresponding true anomaly angles of Mercury and solar radiation accelerations, are summarized in Table 3. Two important corrections to those values initially published by Potter & Morgan (1987) are included in Table 3. First, three improved column densities as recomputed by Potter (1988) are listed for the observations of 1986 February 22. Second, new values for the solar radiation acceleration expressed in units of surface gravity are listed since the original values published by Potter & Morgan (1987, in their Table II and used in their Fig. 1) were discovered to be incorrect because of a computing error (Potter 1989). For the 21 observations in Table 3 obtained with a north-south slit, the corrected sodium column density plot as a function of the solar radiation acceleration in units of surface gravity is given in Figure 17. The sodium column density is still anticorrelated with the solar radiation acceleration as initially reported by Potter & Morgan (1987). The anticorrelation is exhibited in Figure 17 by the straight-line least-squares fit to the 21 data points. The slope of the least-squares–fit straight line in Figure 17 has, however, a somewhat smaller negative value than that originally reported. Since the column density is known to be time variable, the least-squares–fit straight line in Figure 17 essentially represents the time-average trend for the column density viewed in the north-south slit. In addition to time variability, some scatter in the column density will also arise from the sensitive method of extracting the column density from the ratio of the D_2 to D_1 sodium emission brightnesses (measured simultaneously and with high signal-to-noise ratio but with no absolute calibration), where a small change (~5%–10%) in the ratio produces a factor of ~2 change in the column density (see Brown & Yung 1976). Based upon the heliocentric distance and radial motion of Mercury and the corresponding maximum value (0.5433) and minimum value (0.0336) of the solar radiation acceleration in units of surface gravity, the average column density as determined from the least-squares straight line in Figure 17 changes from a low of 1.35×10^{11} cm^{-2} to a high of 2.14×10^{11} cm^{-2} (i.e., a factor of 1.59).

It is interesting to ask how the sodium zenith column densities obtained from the observations of Potter & Morgan

TABLE 3

MERCURY ATMOSPHERE: SODIUM OBSERVATIONS OF POTTER & MORGAN (1987)

Civil Date	UT Time (h)	Julian Date	True Anomaly Angle	Column Density (10^{11} cm^{-2})	Solar Radiation Acceleration (cm s^{-2})	Solar Radiation Acceleration[a] (Surface Gravity)	Visible Terminator
1985 Jan 03	20.40	244,069.35	109°8	1.65 ± 0.41	149.22	0.4030	Morning
1985 Jan 04	16.80	070.20	113.0	1.65 ± 0.41	143.15	0.3866	Morning
1985 Jan 06	16.32	072.18	120.2	1.73 ± 0.42	130.65	0.3529	Morning
1985 May 11	17.76	197.24	230.0	1.93 ± 0.43	106.82	0.2885	Morning
1985 May 12	14.40	198.10	232.9	2.15 ± 0.41	116.44	0.3145	Morning
1985 May 13	14.64	199.11	236.3	1.69 ± 0.44	122.57	0.3311	Morning
1985 May 14	14.88	200.12	240.0	1.61 ± 0.42	129.01	0.3484	Morning
1985 May 15	14.16	201.09	243.2	2.24 ± 0.43	135.09	0.3649	Morning
1985 Jul 10	1.92	256.58	147.3	2.24 ± 0.49	62.428	0.1686	Evening
1985 Jul 10	18.48	257.27	149.4	1.85 ± 0.48	56.997	0.1539	Evening
1985 Jul 11	1.20	257.55	150.3	1.89 ± 0.48	56.773	0.1533	Evening
1985 Nov 16 (E-W)	20.40	386.35	281.7	0.98 ± 0.44	192.91	0.5210	Evening
1985 Nov 16	19.44	386.31	281.5	1.30 ± 0.42	192.65	0.5203	Evening
1986 Feb 17	18.72	479.28	307.1	1.49 ± 0.20	191.73	0.5179	Evening
1986 Feb 17	19.20	479.30	307.2	1.32 ± 0.20	188.08	0.5080	Evening
1986 Feb 17	19.92	479.33	307.4	1.34 ± 0.20	186.02	0.5024	Evening
1986 Feb 19	20.16	481.34	318.8	1.15 ± 0.20	156.25	0.4220	Evening
1986 Feb 20	16.80	482.20	323.8	1.44 ± 0.29	130.46	0.3524	Evening
1986 Feb 22	16.56	484.19	335.9	1.54 ± 0.50	71.387	0.1928	Evening
1986 Feb 22	17.28	484.22	336.1	1.58 ± 0.50	71.422	0.1929	Evening
1986 Feb 22	17.28	484.22	336.1	1.89 ± 0.50	71.422	0.1929	Evening
1986 May 05 (E-W)	13.44	556.06	254.9	1.27 ± 0.83	156.37	0.4224	Morning
1986 May 05	14.64	556.11	255.1	1.27 ± 0.83	156.60	0.4230	Morning

[a] Ratio of solar radiation acceleration to surface gravity (370.24 cm s^{-2}).

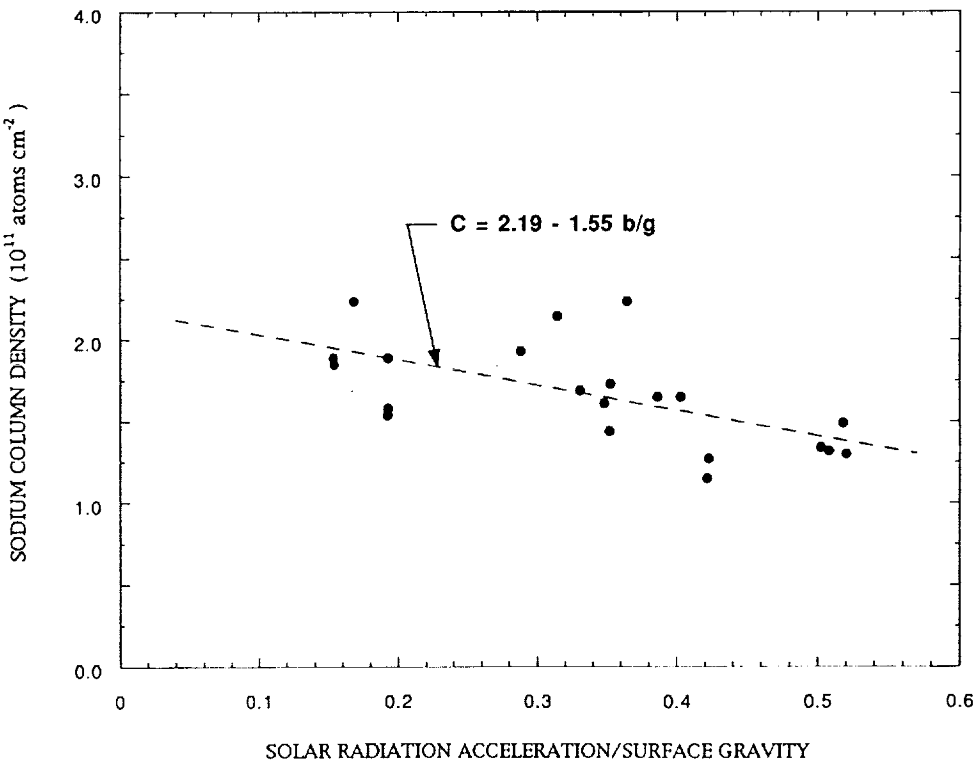

FIG. 17.—Observed variation of the sodium abundance in Mercury's atmosphere with solar radiation acceleration. The sodium column abundance for 21 slit-average brightness measurements of Potter & Morgan (1987) acquired with a north-south oriented slit is shown by the solid dots as a function of the radiation acceleration (in units of surface gravity) experienced by stationary sodium atoms in Mercury's atmosphere due to solar resonance scattering in the D-lines. The dashed line is a least-squares fit straight line to the measurements, where C is the column density, b is the solar radiation acceleration, and g is the acceleration of surface gravity.

(1987) compare with the model calculations in Figures 14–16. In making this comparison as a function of the true anomaly angle, two problems, however, arise. First, the number of data points is low since there are only 21 north-south slit-average brightness measurements for the whole 360° range. Second, for any small interval of the true anomaly angle, the variability of the data points is somewhat comparable to the maximum variation of the column density so that there is not a sufficient number of data points in the interval to obtain a good average value and to adequately differentiate different model calculations. In the absence of more data, however, a fourfold increase in the statistics is realized in Figure 17 by using the radiation acceleration as the independent variable instead of the true anomaly angle (see Fig. 5). In order to better isolate information that may be present in the fourth order degeneracy, however, the data points in Figure 17 are replotted in Figure 18, where they are divided into two sets of points: (1) 13 solid dots for Mercury with true anomaly angles centered about aphelion between 64° and 296° and (2) eight open dots for Mercury with true anomaly angles centered about perihelion between 296° and 64°. In Figure 18, each set of points is fitted separately by a least-squares straight line. Although the number of points in each data set is not as large as one would like, the column densities and the negative slope of the straight-line fit for the solid dots (i.e., where Mercury is more distant from the Sun) are larger than for the open dots (i.e., where Mercury is closer to the Sun). In the remaining discussion in this section, model calculations for the sodium column density are compared in Figures 19, 20, and 21 with the observational data in Figure 18 for various true anomaly dependencies of the source and for different values of the energy accommodation coefficient. In all cases, the sodium flux ϕ in the model is determined by normalizing the model calculated column density at a true anomaly angle of 64° to the least-squares straight-line fit in Figure 17. The true anomaly angle of Mercury is also given as a parameter along the model curves.

In Figure 19, model column densities for a constant source are compared to the observed column densities. For an energy accommodation coefficient of 0.0, 0.5, and 1.0, the values of the sodium flux are, respectively, 5.2×10^7 atoms cm^{-2} s^{-1}, 3.0×10^7 atoms cm^{-2} s^{-1}, and 2.6×10^7 atoms cm^{-2} s^{-1} as indicated. Two important results are immediately evident. First, atoms will certainly not bounce elastically on the surface because this condition produces a dynamic range for the column density that is much too large. This dynamic range is caused by the accumulated kinetic energy of the atoms as they are driven antisunward by the solar radiation acceleration and undergo either rapid lateral transport (if bound) or rapid escape from the planet. A significant surface energy accommodation coefficient is required to reduce the accumulated atom energy and hence reduce the large dynamic range of the model calculated column density to values that are even near the observed column density range. As the value of β increases, the dynamic range of the column density decreases, but even for the maximum value of $\beta = 1.0$, the model calculated variation is still too large. For the assumed constant source, this larger dynamic range indicates that the model calculated variation

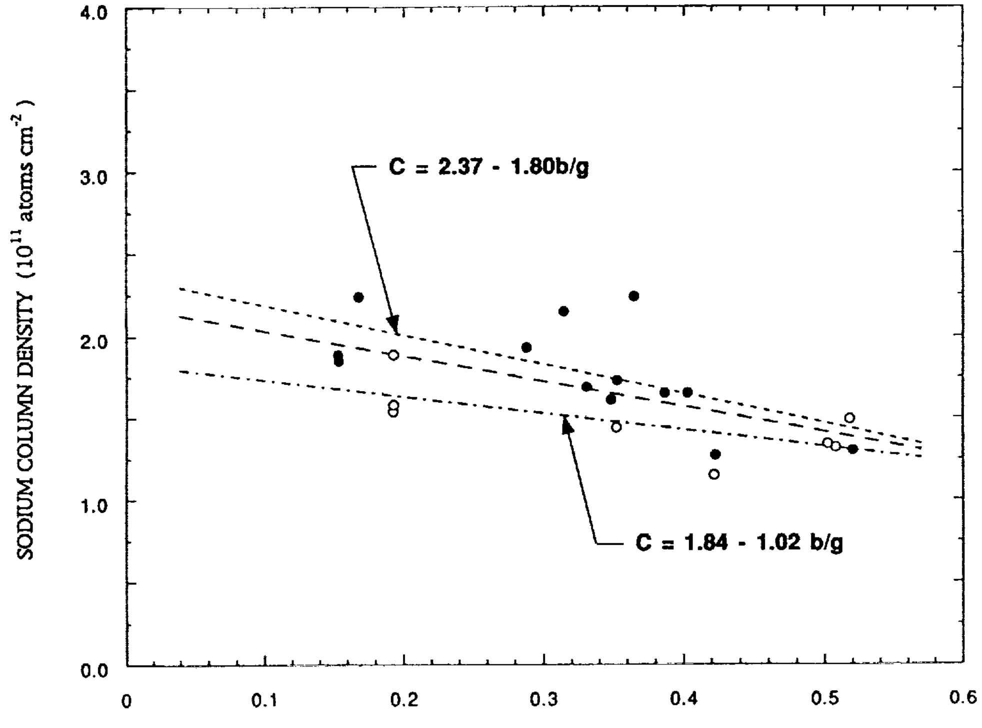

FIG. 18.—Observed variation of the sodium abundance in Mercury's atmosphere with solar radiation acceleration. The measurements in Fig. 17 have been subdivided into two sets of points: (1) the solid circles for true anomaly angles from 64° to 296° with the least-squares–fit straight line given by the shorter dashed line and (2) the open circles for true anomaly angles from 296° to 64° with the least-squares–fit straight line given by the dot-dashed line. For the least-squares–fit straight lines, C is the column density, b is the solar radiation acceleration, and g is the acceleration of surface gravity. The longer dashed line is the same least-squares fit to all of the data points given in Fig. 17.

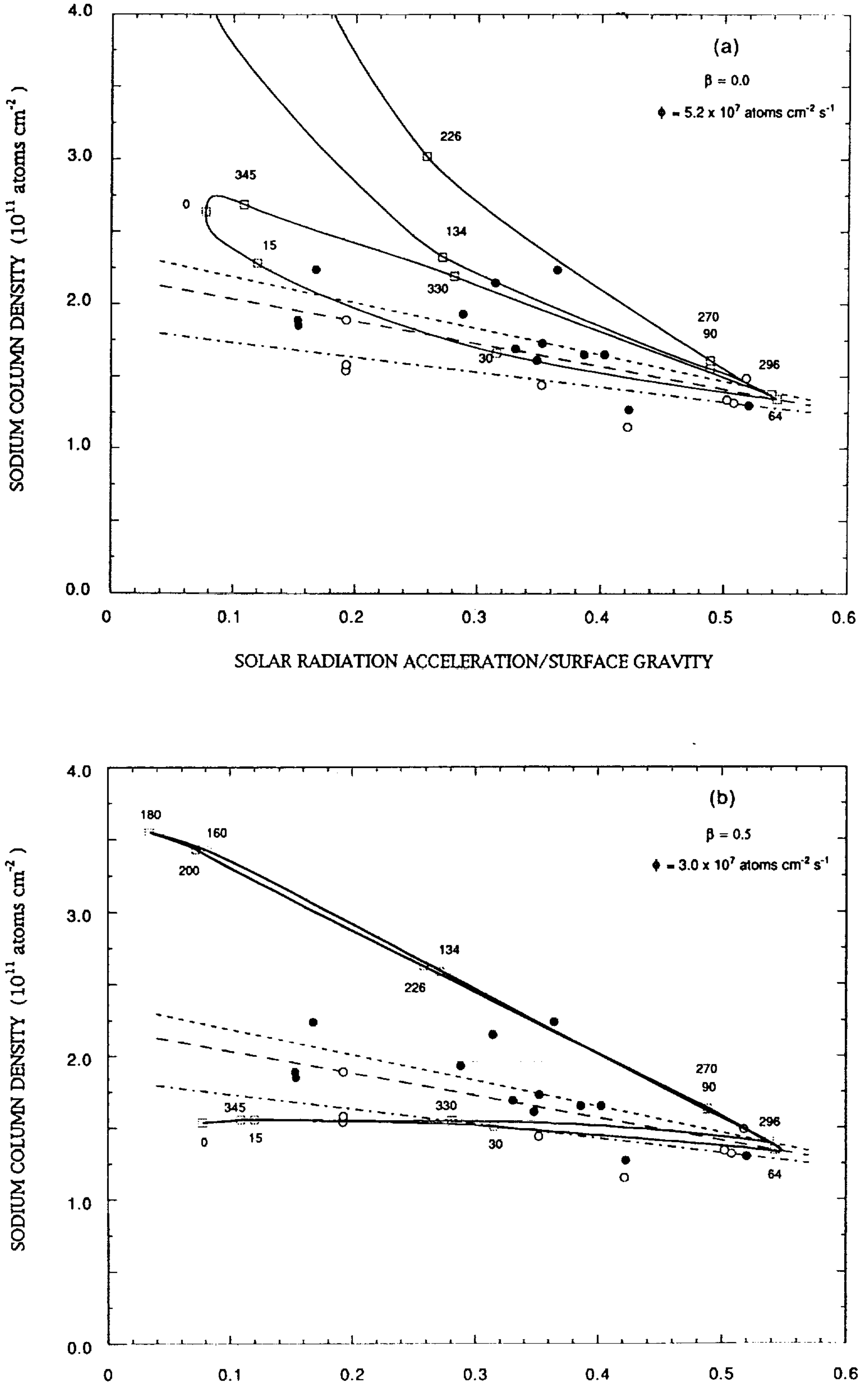

FIG. 19.—Model simulations for the sodium abundance variation with solar radiation acceleration. The model simulated variation of the sodium column density with the solar radiation acceleration (in units of surface gravity) is shown by the solid line for the indicated constant surface source flux (*a*) for $\beta = 0.0$, (*b*) for $\beta = 0.5$, and (*c*) for $\beta = 1.0$. The constant flux is determined by normalizing the model column density at a true anomaly angle of 64° to the least-squares straight-line fit in Fig. 17. True anomaly angles (in degrees) are indicated along the curves by the dashed squares.

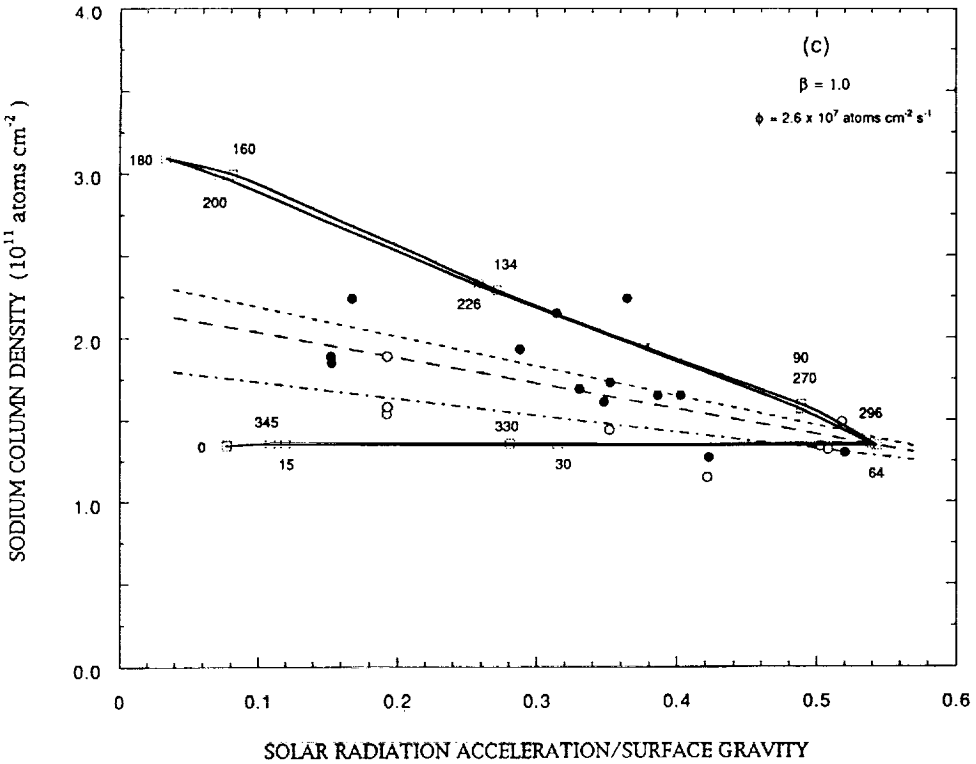

FIG. 19—*Continued*

produced by photoionization and transport is physically too large and that some decrease of the source with the true anomaly angle is required to rectify the situation. Second, even though the calculated dynamic range is too large, the general behavior of the calculated and observed column densities as a function of the solar radiation acceleration is similar. For true anomaly angles within ±64° of perihelion, both the calculated and observed column densities are lower than the calculated and observed column densities for true anomaly angles within ±116° of aphelion. In addition, for β as large as 0.5, the two calculated perihelion branches (i.e., $-64°$ to 0° and 0° to 64°) of the lower curve are essentially the same, and the two calculated aphelion branches (i.e., 64° to 180° and 180° to 296°) of the upper curve are essentially the same. The negative slope of both the upper curve for two aphelion branches and the lower curve for the two perihelion branches decreases as the value of β increases. For $\beta = 1$, the slope for the lower curve for the two perihelion branches is essentially zero, indicating that the rate of decrease in the column density because of the increasing transport loss to the night side has just matched the rate of increase in the column density because of the increasing photoionization lifetime. This matching of the two rates indicates that the value of β in the model should be somewhat less than 1.0 so that the transport loss will dominate the increased atom residence time provided by the lifetime and thus insures the nonzero negative slope (i.e., anticorrelation) of the lower curve for the two perihelion branches as required by the observations. The model results in Figure 19*b* are similar in nature to the sunlit planetary half-disk-averaged column abundance of sodium calculated for $\beta = 0.5$ by Ip (1990) but have a larger column density variation, as would be expected, since the partial spatial region of the disk sampled here is restricted nearer to the terminator (i.e., from $\Phi = 60°$ to 90°) where antisunward transport driven by solar radiation acceleration is more dominant.

In Figure 20, model column densities for an R^{-1} source (i.e., the next most weakly varying source in Fig. 13) are compared to the observed column densities for $\beta = 0.5$ and $\beta = 1.0$, where the values of the sodium flux ϕ_0 [i.e., $\phi = \phi_0(R_p/R)$] are, respectively, 3.3×10^7 atoms cm^{-2} s^{-1} and 2.9×10^7 atoms cm^{-2} s^{-1} as indicated. Similar to Figures 19*b* and 19*c*, column densities in the upper curve in Figures 20*a* and 20*b* are produced by the two aphelion branches (i.e., 64° to 180° and 180° to 296°), and those in the lower curve by the two perihelion branches (i.e., $-64°$ to 0° and 0° to 64°). In comparison to the least-squares straight-line fit for the observational data, the overall column density variation for the R^{-1} source in Figures 20*a* and 20*b*, although still slightly too large, is much better than for the constant source in Figures 19*b* and 19*c*. For the upper curve produced by the two aphelion branches, the negative slope is still too large for $\beta = 0.5$ in Figure 20*a* but matches the observation quite well for $\beta = 1.0$ in Figure 20*b*. For the lower curve produced by the two perihelion branches, the negative slope is in reasonably good agreement for $\beta = 0.5$ in Figure 20*a* but is too flat for $\beta = 1.0$ in Figure 20*b*. These comparisons suggest that a better match to the observational data will be obtained for a source which decreases more rapidly than R^{-1} and for a value of β near 0.5.

Model column densities for $\beta = 0.5$ are compared to the observed column densities for an $R^{-1.5}$ source [i.e., $\phi = \phi_0(R_p/R)^{1.5}$] in Figure 21*a*, for an R^{-2} source (i.e., the third source in Fig. 13) in Figure 21*b*, and for an impact vaporization source (i.e., the fourth source in Fig. 13) in Figure 21*c*, where the values of the sodium flux ϕ_0 are, respectively, 3.5×10^7 atoms cm^{-2} s^{-1}, 3.7×10^7 atoms cm^{-2} s^{-1}, and 3.5×10^7 atoms cm^{-2} s^{-1} as indicated. For the $R^{-1.5}$ source in Figure

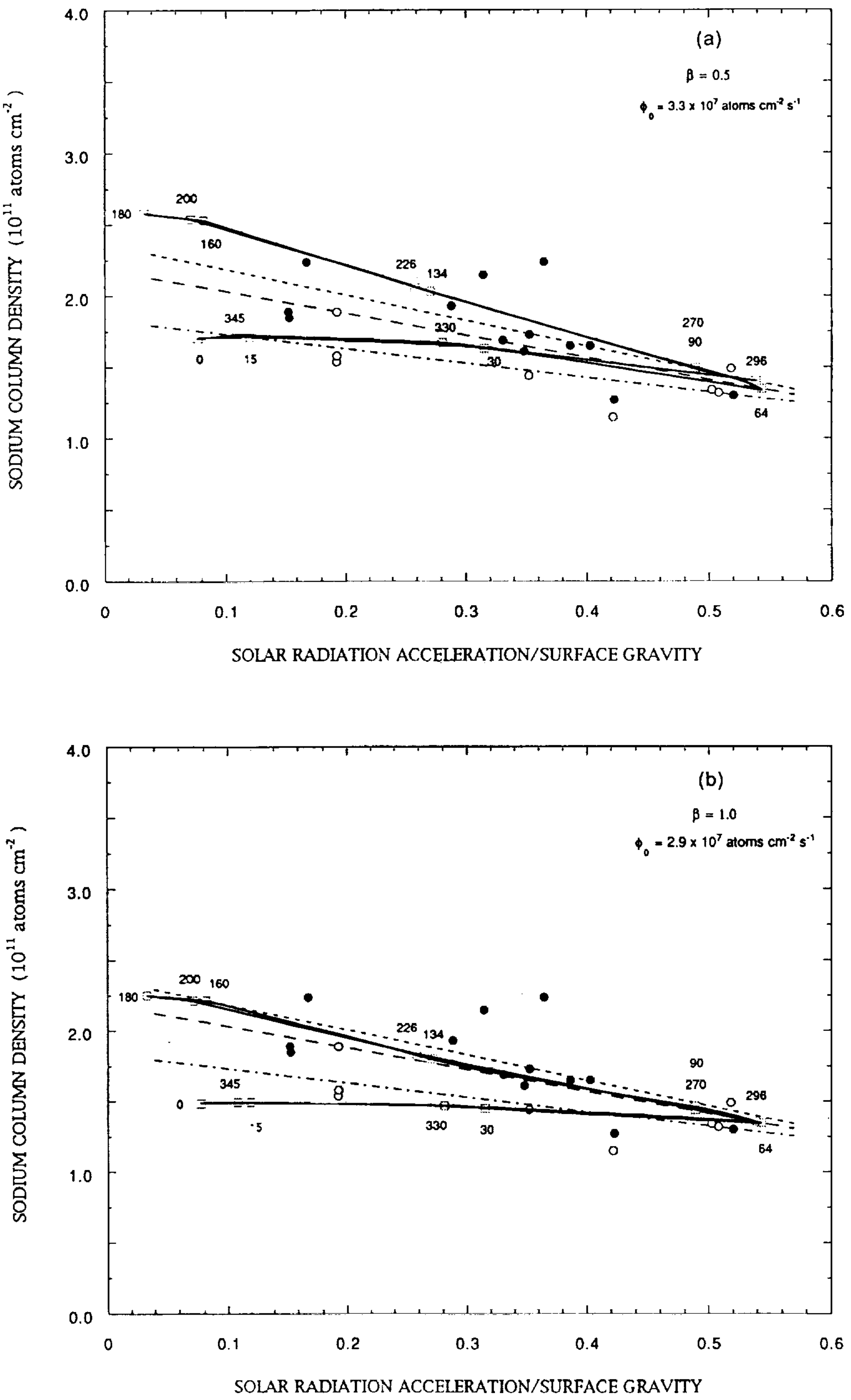

FIG. 20.—Model simulations for the sodium abundance variation with solar radiation acceleration. The model simulated variation of the sodium column density with the solar radiation acceleration (in units of surface gravity) is shown by the solid line for a surface source flux that varies as the inverse of the heliocentric distance (*a*) for $\beta = 0.5$ and (*b*) for $\beta = 1.0$. The absolute flux at zero true anomaly angle is the value ϕ_0 indicated. This flux is determined by normalizing the model column density at a true anomaly angle of 64° to the least-squares straight-line fit in Fig. 17. True anomaly angles (in degrees) are indicated along the model curves by the dashed squares.

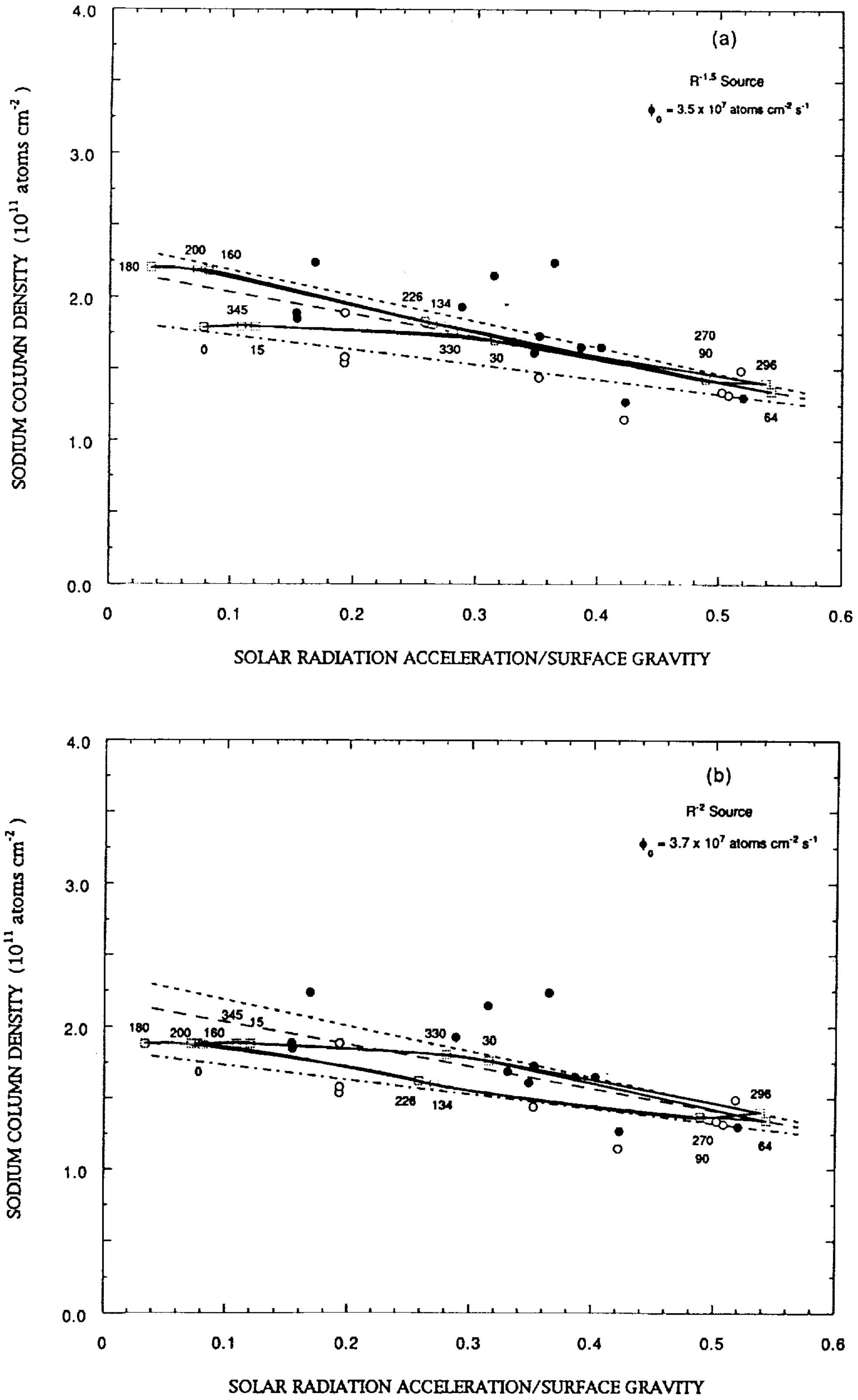

FIG. 21.—Model simulations for the sodium abundance variation with solar radiation acceleration. The model simulated variation of the sodium column density with solar radiation acceleration (in units of surface gravity) is shown by the solid line for $\beta = 0.5$ and for a surface source flux that (*a*) varies as the inverse 1.5 power of the heliocentric distance, (*b*) varies as the inverse square of the heliocentric distance, and (*c*) has the impact vaporization true anomaly angle dependence given in Fig. 13. The absolute flux at zero true anomaly angle is the value ϕ_0 indicated. This flux is determined by normalizing the model column density at a true anomaly angle of 64° to the least-squares straight-line fit in Fig. 17. True anomaly angles (in degrees) are indicated along the model curves by the dashed squares.

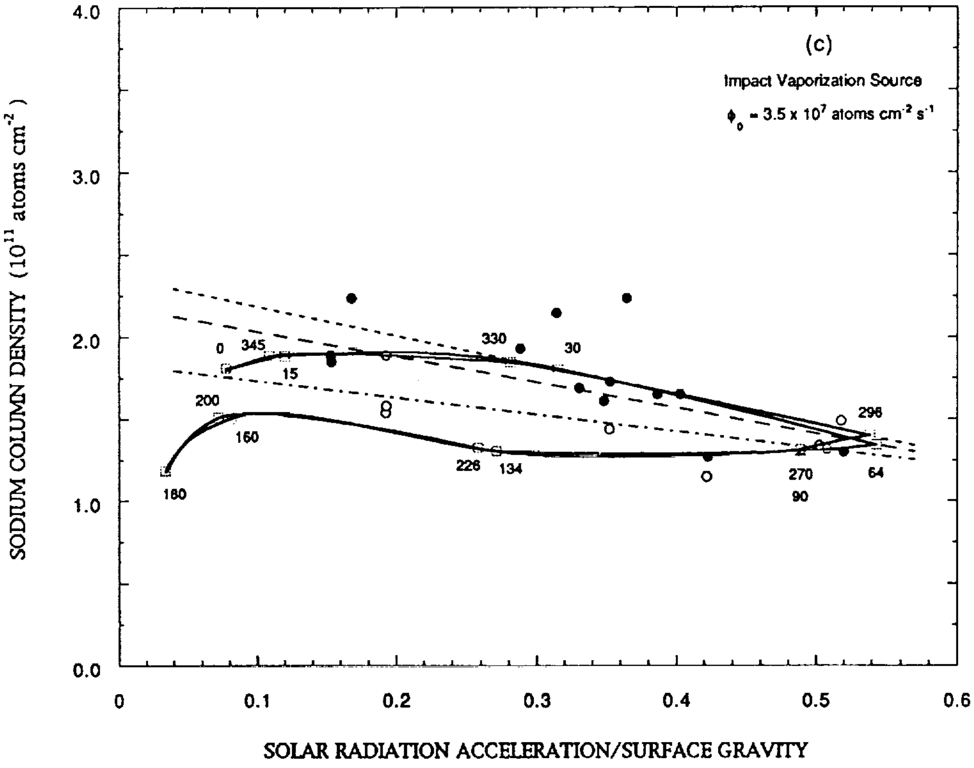

FIG. 21—*Continued*

21*a*, the upper curve is still produced by the two aphelion branches, and the lower curve is still produced by the two perihelion branches. These two curves, which provide a reasonable (but not perfect) fit to the data, lie between the two least-squares straight-line fits to the observational data and are essentially identical for values of the solar radiation acceleration in units of surface gravity between about 0.3 and 0.5. For the $R^{-1.5}$ source and $\beta = 1.0$, the negative slope of the two curves (not shown) is too small, with the upper curve for the two aphelion branches just above the lower least-squares straight-line fit to the observational data and the lower curve for the two perihelion branches mostly below the straight line. Exhibiting exactly the reverse behavior to the model results in Figures 19, 20, and 21*a* and also to the two least-squares straight-line fits to the observations, the column densities in the upper curve of Figures 21*b* and 21*c* are now produced by the two perihelion branches and those in the lower curve by the two aphelion branches. In Figure 21*b*, the separation of the column density in the upper and lower model curves is fairly small, and the overall fit to data set as a whole (*longer dashed line*) is fairly good if one ignores the separate and reverse oriented contributions from the perihelion and aphelion observed branches. The negative slope of the two curves in Figure 21*b* is the result of the velocity dependence of the solar radiation acceleration in the transport migration time, since if the transport process were ignored (i.e., an infinite migration time), the column density in Figure 21*b* would be constant. In Figure 21*c*, the separation of the column density in the upper and lower model curves is much larger, and the overall fit to the data set as a whole (*longer dashed line*) is not very good, even if one ignores the separate and reverse oriented contributions from the perihelion and aphelion observed branches. This mismatch indicates that the impact vaporization source has too large a variation with respect to the true anomaly angle to fit the observations.

The model-data comparisons in Figures 19, 20, and 21 with the five separate functional dependencies of the sources on the true anomaly angle allow a number of conclusions to be drawn and future activities to be identified. First, since the observed column density for sodium in Figure 18 is anticorrelated with the solar radiation acceleration for both the lower least-squares straight-line fit to the two perihelion branches and the upper least-squares straight-line fit to the two aphelion branches, it is clear that lateral transport of ambient atoms driven by solar radiation acceleration, not the photoionization lifetime, is the responsible agent in the anticorrelation observed by Potter & Morgan (1987). Over the appropriate true anomaly range, the observed average column density changes by a factor of ~1.4 for the lower least-squares straight-line fit to the two perihelion branches and by a factor of ~1.7 for the upper least-squares straight-line fit to the two aphelion branches. Second, in order to reduce the variation of the model calculated column densities as a function of the true anomaly angle to approximately these observed values, it is clear (1) that the energy accommodation coefficient for sodium atoms must be significant ($\beta \sim 0.5$, but not 1.0) so as to slow by the proper amount the transport rate driven by solar radiation acceleration and (2) that some decrease of the surface source flux with the true anomaly angle is required. For a single source, the best fit for the five sources considered is surprisingly obtained for a source with a heliocentric distance dependence of approximately $R^{-1.5}$ and a value of β near 0.5. For the more seemingly physically justifiable R^{-2} source, the model calculated slope and column density values compare well with the observations, but unfortunately the variation of the source with the true anomaly angle is sufficiently large to reverse the order of the model curves so that the two perihelion branches are now above the two aphelion branches (i.e., the reverse of the observational data). In order to isolate the true anomaly dependence of the source with more certainty, however, more observational data are clearly needed in order to obtain a better time-averaged column density in a given interval of the true anomaly angle and also over a wider range of the true anomaly angle.

4.3. *Spacetime Animations for Surface Point Sources*

Animations of the spacetime evolution of the sodium and potassium atmospheres produced by a point source on the sunlit surface have been calculated using the models described in § 3 and are presented in the accompanying videotape (ApJ, 441, Part 1, No. 2, Videotape, Segment 3). The animations provide a scientific visualization of the numerical spacetime-dependent Green's functions for the ensuing transport of the atoms above and along the planetary surface. The decay of the atom population due to photoionization is included and visually rendered by reducing the initial yellow brightness of atoms to darker shades which ultimately become brown. In all cases, the gas-surface sticking coefficient is assumed to be zero (i.e., no sticking to the surface) on the sunlit hemisphere, so that the natural time evolution of the dayside ambient atom atmosphere produced by the source atom atmosphere may be followed, and is assumed to be unity (i.e., complete sticking to the surface) on the nightside hemisphere. Once the point source on the sunlit surface is activated in the time-evolution model calculations, the atoms are ejected isotropically and at a constant rate from the point source and are shown for a sufficient time, so that the steady state spatial distribution for the ambient atom population is established. The three-dimensional animation is projected upon a two-dimensional viewer's plane. In all cases, the physical quantity for the atoms that is represented on the viewer's plane is the brightness of the brighter emission line for either sodium (5890 Å) or potassium (7665 Å), where both lines are excited by solar resonance scattering. Latitude and longitude lines on the planet spaced by 30° are shown in order to establish a spatial scale on the surface. For the purpose of identifying the sunlit hemisphere of the planet, a red dot is located at the subsolar point, and the terminator great circle is shown in red. The planet is opaque so that the atmosphere on the far side cannot be seen. All time evolving sequences are shown three times in succession to enhance comprehension. Four different model simulations, which are described separately below, are included on the videotape and illustrate the strong dependence of the ensuing point source atmosphere on the nature of the gas-surface interaction, the location of the point source on the surface, the location of the planet in its orbit, and the initial flux velocity distribution of the source atoms.

In model simulation 1, the spacetime evolution of the lateral transport of sodium gas ejected with an initial speed of 1 km s^{-1} from a point source located at the subsolar point on the planet is compared when the solar radiation acceleration is maximum ($f = 64°$) for two different gas-surface interaction scenarios. The two scenarios contrast the sodium in its lateral transport for the case of no surface thermal accommodation of the ambient atoms (i.e., $\beta = 0.0$, elastic bouncing on the surface) and 50% surface thermal accommodation per bounce (i.e., $\beta = 0.5$). For no thermal accommodation, the evolving ambient atom atmosphere rapidly migrates antisunward and escapes the planet. The presence of the atmosphere within the shadow region of the planet is (artifically) shown so as to illustrate the nature of the spacetime evolution of the escaping atoms in the coma. For 50% surface thermal accommodation, the ambient atom atmosphere does not escape but migrates antisunward along the surface much more slowly and is restricted spatially in its evolution to steady state to a region centered somewhat near the subsolar point. As noted in § 4.2, the case of no thermal accommodation of sodium atoms to the surface produced column density variations that were much larger than observed. In the remaining model simulations, a more appropriate surface thermal accommodation coefficient of $\beta = 0.5$ is therefore adopted.

In model simulation 2, the steady state spatial distributions for sodium gas ejected with an initial speed of 1 km s^{-1} from a point source located at the subsolar point and from a point source located 60° from the subsolar point on the planetary equator are compared when the solar radiation acceleration is maximum ($f = 64°$) and the surface thermal accommodation coefficient β is 0.5. The time evolution of the point source at the subsolar point was shown in model simulation 1. The steady state distribution is localized near the subsolar point source with its most extended (brown-colored) boundary still far from the terminator. In contrast, the steady state distribution originating from the point source located 60° from the subsolar point has a much smaller migration time (because of the larger component of the radiation acceleration parallel to the surface) and thus is able to reach and cross over the terminator before it is completely ionized. This loss of gas by lateral transport to the dark hemisphere lowers the column density of the sunlit atmosphere for $60° \leq \Phi \leq 90°$, which is the portion of the atmosphere observed in the north-south slit of Potter & Morgan (1987), and thus illustrates a mechanism to explain their observed anticorrelation of the sodium column density with the solar radiation acceleration.

In model simulation 3, the spacetime evolution of the lateral transport of potassium gas ejected with an initial speed of 1 km s^{-1} from a point source located 60° from the subsolar point on the planetary equator is compared for Mercury at two different orbital locations for a thermal accommodation coefficient of $\beta = 0.5$. Mercury's locations are chosen at a true anomaly angle $f = 47°$, where the solar radiation acceleration is maximum, and at a true anomaly angle $f = 0°$ (i.e., perihelion), where it is weak. For maximum solar radiation acceleration, the antisunward migration of potassium atoms is very rapid, so that a significant fraction of the atoms is able to cross the terminator and become part of the dark-side atmosphere before they are photoionized. The solar radiation acceleration is indeed so strong that many of the atoms cross the terminator at significant altitudes so as to stay illuminated beyond the terminator boundary, and some of these potassium atoms even escape the planet. The presence of the escaping potassium atoms within the shadow region of the planet is (artificially) shown so as to illustrate their spacetime evolution. For weak solar radiation acceleration, the antisunward migration of potassium atoms along the surface is much slower, so that the atoms are unable to cross the terminator before they are photoionized. As Mercury moves on its orbit about the Sun, the varying solar radiation acceleration will cause the lateral transport rate to change and will likely modulate the sunlit column density of the potassium atmosphere even more strongly than that observed for the sodium atmosphere when a lower energy accommodation coefficient for potassium is adopted.

In model simulation 4, the spacetime evolution of the sodium atoms produced by a meteorite impact vaporization event at a point source located 60° from the subsolar point on the planetary equator is shown for maximum solar radiation acceleration conditions ($f = 64°$) and for a thermal accommodation coefficient of $\beta = 0.5$. The point source is assumed to have a Maxwell Boltzmann speed distribution with a gas temperature of 4000 K, which is an intermediate temperature for such an impact event. Since the initial velocity distribution contains speed components that are both ballistic and escape in nature, both a large escaping coma and an evolving ambient atom atmosphere will be produced by the source atoms. When the atmosphere and escaping coma are within the shadow region of the planet, the sodium is not artificially illuminated in the animation so as to illustrate more realistically the visual spacetime evolution of the D_2 emission brightness of sodium atoms in the circumplanetary environment. The three-dimensional structure of the steady state sodium brightness distribution is also illustrated more clearly after its time evolution is completed by rotation of the planet relative to the viewer's plane.

5. SUMMARY AND CONCLUSIONS

A brief description of observations for gas species in Mercury's exospheric atmosphere was given. A theoretical overview for the nature of exospheric atmospheres was then presented. The interplay of the source, sinks, gas-surface interactions, and transport dynamics in determining the atmospheric structure was discussed in general and assessed specifically for the sodium and potassium atmospheres of Mercury. The large eccentricity (0.2056) of its planetary orbit about the Sun causes a variation in the subsolar temperature (575–708 K) by a factor 1.23, a variation in the dominant photoionization lifetime for sodium (1.4–3.3 hr) and potassium (0.97–2.2 hr) by a factor of 2.30 and a variation in solar radiation accelerations for sodium and potassium by a factor of ~ 16 and 12, respectively. The maximum values of the solar radiation acceleration are very large, having a value of ~ 200 cm s^{-2} (i.e., $\sim 54\%$ of surface gravity) at true anomaly angles of $\pm 64°$ for sodium and with a maximum value of ~ 293 cm s^{-2} (i.e., $\sim 79\%$ of surface gravity) at true anomaly angles of $\pm 47°$ for potassium. Since the sunlit surface is hot, gas-surface interactions favor thermal accommodation of the atoms upon encountering the surface. With a velocity for thermal accommodation for sodium (~ 0.64–0.72 km s^{-1}) and potassium (~ 0.49–0.55 km s^{-1}) atoms that is small compared to the planetary gravitational escape speed (4.25 km s^{-1}), most initial source atoms will, upon encountering the surface, likely rebound and give rise to a thermalized ambient atom atmosphere. This ambient atom atmosphere will migrate on the surface until ionized or until lost to the nightside atmosphere. Of particular importance in this migration process is the competition between the short photoionization lifetimes for sodium and potassium and the rapid antisunward transport of ambient atoms produced by the large solar radiation accelerations.

Models for the sodium and potassium atmospheres were developed in order to investigate the relative importance (and time variability) of the orbital dynamic timescales and rapid photoionization lifetimes for these atoms in determining the nature of their bound and escaping atmospheres. The models were first applied to study the spacetime nature of the source atom atmosphere, which forms an extended coma from its escaping component and a spatially distributed surface source for the ambient atom atmosphere from its ballistic component. For the maximum values of solar radiation acceleration, source atoms for sodium begin to escape at speeds of ~ 2.0 km s^{-1}, while source atoms for potassium begin to escape at speeds of ~ 1.6 km s^{-1}. These speeds are well below the two-body gravitational escape speed of 4.25 km s^{-1}. For a given flux velocity distribution for the source atoms, the number of source atoms that populate escape orbits and the number that populate ballistic orbits are then very dependent on Mercury's position in its orbit. It then follows that the spacetime nature of the escaping gas comae, the spacetime nature of the surface distribution of the nonescaping source atoms which supply the initial conditions for formation of the ambient atom atmospheres, and the spacetime nature of the spatial distribution of the heavy-ion sources produced within the planetary magnetosphere upon ionization of the source and ambient atoms will all be strongly dependent on the orbital location of Mercury.

Modeling studies for the sodium ambient atom atmosphere were undertaken next. Observations by Potter & Morgan (1987) for the high-resolution spectrum of the D_2 emission line (5890 Å) implied that a significant fraction of the atmosphere is likely to be nearly thermal and hence likely dominated by an ambient atom population. These sodium observations, with improvements and corrections noted earlier, showed that the sodium column density is anticorrelated with the large solar radiation acceleration experienced by these atoms. The ability of an antisunward lateral transport driven by this radiation acceleration to compete with the short sodium photoionization lifetime was investigated to see if it provided a mechanism to explain the observations. This was accomplished by calculating an average migration time to cross the terminator for an ensemble of sodium atoms originating from a point source positioned at different locations on the sunlit surface. For a significant portion of Mercury's orbit about the Sun, it was shown that for likely surface accommodation coefficient of ~ 0.5 to 1.0, the migration times for sodium are reduced by a factor of ~ 20 to 50 below the values obtained by neglecting radiation acceleration and are competitive with the photoionization lifetime for those spatial regions of the planetary surface viewed through the observing slit of Potter & Morgan (1987), which were typically within $\sim 30°$ of the terminator. Thus, lateral transport is an important factor in modulating the observed column density of the atmosphere. A similar situation will occur for potassium, which has an even larger solar radiation acceleration and a shorter photoionization lifetime than sodium.

Modeling studies based upon the migration times for the sodium ambient atom atmosphere were then undertaken to calculate the dependence of the column density and D_2 brightness on the true anomaly angle of Mercury and on various sources. For a source rate that is constant, varying as the inverse square of the heliocentric distance, and varying appropriately for micrometeoroid impact vaporization, the calculated column density and D_2 brightness have significantly different behaviors with the true anomaly angle as shown, respectively, in Figures 14, 15, and 16. To obtain column densities of ~ 1–2×10^{11} cm^{-2} and D_2 brightnesses of a few megarayleighs, similar to observed values, surface fluxes for the source atom in the range ~ 2–5×10^7 cm^{-2} s^{-1}, specified for Mercury at perihelion, were required on the sunlit hemisphere. The model calculated column densities as a function of the solar radiation acceleration normalized by the acceleration of surface gravity were also compared for different sources in Figures 19, 20, and 21 with the observations of Potter & Morgan (1987), which showed them to be anticorrelated. From these comparisons, three conclusions emerge. First, lateral transport driven by the solar radiation acceleration is responsible for the anticorrelated nature of the column density. Second, the surface energy accommodation coefficient must be significant ($\beta \sim 0.5$, but not as large as 1.0) in order to reduce the unaccommodated ($\beta = 0.0$) dynamic range of the calculated column density driven by the solar radiation acceleration (factor of ~4.4) to a range that is consistent with the observed variation of the average column density (factor of 1.6 to 2). Third, some decrease in the source rate for the source atom atmosphere as the true anomaly angle moves from the perihelion position to the aphelion position (i.e., in either branch, 0 to ±180) is also required in order to provide a better fit of the model and observed column density. The best fits are obtained for a source rate varying as the inverse 1.5 to 2.0 power of the heliocentric distance, but more data are required to refine the dependence of the source rate. Analysis of a sufficiently large observational data set for the variation of the time-averaged background column density, indeed appears to be a way to identify the source mechanism uniquely. Reduction of available one-dimensional and whole-planet observational data for sodium (Killen et al. 1990; Potter & Morgan 1990; Morgan & Potter 1992), which have been acquired more recently than the slit-average data contained in Potter & Morgan (1987), will therefore be particularly valuable in expanding this data set for future investigations. Finally, model calculations were presented on a videotape format to illustrate and to contrast the spacetime evolution of the sodium and potassium atmospheres produced by a point source on the sunlit surface and to provide scientific visualization animations of the numerical spacetime Green's function for the transport of atoms above and along the planetary surface.

We are grateful to M. R. Combi for early computational support in the development of the numerical model for Mercury's atmosphere and also to R. C. Woodward for development of scientific visualization software for rendering the animation sequences for Mercury's sodium and potassium atmospheres presented on the videotape. The determination of the potassium solar Fraunhofer features above Earth's atmosphere from ground-based data by R. L. Kurucz and the determination of the impact vaporization source rate for Mercury as a function of its true anomaly angle by T. H. Morgan are also gratefully acknowledged. This research was supported by the Planetary Astronomy Program of the National Science Foundation under grant AST-8614298 and by the Planetary Atmospheres Program of the National Aeronautical and Space Administration under contract NASW-4576.

REFERENCES

Broadfoot, A. L., Kumar, S., Belton, M. J. S., & McElroy, M. B 1974, Science, 185, 166
Broadfoot, A. L., Shemansky, D. E., & Kumar, S. 1976, Geophys. Res. Lett., 3, 577
Brown, R. A., & Yung, Y. L. 1976, in Jupiter: Studies of the Interior, Atmosphere, Magnetosphere, and Satellites, ed. T. Gehrels (Tucson: Univ. Arizona Press), 1102
Cheng, A. F., Johnson, R. E., Krimigis, S. M., & Lanzerotti, L. J. 1987, Icarus, 71, 430
Goldstein, B. E., Suess, S. T., & Walker, R. J. 1981, J. Geophys. Res., 86, 5485
Hunten, D. M., Morgan, T. M., & Shemansky, D. E. 1988, in Mercury, ed. F. Vilas, C. Chapman, & M. Matthews (Tucson: Univ. of Arizona Press), 562
Ip, W.-H. 1986, Geophys. Res. Lett., 13, 423
———. 1987, Icarus, 71, 441
———. 1990, ApJ, 356, 675
———. 1993, ApJ, 418, 451
Killen, R. M. 1989, Geophys. Res. Lett., 16, 171
Killen, R. M., & Morgan, T. H. 1993, Icarus, 101, 293
Killen, R. M., Potter, A. E., & Morgan, T. H. 1990, Icarus, 85, 145
———. 1991, Science, 252, 974
Kumar, S. 1976, Icarus, 28, 579
Kurucz, R. L. 1982, private communication
McGrath, M., Johnson, R. E., & Lanzerotti, L. J. 1986, Nature, 323, 694
Morgan, T. H. 1989, private communication
Morgan, T. H., & Potter, A. E. 1992, BAAS, 24, 957
Morgan, T. H., Zook, H. A., & Potter, A. E. 1988, Icarus, 75, 156
———. 1989, Proc. Lunar Planet. Sci. Conf., 19, 297
Ness, N. F., Behannon, K. W., Lepping, R. P., Whang, Y. C., & Schatten, K. H. 1974, Science, 185, 151
Potter, A. E. 1988, private communication
———. 1989, private communication
———. 1993, in Workshop on Sodium Atmospheres, Exospheres, and Coronae in the Solar System (San Juan Capistrano), 25
Potter, A. E., & Morgan, T. H. 1985, Science, 229, 651
———. 1986, Icarus, 67, 336
———. 1987, Icarus, 71, 472
———. 1990, Science, 284, 835
Shemansky, D. E. 1993, in Workshop on Sodium Atmospheres, Exospheres, and Coronae in the Solar System (San Juan Capistrano), 28
Shemansky, D. E., & Broadfoot, A. L. 1977, Rev. Geophys. and Space Phys., 15, 491
Shemansky, D. E., & Morgan, T. H. 1991, Geophys. Res. Lett., 18, 1659
Smyth, W. H. 1986a, Nature, 323, 696
———. 1986b, in paper presented at Mercury Conference (Tucson)
———. 1989, BAAS, 21, 974
Smyth, W. H., & Marconi, M. L. 1995, ApJ, in press
Sprague, A. L. 1990, Icarus, 84, 93
———. 1992, J. Geophys. Res., 97, 18257
Sprague, A. L., Kozlowski, R. W. H., & Hunten, D. M. 1990, Science, 249, 1140
Tyler, A. L., Kozlowski, R. W. H., & Hunten, D. M. 1988, Geophys. Res. Lett., 15, 1141

APPENDIX B

Theoretical Overview and Modeling of the Sodium and Potassium Atmospheres of the Moon

THE ASTROPHYSICAL JOURNAL, 443:371-392, 1995 April 10

THEORETICAL OVERVIEW AND MODELING OF THE SODIUM AND POTASSIUM ATMOSPHERES OF THE MOON

WILLIAM H. SMYTH AND M. L. MARCONI
Atmospheric and Environmental Research, Inc., 840 Memorial Drive, Cambridge, MA 02139
Received 1994 March 29; accepted 1994 October 21

ABSTRACT

A general theoretical overview for the sources, sinks, gas-surface interactions, and transport dynamics of sodium and potassium in the exospheric atmosphere of the Moon is given. These four factors, which control the spatial distribution of these two alkali-group gases about the Moon, are incorporated in numerical models. The spatial nature and relative importance of the initial source atom atmosphere (which must be nonthermal to explain observational data) and the ambient (ballistic hopping) atom atmosphere are examined. The transport dynamics, atmospheric structure, and lunar escape of the nonthermal source atoms are time variable with season of the year and lunar phase because of their dependence on the radiation acceleration experienced by sodium and potassium atoms as they resonantly scatter solar photons. The dynamic transport time of fully thermally accommodated ambient atoms along the surface because of solar radiation acceleration (only several percent of surface gravity) is larger than the photoionization lifetimes and hence unimportant in determining the local density, although for potassium the situation is borderline. The sodium model was applied to analyze sodium observations of the sunward ($D_1 + D_2$) brightness profiles acquired near last quarter by Potter & Morgan (1988b), extending from the surface to an altitude of 1200 km, and near first quarter by Mendillo, Baumgardner, & Flynn (1991), extending in altitude from ~1430 to ~7000 km. The observations at larger altitudes could be fitted only for source atoms having a velocity distribution with a tail that is mildly nonthermal (like an ~1000 K Maxwell-Boltzmann distribution). For both the lower and higher altitude observations, a number of equally good fits were achieved for differing amounts of ambient atom atmosphere as determined by different combinations of (1) the shape of the velocity distribution for the lower speed source atoms and (2) the gas-surface sticking and thermal accommodation conditions for the ambient atoms. For cases considered here, the sodium flux for source atoms ranged for the Mendillo et al. (1991) observations from 3.5×10^5 atoms $\mathrm{cm}^{-2}\ \mathrm{s}^{-1}$ for a dominant ambient atom atmosphere near the surface to 2.1×10^6 atoms $\mathrm{cm}^{-2}\ \mathrm{s}^{-1}$ for no ambient atom atmosphere, while the flux values for the observations of Potter & Morgan (1988b) were ~40% lower. Solar wind sputtering appears to be a viable source atom mechanism for the sodium observations with photon-stimulated desorption also possible but highly uncertain, although micrometeoroid impact vaporization appears to have a source that is too small and too hot, with likely an incorrect angular distribution about the Moon.

Subject headings: atmospheric effects — Moon

1. INTRODUCTION

Knowledge of the atmosphere of the Moon prior to 1988 was acquired from the *Apollo 14*, *15*, *16*, and *17* missions. Surface measurements from the cold cathode gauges on *Apollo 14* and *15* provided an upper limit on the exospheric number density of the lunar atmosphere of about 10^7 cm^{-3} in the daytime and 2×10^5 cm^{-3} at night (Johnson, Carroll, & Evans 1972), but concerns regarding the outgassing of the spacecraft provided questions as to what fraction of this upper limit is native to the Moon. For *Apollo 15* and *16*, measurements by the Lunar Orbiter Mass Spectrometer (Hodges, Hoffman, & Evans 1972) provided no detection of native gases, but the orbiting Alpha Particle Spectrometer detection of ^{210}Po and more marginal detection of ^{222}Rn (Bjorkholm, Golub, & Gorenstein 1973; Gorenstein, Golub, & Bjorkholm 1974a, b; Gorenstein & Bjorkholm 1977) provided evidence for small amounts of radon. The ultraviolet spectrometer onboard the *Apollo 17* command and service module provided only upper limits (Fastie et al. 1973) for H, O, N, C, Kr, Xe, H_2, and CO, which have been recently updated (including an upper limit for S) by Feldman & Morrison (1991). For the lunar surface spectrometer on *Apollo 17*, positive identifications and measurements were obtained for He and Ar by Hoffman, Hodges, & Evans (1973; also Hodges 1977, 1978, 1985) but were limited to the night side because of dayside outgassing and instrument considerations.

In 1988, the discovery of ~3.8 kR of sodium emisson (5890 Å) and ~1.8 kR of potassium emission (7699 Å) above the limb in the sunlit atmosphere of the Moon (Potter & Morgan 1988a) and the independent and nearly simultaneous confirmation of sodium (Tyler, Kozlowski, & Hunten 1988) initiated a new era for remote study of the lunar atmosphere. Because of the close proximity of the Moon to Earth and its very bright surface-reflected sunlight, one-dimensional slits located above the sunlit limb have been used to acquire vertical brightness profiles. Early observations showed, surprisingly, that the sodium atmosphere extended to at least a 1200 km altitude (Potter & Morgan 1988b), with a more recent observation (Potter & Morgan 1991) extending the altitude to 1500 km, indicating that the surface source velocity distribution for the atmosphere is basically nonthermal in character. A number of additional observations have been acquired for sodium (Sprague et al. 1992) for various altitudes up to ~610 km. Two additional observations have also been obtained for potassium

(Kozlowski, Sprague, & Hunten 1990; Sprague et al. 1992) for altitudes up to 190 km. Partial images and one composite image of the sodium have been more recently obtained (Mendillo, Baumgardner, & Flynn 1991; Flynn & Mendillo 1993) using a circular aperture placed well above the limb or a coronagraph mask technique and show sodium present to sunward distances of at least ~5 lunar radii (~9000 km) and to antisunward distances in an escaping coma of ~15–20 lunar radii.

The analyses of these sodium and potassium observations for the Moon to date are summarized in Table 1 and indicate that the atmosphere is still exospheric in nature. The analyses are divided chronologically into three different approaches that have been progressively implemented. The first approach uses a one-temperature (later, a two-temperature with cold and hot components) barometric description with a constant scale height to fit the vertical profiles and extract a scale height and temperature from the fit (see Table 1). Realizing that the constant scale height approximation was not an appropriate method for such an extended atmosphere, the second approach used the spherically symmetric description of Chamberlain (1963) for the density of an exosphere. This calculation of the column density and the fit to the vertical brightness profiles is based upon a Maxwell-Boltzmann velocity distribution. While this method properly includes the variation of gravity with altitude, it does not include the effects on the sodium and potassium three-dimensional density distributions of (1) a finite photoionization lifetime, (2) solar radiation acceleration, (3) non–Maxwell-Boltzmann source velocity distributions, (4) spatially nonuniform exobase (i.e., here surface) source distributions, and (5) complex gas-surface interactions. The third approach in Table 1, which is considered in this paper, is to use a Monte Carlo dynamic model for the atmosphere (Ip 1991; Smyth & Marconi 1993). This approach is numerical in nature and may readily include all of the above mentioned effects excluded by the Chamberlain model.

Early fits of the observed profiles using the first approach were strongly dependent on the maximum slit tangent altitude sampled by the observation, with longer slits yielding larger scale heights and higher temperatures. More recent fits using the second method likely include this same effect but also include the additional geometrical problem of using a spherically symmetrical density description to extract a scale height and temperature from a density distribution that is at best azimuthally symmetric about the Sun-Moon line (e.g., see the very recent observations of Flynn & Mendillo 1993; Potter & Morgan 1994). This latter problem may be particularly significant when the line of sight at the base of the slit (i.e., all slit observations in Table 1 are taken with the slit in the luminance equator plane) is tangent to the Moon's surface at a point on the equator between the subsolar point and the terminator which has a significant departure angle from the subsolar point (i.e., for the larger local solar zenith angle observations in Table 1). This geometry is the case for the analysis presented by Sprague et al. (1992), where they deduce an increasing temperature with an increasing local solar zenith angle using the

TABLE 1

ANALYSIS CHRONOLOGY OF EMISSION DATA VERTICAL PROFILES FOR THE LUNAR SODIUM AND POTASSIUM ATMOSPHERES (LUMINANCE EQUATOR OBSERVATIONS)

Date of Observation	Species	Surface Density (cm^{-3})	Scale Height[a] (km)	Temperature (K)	Maximum Slit Tangent Attitude (km)	Local Solar Zenith Angle	Time Since New Moon (day)	Reference
1. Constant Scale Height Approach:								
1988 Jan 12	K	15 ± 3	90 ± 20	690	40	18°	22.8	1
1988 Jan 13	Na	67 ± 12	120 ± 42	540	40	29	23.7	1
1988 Jun 7.........	Na	57 ± 20	79 ± 8	354	100	3		2
1988 Oct 2, 3......	Na	... 35(c), 2(h)	400–600 120(c), 500(h)	1800–2700 540(c), 2240(h)	1200	4, 8	21.2, 22.2	3
1989 Apr 29.......	K	9.5 ± 1 9.6(c), 1.1(h)	80 52(c), 329(h)	600 395(c), 2500(h)	106	7		4
2. Chamberlain Model Approach:								
1988 May 28	Na	29	260	1150	400	61	12.3	5
1988 Oct 2, 3......	Na	44	260	1150	1200	4, 8	21.2, 22.2	5
1989 Feb 22	Na	46	200	950	1500	18	16.0	5
1988 May 24	Na	...	70	385	100	0		6
1988 Jun 7.........	Na	34	106	476	100	3		6
1990 Aug 29.......	Na	26	270	1210	520	9		6
1990 Oct 12	Na	17	379	1699	610	16		6
1990 Oct 13	Na	20	429	1924	190	29		6
1990 Oct 14	Na	16	485	2175	190	41		6
1991 Jul 19	Na	...	287	1287	360	6		6
1989 Apr 29	K	10	80	610	106	7		6
1990 Jul 18	K	9	136	1033	190	41		6
3. Dynamic Model Approach (Monte Carlo):								
1988 Oct 2, 3......	Na[b]	54	223	1000–1200	1200	4, 8	21.2, 22.2	This paper
1991 Feb 20	Na[c]	90	223	1000–1200	~7000[c]	24	5	This paper

[a] Scale height based on gravity at surface.

[b] Data from Potter & Morgan 1988b.

[c] Data from Mendillo et al. 1991; minimum tangent altitude of ~1430 km.

REFERENCES.—(1) Potter & Morgan 1988a; (2) Tyler et al. 1988; (3) Potter & Morgan 1988b; (4) Kozlowski et al. 1990; (5) Potter & Morgan 1991; (6) Sprague et al. 1992.

second approach. This geometrical problem, however, draws into question whether this correlation is true because of a higher temperature (the basis for the hypothesis of a two-component source mechanism in their paper) or merely because an asymmetrical density distribution has been improperly fitted by using a model for a spherically symmetrical density distribution. Monte Carlo model calculations in this paper for two observations (see Table 1) that have widely differing local solar zenith angle (i.e., 4° and 24°) provide one counterexample to the correlation noted by Sprague et al. (1992). Monte Carlo models, therefore, are clearly required for the analysis of these data and the new observational data that will be forthcoming.

In this paper, a theoretical overview is first presented in § 2 to depict the character and to evaluate the relative importance of various physical processes in shaping the sodium and potassium atmospheres of the Moon. This detailed knowledge is then incorporated into models for the sodium and potassium atmospheres in § 3. In § 4, the sodium model is applied to select observations of the sodium atmosphere. The analysis is discussed in § 5. Finally, a summary with concluding comments is given in § 6.

2. THEORETICAL OVERVIEW

2.1. *Introduction*

Since the atmosphere of the Moon is essentially exospheric in nature, gas-phase collisions are negligible. The Moon therefore has multi-atmospheres, with each separate atmosphere forming independently and hence each having the capacity of being very different. These differences are determined by the unique properties of each particular gas, the nature of the sources and sinks for that gas, and the interactions of that gas with the surrounding environment. Thus, atoms that are liberated from the surface by some source mechanism and that are initially gravitationally bound will later impact the surface. If these atoms do not stick to the surface, they will move independently from point to point on the surface by ballistic hops. The general situation is illustrated in Figure 1. In addition to the source characteristics, the number and shape of these ballistic hops are determined by (1) the relevant forces acting on each atom, (2) the nature of the gas-surface interactions, and (3) the various loss processes that are operative. The relevant forces are the gravitational field of the Moon and the solar radiation pressure acceleration experienced by the atoms. For sodium and potassium, solar radiation acceleration is a small fraction of the lunar gravitational acceleration near the surface where the thermal atoms reside. On the other hand, solar radiation acceleration can be a significant fraction of the lunar gravitational acceleration at higher altitudes, which is the appropriate spatial domain for nonthermal atoms. The solar radiation acceleration for sodium and potassium depends upon the radial velocity of the atom with respect to the Sun because of the Fraunhofer absorption features in the solar spectrum. This dependence, to be discussed later, can produce observable variations in the spatial distribution of sodium and potassium about the Moon. The gas-surface interactions are determined by various physical and chemical processes that are not well understood but that at least depend on the local surface temperature and composition. These processes, discussed in § 2.4, determine the probability that an atom upon encountering the surface will stick to it for a long time or, alternatively, will rebound nearly instantaneously from it with a kinetic energy that may be accommodated to some degree with the local surface temperature. The loss processes for atoms in the sunlit hemisphere include dayside surface capture, gravitational escape, photoionization followed by solar-wind convection, and, for nonthermal atoms, lateral transport to the nightside.

Atoms that are liberated from the surface by various source mechanisms are called "source atoms" and may be thermal or nonthermal in nature. Source atoms that encounter the surface and have one or more additional ballistic hops are called "ambient atoms" and form the bound component of the atmosphere. These two components of the atmosphere were introduced by Hunten, Morgan, & Shemansky (1988) to clarify the role of the initial source and the gas-surface interactions in forming an exospheric atmosphere and have since been generally adopted in the literature. Source atoms that initially have sufficient energy to escape gravitationally from the Moon (or ambient atoms that eventually gain sufficient energy to escape) will form an atmospheric coma. Because of the action of solar radiation acceleration, the sodium and potassium comae for nonthermal atoms will have a sunward neutral pause and an

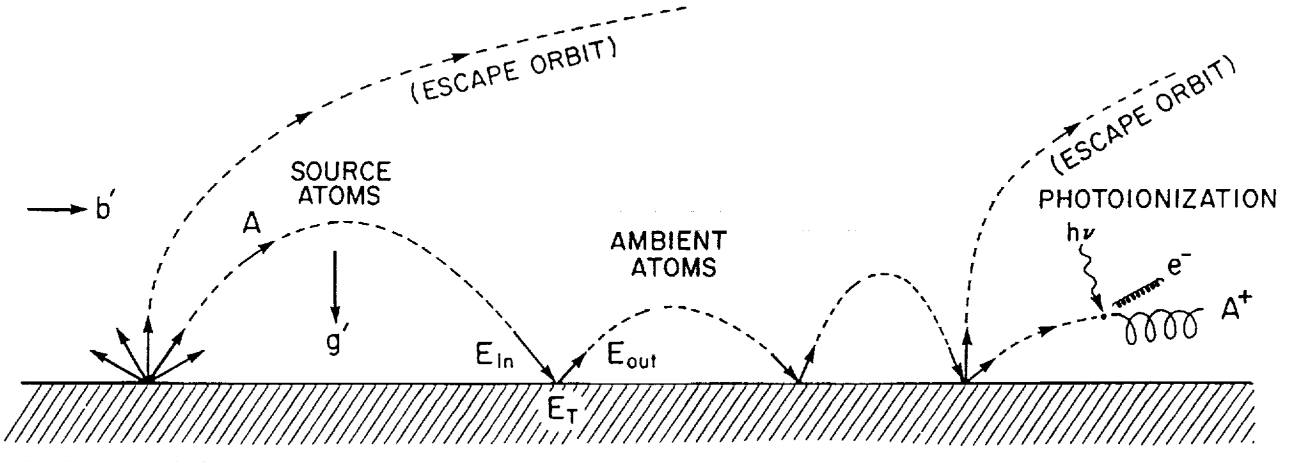

FIG. 1.—Atom dynamics in exospheric atmospheres. The different trajectories of source atoms liberated from the surface (at the left) and of the ambient atoms subsequently created when source atoms rebound from the surface are shown under the influence of local gravity (g'), solar radiation acceleration (b'), gas-surface encounters, and photoionization.

antisunward tail structure similar to that of a comet coma, as noted by Ip (1991). The local vertical density structure of the atmosphere is basically determined by the relative populations of the ambient atoms and the source atoms as well as the degree of thermal accommodation achieved by the ambient atoms as they migrate on the surface. The density distribution about the Moon is basically determined by the longitudinal, latitudinal, and time-dependent nature of the source mechanisms and the relative competition between the local lateral transport time and the loss lifetime of the atoms. The general situation is shown in Figure 2. Atoms reside in three different reservoirs: an external reservoir, an atmospheric reservoir, and a surface reservoir. As illustrated in Figure 2, the nature of the atmosphere is determined by the relative importance of processes that control the interchange between the atmospheric reservoir and the external and surface reservoirs. Source atoms for the atmospheric reservoir are initially supplied by various external and surface source mechanisms and will generally have both escape and ballistic components. If the source has only an escape component, the atmospheric structure is rapidly determined, and the process in Figure 2 terminates at point 1. If a ballistic component exists, the ballistic atoms may be captured by the surface (i.e., stick to the surface) upon impact. If all ballistic atoms stick to the surface, the atmospheric structure is established totally by the source atoms, and the process is terminated at point 2. If, however, the ballistic component is not captured (or only partially sticks to the surface), an ambient atmosphere is produced. Subsequent interactions of ambient atoms with the surface or with solar radiation may cause some of these atoms to escape (point 3). Energetic ambient atoms from the dayside atmosphere on long ballistic orbits may populate the nightside atmosphere directly. Less energetic ambient atoms in the dayside (nightside) atmosphere may populate the nightside (dayside) atmosphere by lateral transport that may be enhanced (retarded) by solar radiation acceleration. The remaining ambient atoms migrate on the surface and contribute to the two-dimensional structure of the atmosphere. Some fraction of atoms in the nightside atmosphere may also be captured by the surface and returned to the dayside atmosphere by the rotation of the Moon (point 5). Atoms in the dayside or nightside atmosphere may undergo ionization (point 4) and be either lost from the Moon by magnetospheric convective loss or recycled to the Moon by surface capture (point 6). The spacetime dependent nature of the source mechanisms and the nature of the gas-surface interactions for the Moon remain the central quantities that must be deduced unambiguously from observational data for sodium and potassium.

The four primary factors—sources, sinks, gas-surface interactions, and transport dynamics—that control the spatial distribution of sodium and potassium in the lunar atmosphere will now be discussed. Although these factors are conceptually distinct, they are coupled in the observational brightness data for the atmospheres and are not easily separated uniquely. It is therefore particularly important to understand these factors individually and to include their spacetime dependencies properly in models in order to be able to interpret correctly various atmospheric observations.

2.2. *Sources*

Four surface processes have been suggested in the literature to populate the lunar sodium and potassium atmospheres: (1) thermal desorption, (2) solar photon-induced desorption, (3) sputtering by solar wind ions, and (4) impact vaporization of the regolith (and impactors) by the steady influx of micrometeoroids. Atoms released from the surface by thermal desorption may be present locally or provided by source atoms that upon encountering the surface are thermally accommodated and produce an ambient atom atmosphere, if the thermal desorption time is short compared to the ballistic flight time. For sodium atoms, estimates of the source rates for the latter three processes are summarized in Table 2. Values for the sodium flux from photodesorption vary by several orders of magnitude and depend critically upon the uncertain yields and the portion of the solar spectrum that is physically applicable to the sputtering process. Values for the sodium flux from solar wind sputtering vary from 1.5×10^5 atoms cm^{-2} s^{-1}, using the early-estimated and larger yields for a fresh regolith surface of McGrath, Johnson, & Lanzerotti (1986) adopted by Morgan, Zook, & Potter (1989), to 2.4×10^3 atoms cm^{-2} s^{-1},

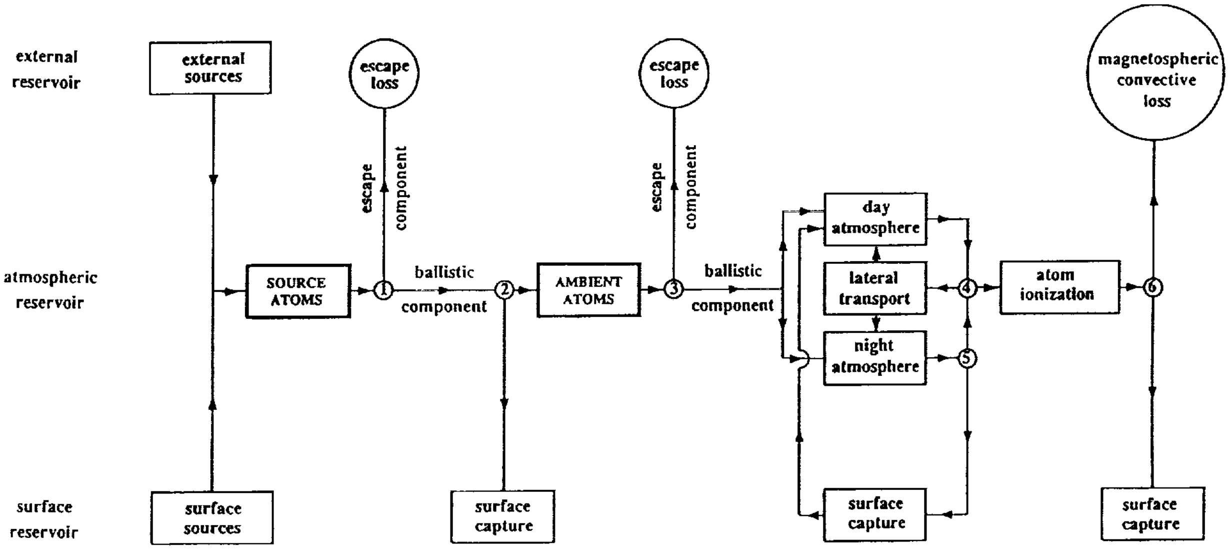

FIG. 2.—Interchange of gas between external, atmospheric, and surface reservoirs. The development of the exospheric atmosphere depicted pictorially in Fig. 1 is shown in a more interactive physical manner. See text for discussion.

TABLE 2

ESTIMATES FOR THE SODIUM SOURCE ATOM FLUX FROM THE LUNAR SURFACE

Sodium Flux[a] (atoms cm^{-2} s^{-1})	Sodium Regolith Fractional Abundance f_{Na}	Yield Y (neutrals per photon or ion)	Solar or Ion Flux Φ (photons or ions cm^{-2} s^{-1})	Reference
Photon-Stimulated Desorption:				
3×10^6–3×10^7......	0.002	$(Y\Phi = 1.5 \times 10^9\text{–}1.5 \times 10^{10})$[b]		1
3×10^4................	0.002	$(Y\Phi = 1.5 \times 10^7)$[h]		2
5×10^3................	0.0033	10^{-6}	1.5×10^{12}	3
Solar Wind Sputtering:				
1×10^5................	0.0033	0.1 (H^+)[c]	3×10^8	4
0.5×10^5.............	0.0033	1.0 (He^{++})[c]	(1.5×10^7)[d]	4
2.4×10^3.............	0.0033	0.003	(2.4×10^8)[e]	3
Meteoritic Impact Vaporization:				
7.4×10^3.............	0.0033	(Regolith)	...	5
1×10^5................	0.0033	(Regolith)	...	4
0.2×10^5.............	...	(Meteoroid)	...	4
$(5.3\text{–}6.2) \times 10^3$	0.0033	(Regolith)	...	6

[a] The sodium flux is determined by the product $f_{\mathrm{Na}}\, Y\Phi$.

[b] Estimates at Mercury scaled to 1 AU by using Mercury's heliocentric distance equal to its semimajor axis.

[c] Yields estimated by McGrath et al. 1986.

[d] Original He^{++} flux corrected from 10% to 5% of the H^+ solar wind ion flux.

[e] Effective flux that produces the yield Y derived for a sputter desorption surface rate of 0.031 Å yr^{-1} and a surface density of 2.7 g cm^{-3}.

REFERENCES.—(1) McGrath et al. 1986; (2) Killen et al. 1990; (3) Morgan & Shemansky 1991; (4) Morgan et al. 1989; (5) Gault et al. 1972; (6) Cintala 1992.

based incorrectly by Morgan & Shemansky (1991) upon the much smaller net erosion rate, not the larger sputtering rate (see Johnson & Baragiola 1991). The most recent sodium flux for micrometeoroid impact vaporization is given by Cintala (1992) and is similar to the earlier value of Gault, Hörz, & Hartung (1972) but is more than an order of magnitude smaller than the recent estimate of Morgan et al. (1989). The estimate of Cintala is based on calibrated physical calculations while the estimate of Morgan et al. is based upon a similarity argument relating the vapor mass to the infall mass, which has been obtained in model simulations for large impactors in the limit of high impact speeds (when the similarity factor is ≥ 40; see O'Keefe & Ahrens 1977). The large difference occurs primarily because of a factor of 4 lower micrometeroid mass infall flux used by Cintala (1992) and because of an inflated vapor-mass to infall-mass factor of 5.4 used by Morgan et al. as compared to its updated value of 0.63 (see Cintala for discussion) or Cintala's value of 1.4. For the lunar context, a vapor mass that is comparable or smaller than the infall mass is believed to be more appropriate (Ahrens 1994) and would therefore yield a downward adjusted sodium source flux for Morgan et al. of $\sim(2\text{–}3) \times 10^4$ atoms cm^{-2} s^{-1}. A more recent estimate of the micrometeoroid mass infall flux (Love & Brownlee 1993) indicates that the lower value used by Cintala should be increased by a factor of ~ 3.7, which adjusts upward his sodium source flux to a value of $\sim(2.0\text{–}2.3) \times 10^4$ atoms cm^{-2} s^{-1}. Thus, a best estimate for the sodium flux from micrometeoroid impact vapor would appear to be $\sim(2\text{–}3) \times 10^4$ atoms cm^{-2} s^{-1}.

Each of the four source mechanisms has a somewhat distinct energy distribution for the liberated atoms and will therefore make distinct contributions to certain spatial regions of the two-dimensional sodium and potassium lunar atmospheres on the sky plane. Atoms supplied by thermal desorption (i.e., lunar subsolar temperature is ~ 400 K) will essentially all be ballistic in nature and hence contribute to the atmospheric density relatively close to the surface (i.e., altitudes ≤ 400 km which is between 1.0 and ~ 1.2 lunar radii). For photodesorption, measurements by Arlinghaus et al. (1989) using a 3080 Å laser beam have shown that Zn atoms liberated from a ZnS single crystal have a yield of $\sim 10^6$ Zn per photon and a velocity distribution that is Maxwell-Boltzmann in nature with a peak that corresponds to a temperature of 1880 K for a photon intensity ablation fluence of 17 mJ cm^{-2} and decreases as the ablation fluence decreases. This Maxwell-Boltzmann velocity distribution is in marked contrast to their findings for Zn atoms ejected by 3 keV Ar^+ ion bombardment of both a Zn surface and a ZnS single crystal, where the ejected Zn atoms exhibited the well-known Sigmund-Thomson sputtering flux velocity distribution which has a peak at a higher velocity and, asymptotically, decays much less rapidly (i.e., $\sim v^{-4}$). In addition, more recent and preliminary experimental results by Wiens et al. (1993) using a 3080 Å laser beam for photodesorption of sodium atoms from a Na_2SO_4 surface were obtained in the low-intensity regime, where thermal effects are negligible and for even lower values of the ablation fluence than noted above. These measurements demonstrated a yield of $\sim 10^{-7}$ Na per photon and a sodium velocity distribution with a peak that corresponds to an even lower temperature (< 800 K) than that for Zn. Other studies of thermal metal atoms generated by photodesorptive processes also demonstrate a low-temperature Maxwellian for the liberated metal neutrals (Townsend 1983; Haglund & Tolk 1986).

Sodium and potassium atoms liberated from the porous lunar regolith by solar wind ion sputtering or solar photon-induced desorption will be characterized by a mixture of a direct source atom velocity distribution and a delayed source atom velocity distribution. The direct source atom velocity distribution is produced by atoms that are sputtered upward without any collisional encounters with the regolith, while the delayed source atom velocity distribution is produced by atoms that are sputtered and undergo one or more collisional encounters with the regolith before exiting it in an upward flux. The delayed source will therefore be a quasi-thermalized velocity distribution, with a characteristic temperature that is somewhere between the local surface temperature and the characteristic temperature of the direct source velocity distribution. The amount of thermalization will depend on the degree of the surface porosity and the detailed properties of the gas-surface interactions (e.g., dependence of the sticking and energy accommodation coefficients for the regolith material on the atom velocity and the surface temperature). Based upon the work of Hapke (1986; Hapke & Cassidy 1978), the relative sputtered strengths from a porous lunar surface for the direct source, the delayed source, and the source component that sticks in the regolith and does not contribute to the atmosphere are, respectively, approximately 10% (3% including macroscopic roughness), 68% (74% including macroscopic roughness), and 22% (23% including macroscopic roughness) for sodium and 10% (3% including macroscopic roughness), 85% (91% including macroscopic roughness), and 5% (6% including macroscopic roughness) for potassium.

The direct source atom velocity distribution for solar wind sputtering will be characterized by a Sigmund-Thompson sputtering flux velocity distribution, which typically has a peak in the range of 1–3 km s^{-1} depending upon the binding energy of atoms to the surface. For solar photon-induced desorption, the direct source atom velocity distribution is likely to be Maxwellian-like and characterized by a temperature of the order of ~1000 K or so (i.e., ~800–1880 K), assuming the laboratory measurements noted above are applicable to the lunar surface and can be interpreted as a direct source. For the delayed source, the quasi-thermalized velocity distribution for solar wind sputtering should therefore probably be at least mildly nonthermal in nature, while for the solar photon-induced desorption it might be more thermalized, because the direct source for photosputtering appears to be hotter than the surface but cooler than the Sigmund-Thompson sputtering flux velocity distribution. The atmosphere for solar wind sputtering would therefore have a minor component from the direct source that extends to larger distances above the Moon and exhibits a power-law column density gradient that is significantly less steep ($\sim r^{-2.5}$; see Johnson 1990) than that for a photodesorption source (because of the much less steep slope of the tail of the Sigmund-Thompson velocity distribution) and a major component from the delayed source that is likely somewhat hotter than the local surface temperature. The atmosphere for solar photon-induced desorption will therefore have a minor component from the direct source that is likely similar in nature to that for the major component of the solar wind and have a major component from the delayed source that is cooler and therefore more localized near the surface. For both the solar wind and photon-induced desorption sources, the direct and delayed source strengths should approximately decrease by a cosine of the departure angle from the subsolar point. Furthermore, the source strength, angular distribution, and speed distribution generated by the oblique impact of the solar wind ions and photons with the surface further from a subsolar point may also vary because of angular and temperature effects that modify in more complex ways the direct and quasi-thermalized delayed sources exiting the cooler regolith.

For impact vaporization of the lunar surface by micrometeoroids, the initial vapor cloud is present in the prompt ejecta and, for volatiles such as sodium and potassium, may be produced from the liquid melt and from the heated, shocked, and fractured solid regolith. The relative proportions of vapor mass and the velocity characterizations of the vapor for these three components are not well known. The velocity of the prompt vapor may be at least comparable to the highest temperature of vaporization (~3000 to 4000 K) represented by the vaporized product constituents of the regolith as discussed by Ahrens & O'Keefe (1971) and may perhaps have a high-speed component as large as or even larger than the impact speed of the micrometeoroids with the regolith, which for the Moon have an average value of ~15 km s^{-1} (Morgan et al. 1989). If present, such a high-speed component would rapidly escape the lunar atmosphere (escape speed 2.4 km s^{-1}) and produce a dim, nearly invisible brightness profile. The vapor produced by micrometeoroid sized projectiles impacting different surfaces has been estimated to have a temperature of 2500 to 5000 K from Planck function fits to the impact flash spectrum by Eichhorn (1978), although the initial temperature produced during the impact is likely significantly higher. Vapor produced from the liquid and the heated, shocked, and fractured solid regolith is likely to be more characterized by the melt temperature of the regolith constituents, which is generally ~1400 to 3000 K, with sodium- and potassium-bearing compounds occurring at the low end of the temperature range (Ahrens & O'Keefe 1971). Given the general uncertainty of this situation, it is therefore likely that a significant fraction of the sodium and potassium produced by impact vaporization will produce an extended lunar atmosphere which at large distances from the Moon will have a density gradient that is controlled by a somewhat Maxwellian velocity distribution with a characteristic temperature of several thousand degrees. The source for this atmosphere should be somewhat isotropic and perhaps organized with azimuthal symmetry on the lunar hemisphere facing in the direction of Earth's orbital motion, which is the forward-moving surface assumed to collect the micrometeoroids in the estimates for the sodium vapor fluxes in Table 2.

2.3. *Sinks*

The lifetime of sodium and potassium atoms in the lunar sunlit atmosphere is dominated by photoionization and has values of ~15 hr and ~10 hr respectively. Except in the lunar shadow, where they are not operative, the photoionization lifetimes of sodium and potassium are essentially constant, since the Moon-Sun distance does not vary significantly. The next most important limiting lifetime process for sodium and potassium is electron impact ionization in the solar wind with a nominal value of ~360 hr for sodium and ~250 hr for potassium. The ambient atmosphere is shielded from the direct interactions with the variable conditions for the solar wind only when the Moon is within the magnetotail of Earth, which occurs for about one-sixth of the lunar orbit.

2.4. *Gas-Surface Interactions*

The gas-surface interactions are determined by various physical and chemical processes that can be rather complex and are not well understood. The subject has been discussed by Shemansky & Broadfoot (1977) and more recently for sodium and potassium by Hunten et al. (1988) as well as Shemansky (1993). Physical adsorption is generally described by an energy accommodation coefficient β and by an atom residence time for adsorption that are strongly dependent on surface composition, structure, and temperature. The energy accommodation coefficient β is defined by

$$\beta = \frac{(E_{\text{out}} - E_{\text{in}})}{(E_T - E_{\text{in}})} , \tag{1}$$

where the energy of the atom (see Fig. 1) is E_{in} before impact and E_{out} after impact and where the thermal energy of the surface is denoted by E_T. In the atmospheric model described in § 3, this coefficient includes any process (e.g., single and multicollisional physical adsorption encounters with the surface) that partially thermalizes the atom and then allows it to exit the surface in a residence time for physical adsorption that is typically much shorter than a local ballistic timescale. The energy accommodation coefficient is defined so that $\beta = 0$ for 0% surface accommodation (elastic bounce) and $\beta = 1$ for 100% surface accommodation.

For the ideal case of a 600 K α-quartz flat surface, the value of the energy accommodation coefficient for a single collisional encounter event with the surface has been calculated to be 0.62 for sodium and 0.26 for potassium (see Table IV in Hunten et al. 1988). These values imply that sodium and potassium would accommodate to the surface of the Moon in a few bounces. As discussed by Hunten et al. (1988), the residence times for physical adsorption depend exponentially on the temperature and increase rapidly as the temperature decreases. For a surface temperature of 200 K, 100 K, and 80 K, the residence times for single-collisional physical adsorption are 3.6×10^{-7} s, 0.71 s, and 1000 s for sodium and 2.0×10^{-7} s, 0.16 s, and 150 s for potassium, respectively. These residence times are an extremely small fraction of a second for surface temperatures typical of the sunlit hemisphere of the Moon (where the subsolar temperature is approximately 400 K) so that the surface reservoir time should be insignificant compared to a ballistic hop time. For nightside temperatures which may be a little cooler than 100 K, the residence times rapidly become much larger than 1 s and can then begin to compete favorably with the ballistic hop times of atoms so that the nightside surface reservoir begins to capture the nightside ambient atoms. The effect of long residence times for physical adsorption on cooler surfaces and the even more complex chemical adsorption (or other effective bonding of atoms to the surface) on hot or cooler surfaces will be collectively described in the atmospheric model in § 3 by a surface sticking coefficient, which is the probability that an atom upon encountering the surface will stick to it. The introduction of both the effective energy accommodation coefficient and the sticking coefficient provides the flexibility to cover a broad range of appropriate physical cases of interest.

2.5. *Transport Dynamics*

The transport dynamics of sodium and potassium atoms in the lunar atmosphere are dependent upon the acceleration of gravity and also the solar radiation acceleration produced by solar resonance scattering of sodium in the D emission lines (5890 Å, 5896 Å) and solar resonance scattering of potassium in its corresponding emisson lines (7665 Å, 7699 Å). Solar radiation acceleration can, in general, have three major effects on the transport dynamics of sodium and potassium atoms. It can (1) cause source atoms to escape the Moon, (2) cause source atoms to be carried in one long ballistic trajectory to the nightside of the Moon, or (3) drive a lateral (antisunward) transport of the ambient atoms along the sunlit surface. The importance of these effects depends upon the magnitude of the solar radiation acceleration and the velocity distribution for the source atoms.

For sodium or potassium, the magnitude of the solar radiation acceleration depends primarily on the Doppler shift of the atom out of the bottom of the solar Fraunhofer feature which determines the solar resonance scattered brightness available for the atom. For no atom Doppler shift (i.e., a zero atom-Sun radial velocity), the radiation acceleration at a nominal heliocentric distance of 1 AU is 2.71 cm s^{-2} (i.e., ~1.7% of surface gravity) for sodium and 5.33 cm s^{-2} (i.e., ~3.3% of surface gravity) for potassium. The solar radiation accelerations will, however, generally be larger since atoms do have radial velocities relative to the Sun. The Doppler shift will depend upon the heliocentric radial component of the vector sum of the velocity of the Moon with respect to the Sun and the instantaneous velocity of the atom with respect to the Moon. For an atom stationary in the sunlit lunar atmosphere, its radial velocity is that of the Moon relative to the Sun, which is given in Figure 3 for the year 1993. This radial velocity varies as the Moon moves about Earth with its synodic period of ~29.5 days (where, to lowest order, the Moon is on a circular orbit with a speed of ~1.0 km s^{-1} plus some three-body motion of order of ~0.1 km s^{-1} or less) and as Earth moves about the Sun with a period of 1 yr (where, to lowest order, Earth is on an elliptic orbit with a maximum radial velocity of ~+0.5 km s^{-1} in the spring of the year and ~−0.5 km s^{-1} in the fall of the year). The radial velocity is essentially symmetric about zero in early January, when the Earth is at perihelion, and in early June, when the Earth is at aphelion. The maximum positive velocities for a stationary atom thus occur in the spring at first quarter, and the maximum negative velocities occur in the fall at last quarter. Based upon the radial velocity in Figure 3 and the corresponding three-body variation in the heliocentric distance, the solar radiation acceleration experienced by a stationary atom in the sunlit atmosphere is shown for sodium and potassium, respectively, in Figures 4 and 5. In both figures, the envelope of values for the solar radiation acceleration is indicated at first quarter by the dot-dashed line and at last quarter by the dashed line. For each lunar period, the minimum value of solar radiation acceleration experienced by a stationary atom occurs at second quarter (i.e., full Moon) where the heliocentric radial motion of the Moon about Earth is near zero and where the heliocentric distance of the Moon is a local maximum. The solar radiation acceleration in Figures 4 and 5 varies considerably, being substantially larger than or slightly smaller than the minimum values noted above for the nominal heliocentric distance of 1 AU. The nonzero instantaneous velocity of a sodium or potassium atom in the sunlit atmosphere will, however, significantly alter (i.e., enhance or reduce) the solar radiation acceleration in Figures 4 and 5 experienced by a stationary atom in the lunar atmosphere. This alteration occurs because the nonthermal velocities (~1–2 km s^{-1}) of sodium atoms (and therefore likely for potassium atoms as well) required for the surface sources to populate the more distant portions of the observed subsolar corona are comparable to the Moon-Sun radial velocities in Figure 3. The instantaneous velocity of sodium or potassium atoms will therefore affect the structure of the atmosphere in different ways during the year as discussed below.

The structure of the sodium and potassium atmospheres will be time variable with season of the year and lunar phase because of the time-dependent solar radiation acceleration. For the Moon near first quarter in the spring of the year, the instantaneous atom velocities will produce lunar sodium and

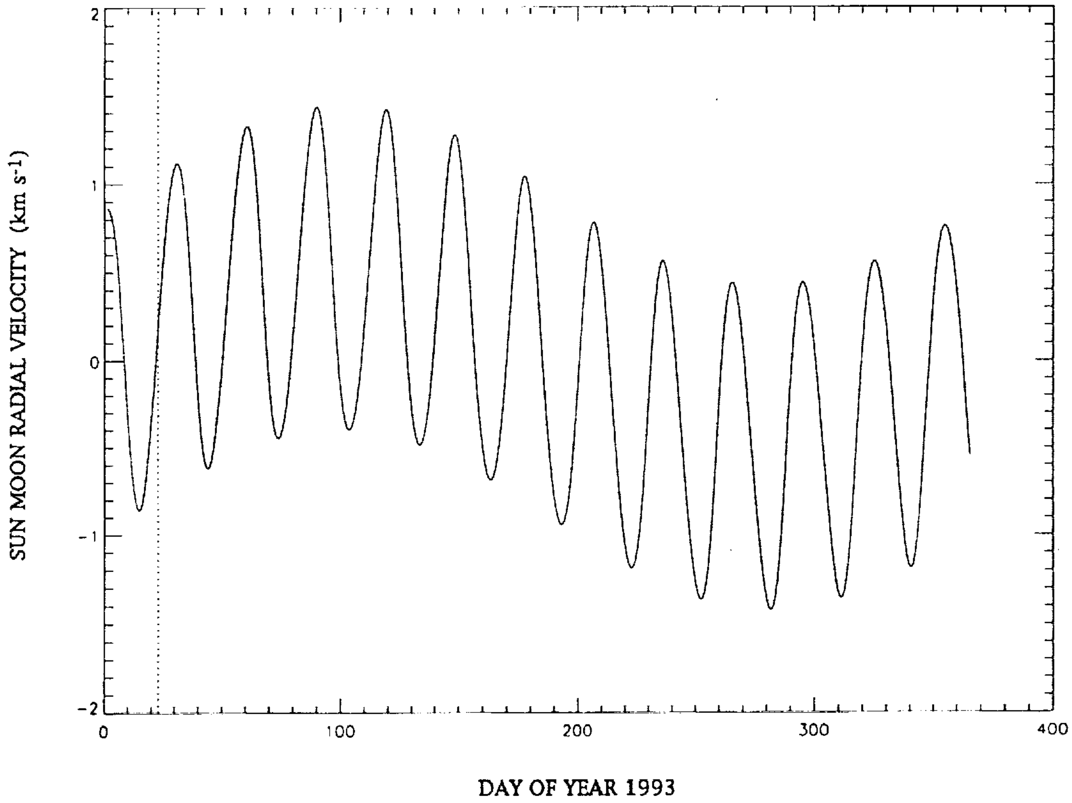

FIG. 3.—Sun-Moon radial velocity. The radial velocity is shown as a function of time during the year 1993 and is based upon Brown's theory of the Moon's motion (Battin 1964). Positive velocity is motion away from the Sun. The vertical dotted line indicates the location of the start of the lunar period (i.e., new Moon).

potassium atmospheres that are spatially expanded in the sunlit hemisphere and have an enhanced escape population in the antisunward coma. For the Moon near last quarter in the fall of the year, the instantaneous atom velocities will produce lunar sodium and potassium atmospheres that are spatially contracted in the sunlit hemisphere and have a larger bound population in the antisunward coma. This can be understood as follows. Since most of the upward moving atoms in the sunlit hemisphere have a velocity component that is toward the Sun, this atom velocity component will either at first quarter partially or completely cancel the maximum velocity of the Moon moving away from the Sun (which occurs in the spring) or at third quarter be added to the maximum velocity of the Moon moving toward the Sun (which occurs in the fall). In the spring at first quarter, this cancellation will reduce the Doppler shift and hence the solar radiation acceleration experienced by these atoms below values at that time in Figures 4 and 5. As a result, the subsolar altitudes will be larger so as to produce an expanded sunlit atmosphere in the spring at first quarter. On the other hand, in the fall at last quarter the larger resultant radial velocity component will produce a larger Doppler shift and hence a larger solar radiation acceleration than shown at that time in Figures 4 and 5. This larger solar radiation acceleration will reduce the subsolar altitudes of the atoms and thereby produce a contracted sunlit atmosphere in the fall at third quarter. This reduction of the solar radiation acceleration in the spring at first quarter and its enhancement in the fall at third quarter are illustrated in Figure 6*a* for a sodium atom moving relative to the Moon with an instantaneous velocity of 1 km s^{-1} toward the Sun. In contrast, for atoms in the expanded portion of the sunlit corona or in the corona beyond the terminator that have an instantaneous velocity component that is directed antisunward, this atom velocity component will be either at first quarter aligned with the maximum velocity of the Moon moving away from the Sun (occurring in the spring), causing the resultant radial velocity of the atoms with respect to the Sun to be larger, or at third quarter antiparallel with the maximum velocity of the Moon toward the Sun (occurring in the fall), causing the resultant radial velocity of the atoms with respect to the Sun to be partially or completely canceled. At first quarter in the spring, this larger radial velocity will produce a larger Doppler shift and hence a larger solar radiation acceleration than shown at that time in Figures 4 and 5. This larger solar radiation acceleration will enhance the escape of atoms from the gravitational grasps of the Moon in the antisunward coma in the spring at first quarter. In contrast in the fall at last quarter, the smaller radial velocity will reduce the Doppler shift and hence the solar radiation acceleration experienced by these atoms below those values shown at that time in Figure 4 and 5. This smaller solar radiation acceleration will reduce the escape of atoms from the gravitational field of the Moon in the antisunward coma in the fall at third quarter. This enhancement of the solar radiation acceleration in the spring at first quarter and its reduction in the fall at the last quarter are illustrated in Figure 6*b* for a sodium atom moving relative to the Moon with an instantaneous velocity of 1 km s^{-1} away from the Sun. Simple illustrations of these effects in the luminance equator in the spring at first quarter and in the fall at third quarter are given, respectively, for sodium and potassium atoms in Figures 7*a* and 7*b*.

The initial surface distribution of any ambient atom atmosphere that is produced when bound source atoms encounter

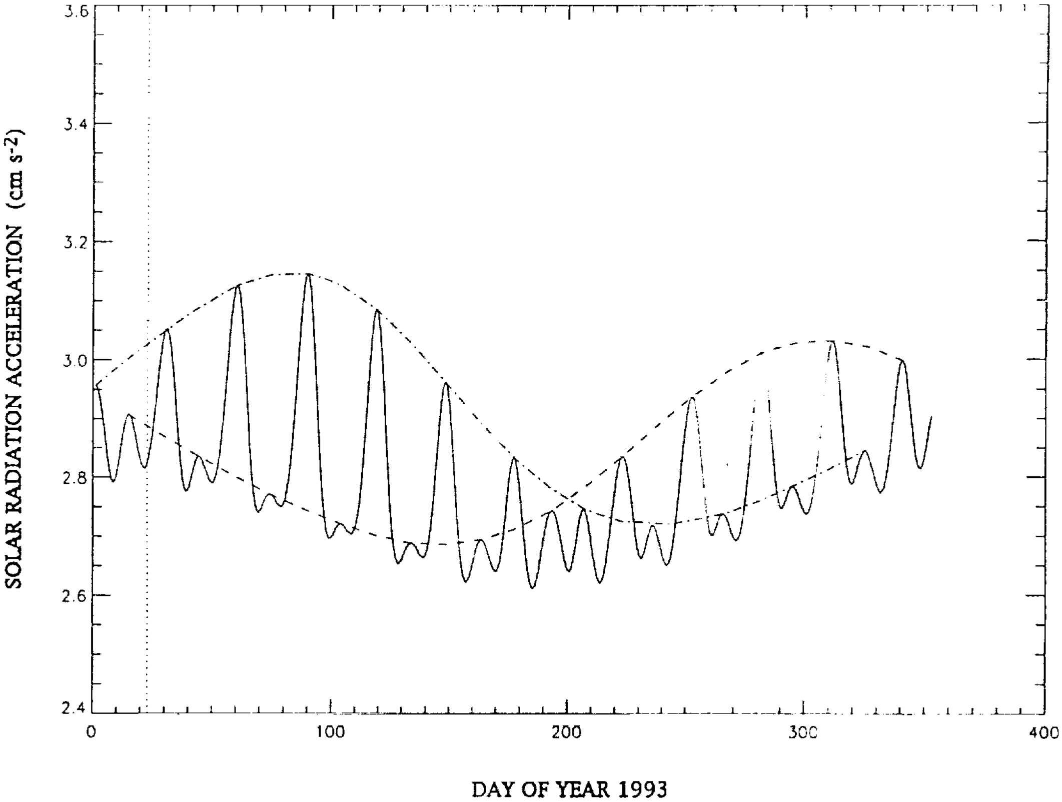

FIG. 4.—Solar radiation acceleration for stationary sodium atoms in the lunar atmosphere. The radiation acceleration experienced by stationary sodium atoms in the lunar atmosphere due to solar resonance scattering in the sodium D-lines (5890 Å, 5896 Å) is shown as a function of time during the year 1993 and is based upon the Sun-Moon radial velocity in Fig. 3 and the corresponding changes in the heliocentric distance. The vertical dotted line indicates the location of the start of a lunar period (i.e., new Moon). The envelope of values for the solar radiation acceleration is indicated at first quarter by the dot-dashed line and at last quarter by the dashed line.

the sunlit surface will therefore also change with season and lunar phase. This relative angular distribution on the lunar surface of this ambient atom atmosphere will be preserved if the local transport time is long compared to the photoionization lifetime. Neglecting solar radiation acceleration, the local transport time is determined by the random walk of atoms along the surface for ballistic orbits appropriate to the surface temperature. For a nominal dayside surface temperature of 300 K and a characteristic distance of one lunar radius, the characteristic transport time is ∼75 hr for sodium and ∼166 hr for potassium. Since the transport times for sodium and potassium are much larger than their photoionization lifetimes of 15 and 10 hr, respectively, the local density is determined by the velocity distribution and source rate for the source atoms, the locally created population of the ambient atoms, and the photoionization rate. Although the inclusion of the solar radiation acceleration introduces a lateral (antisunward) transport, the maximum values of the radiation acceleration in Figures 4 and 5 are too small to sufficiently reduce the transport time for thermal atoms so as to alter this conclusion, although for potassium the (antisunward) transport time is on the verge of being important.

3. MODELS FOR SODIUM AND POTASSIUM ATMOSPHERES

Models for the sodium and potassium atmospheres of the Moon have been developed which incorporate the factors discussed in the theoretical overview. The models are numerical and Monte Carlo in nature and are appropriate for studying the relative importance of various physical processes and for simulating and analyzing various observational data acquired by ground-based facilities for the solar resonance scattered emission brightnesses in the D-lines of sodium atoms (5890 Å, 5896 Å) and potassium atoms (7665 Å, 7699 Å). The model calculates the three-dimensional sodium and potassium densities about the Moon and also the projected two-dimensional column densities as well as the solar resonance scattered image brightnesses of the emission lines on the sky viewing plane. High-resolution line profiles for the emission lines may also be calculated for a given field of view. The dependence of the solar resonance scattered brightness on the instantaneous radial motion of each atom with respect to the Sun (which varies because of the solar Fraunhofer features) is incorporated in the calculation and includes the instantaneous motion of the atom with respect to the Moon as well as the Moon's motion relative to the Sun based upon Brown's theory (see Battin 1964). Only single scattered photon events in the optically thin limit are required for the lunar data. For emission brightness and gas density calculations, the model can adopt an initial source flux velocity-distribution on the surface of the Moon that is both spatially (i.e., longitude and latitude) and time dependent.

The density of the exospheric atmosphere is calculated by following the trajectories of a large number of atoms that have initial conditions on the surface determined by an adopted source mechanism. The only collisions that occur for atoms are with the surface if the source atoms do not initially escape. The individual atom orbits are determined by numerically inte-

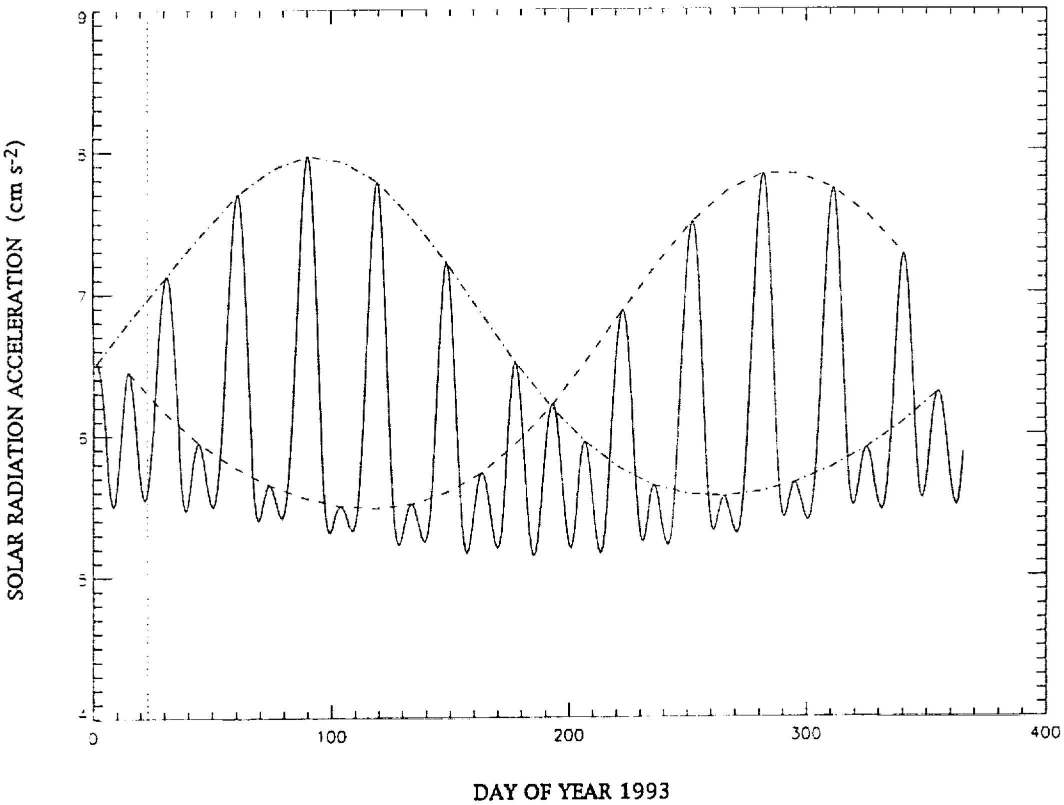

FIG. 5.—Solar radiation acceleration for stationary potassium atoms in the lunar atmosphere. The radiation acceleration experienced by stationary potassium atoms in the lunar atmosphere due to solar resonance scattering in the potassium lines (7665 Å, 7699 Å) is shown as a function of time during the year 1993 and is based upon the Sun-Moon radial velocity in Fig. 3 and the corresponding changes in the heliocentric distance. The vertical dotted line indicates the location of the start of a lunar period (i.e., new Moon). The envelope of values for the solar radiation acceleration is indicated at first quarter by the dot-dashed line and at last quarter by the dashed line.

grating the equations of motion using a fourth-order Runge-Kutta method with small but dynamically determined time steps. The equations of motion include the gravity of Earth, the radially dependent acceleration of the gravity of the Moon, and the antisunward-directed radiation pressure acceleration experienced by these atoms as they undergo solar radiation scattering in their emission lines. The gravity of Earth contributes only small centrifugal and Coriolis terms because of the motion of the Moon about Earth but is otherwise not directly significant near the Moon since the Moon-Earth Lagrange radius (i.e., the average radial distance from the Moon of the L1 and L2 Lagrange points where Earth gravity, lunar gravity, and centrifugal forces balance) is ~35 lunar radii. This average Lagrange radius is also significantly larger than the radial distance of ~7.5 lunar radii and ~5 lunar radii for sodium and potassium atoms, respectively, where the solar radiation acceleration has already equaled or exceeded the lunar gravity. The dependence of the solar radiation acceleration on the instantaneous radial velocity of each atom with respect to the Sun as discussed in § 2.5 is fully included as well as the shadow of the Sun cast by the Moon. When the atom orbit encounters the surface of the Moon, its gas-surface interactions are described by a sticking coefficient (i.e., minimum value: 0 = no sticking; maximum value: 1 = 100% sticking) and the energy accommodation coefficient β (i.e., minimum value: 0 = no accommodation; maximum value: 1 = 100% accommodation to the local surface temperature). The two coefficients may be specified in different combinations to simulate a variety of physical and chemical conditions. If the atom bounces on the surface (i.e., if the sticking coefficient is not unity), its velocity vector is directed upward with a randomly selected angle and with a velocity magnitude (i.e., corresponding energy E_{out} in eq. [1]) appropriate to its accommodation coefficient, where E_T is given by the most probable energy of a Maxwell-Boltzmann velocity distribution at the local surface temperature. The trajectory calculation is then continued with these new initial conditions. In the density calculation, the photoionization lifetime of the atom as it moves on its trajectory is also included, taking into account the Sun's shadow.

Model calculations to be undertaken in this paper will consider only source atoms that originate on the surface of the Moon. For the classical description of an exosphere for a body with a simple $1/r$ gravitational potential (Chamberlain 1963), this type of source includes the so-called ballistic orbits and escape orbits but excludes the so-called satellite orbits (i.e., bound orbits that do not intersect the lunar surface). The contribution of "satellite orbits" to the density of the lunar corona is expected to be negligible and will not be considered further in this paper, since the collision time of exospheric atoms to populate the "satellite orbits" is very long compared to the photoionization lifetime as noted by Sprague et al. (1992). It should be, however, noted in passing that with the addition of the solar radiation acceleration in the problem, the distinct classical boundary in phase space for "satellite orbits" is lost. Because of this additional force, "satellite orbits" in the near lunar corona can decay into either "ballistic orbits" as illus-

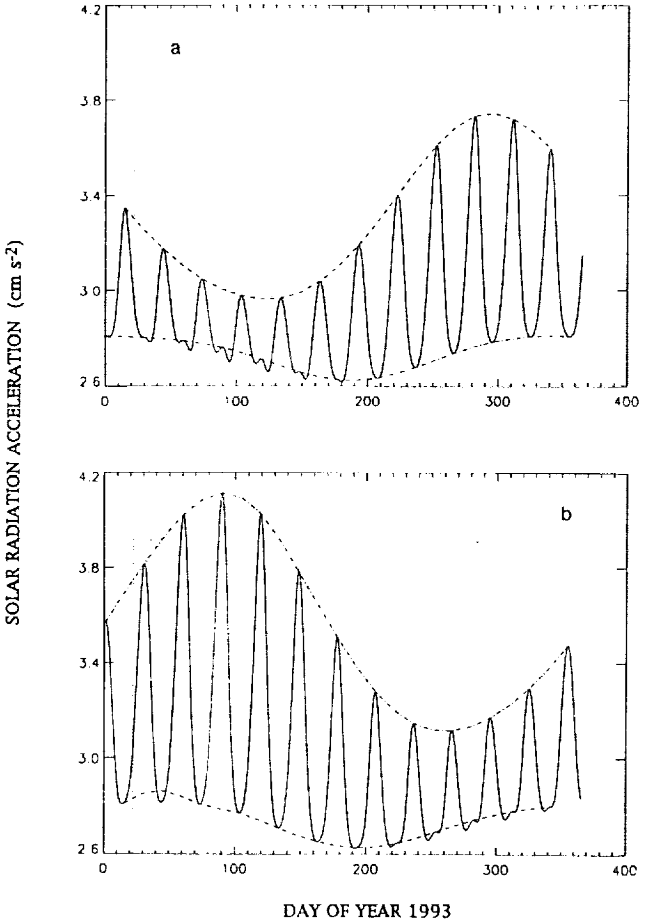

FIG. 6.—Solar radiation acceleration for moving sodium atoms in the lunar atmosphere. As a function of time during the year 1993, the solar radiation acceleration experienced in the lunar atmosphere by sodium atoms that are moving relative to the Moon with an instantaneous velocity of 1 km s^{-1} is shown in (*a*) when their motion is toward the Sun and in (*b*) when their motion is away from the Sun. The radiation acceleration is produced by solar resonance scattering in the sodium D-lines (5890 Å, 5896 Å) and is based upon both the instantaneous atom velocity and the Sun-Moon radial velocity in Fig. 3 with the corresponding changes in the lunar heliocentric distance. The vertical dotted line indicates the location of the start of a lunar period (i.e., new Moon). The envelope of values for the solar radiation acceleration is indicated at first quarter by the dot-dashed line and at last quarter by the dashed line.

trated in Figure 8 or "escape orbits" as illustrated in Figure 9 on the order of one unperturbed orbital period (e.g., 5.1 and 9.4 hr, respectively, for the circular orbits at 2 and 3 lunar radii).

To verify the model for the lunar atmosphere, it is first compared to the limiting case where the Moon is in an inertial system and has only a simple $1/r$ gravitational potential. For a Maxwell-Boltzmann velocity distribution at the exobase (here the lunar surface), this limiting case is given by Chamberlain (1963) where the spherically symmetric density is obtained by adding the classical analytic density expressions for the "ballistic orbits" and "escape orbits" (i.e., excluding the "satellite orbits"). Choosing a Maxwell-Boltzmann distribution for sodium with a temperature of 1000 K and integrating this analytic expression for the density to obtain the column density in the sky plane, a comparison of the normalized column density for the lunar Monte Carlo model and the analytic model of Chamberlain is given in Figure 10. The model and analytic results are in excellent agreement, with only minor statistical fluctuations present at distances of 3 lunar radii in the Monte Carlo calculation utilizing 100,000 atom orbits.

The introduction of solar radiation acceleration in the lunar atmosphere model will of course destroy the spherical symmetry of the Chamberlain atmosphere. To most simply illustrate this departure from spherical symmetry, a model simulation is undertaken for sodium where a constant solar radiation acceleration (i.e., independent of the instantaneous atom velocity) of 3.1 cm s^{-2} (near the maximum value for sodium in Fig. 4) is added to the otherwise r^{-2} dependence of the gravitational acceleration of the Moon. Adopting a uniform surface source for sodium with a 1000 K Maxwell-Boltzmann velocity distribution, the model simulation for the normalized column density is given in Figure 11. The effect of solar radiation, as expected, is to limit the vertical extent of the sunward atmosphere and produce an escaping tail in the antisunward atmosphere similar to that of a comet coma. The reduction in the radial column density profile at the subsolar point in comparison to the model-simulated spherically symmetric case of Chamberlain is illustrated in Figure 12. This reduction is caused by sodium atoms that are now blunted in their sunward motion and are given an angular motion around the Moon toward the terminator so as to remove atoms from the subsolar column and supply them to the antisunward bound and escaping coma. Model calculations including the more complex effects of the gravity of the Moon-Earth system and the full instantaneous atom-Sun velocity and heliocentric dependence of the solar radiation accelerations are similar in character to the results of Figure 11. As discussed in § 2.5, the variation of the solar radiation acceleration with the time of the year and the lunar phase of the Moon will produce spatial changes in the atmosphere for the same surface source. An example of this change is shown for sodium and potassium in Figures 13 and 14, respectively, for a uniform surface source with a Maxwell-Boltzmann velocity distribution. At first quarter in the spring of the year, there is an expanded sunward atmosphere with a larger population of escaping atoms in the tailward coma, while at last quarter in the fall of the year there is a contracted sunlit atmosphere with a smaller population of escaping atoms in the tailward coma. The column density difference in the sunlit atmosphere is more dramatic in the case of potassium than sodium because of the larger value of the solar radiation acceleration for potassium. For sodium, this behavior has recently been reported in the antisunward coma, where the presence of an escaping coma was seen in the late winter (1991 February 20) observations of Mendillo et al. (1991) acquired when the Moon was nearing first quarter but not seen in the early fall (1991 September 30) observations of Flynn & Mendillo (1993) acquired when the Moon was nearing last quarter.

4. ANALYSIS OF SODIUM OBSERVATIONS

Analysis of ground-based sodium observations in this paper will be restricted to the two sunward ($D_1 + D_2$) radial brightness profiles that have the greatest altitude coverage. Study of such profiles provides a sensitive method for probing the importance of both the ambient atom atmosphere relatively near the surface and the hotter source atom atmosphere at much larger lunar altitudes. Observations selected for the analysis are (1) those of Potter & Morgan (1988b) acquired on 1988 October 2–3, when the Moon was near last quarter (lunar age 21.2–22.2 days) with spatial coverage from the limb to 1200

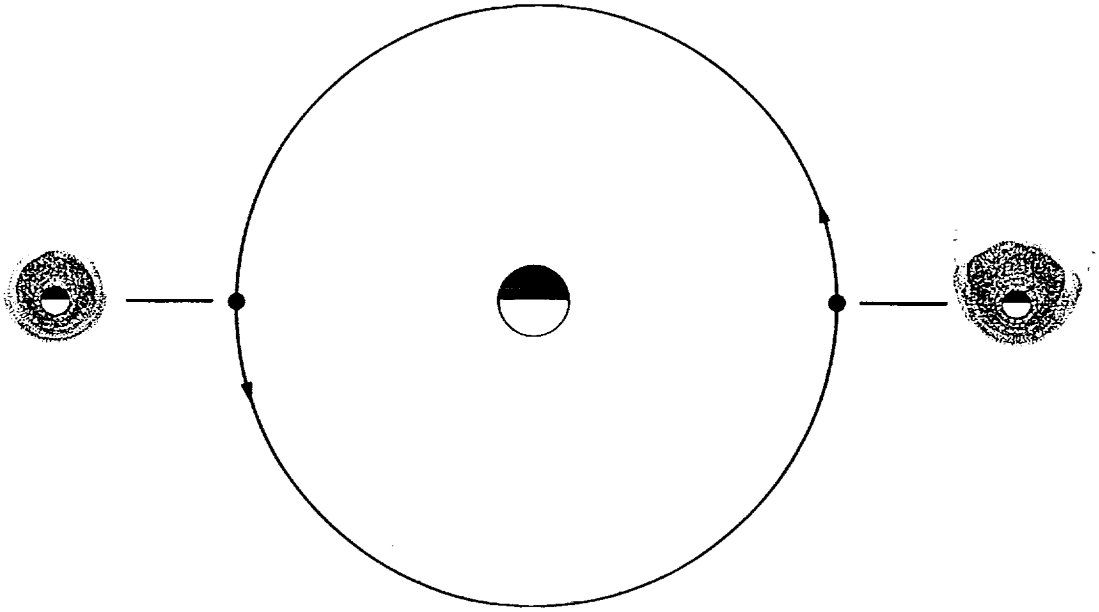

FIG. 7*a*

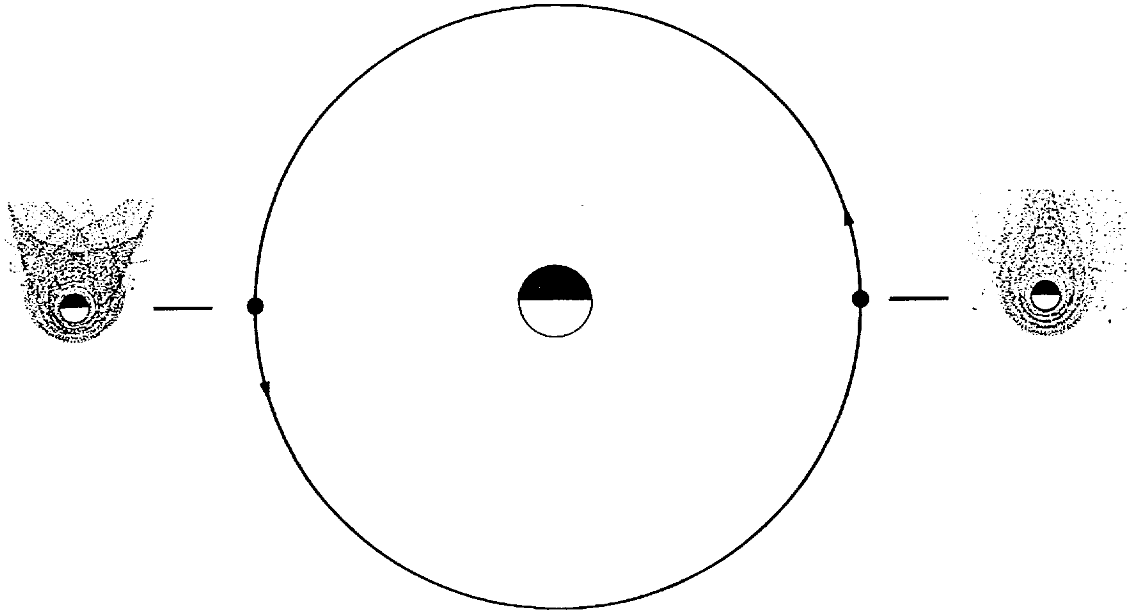

FIG. 7*b*

FIG. 7.—Comparison of the spatial character of the lunar sodium and potassium atmospheres at first and last quarters. The Moon's position is shown (not to scale) in relation to the Earth and Sun at first quarter (*right*) and last quarter (*left*) by the two dots on its orbit (*large circle*). The shape and size of the lunar sodium atmosphere in (*a*) and the potassium atmosphere in (*b*) are shown in dot-plot representation (properly scaled to the Moon) for the case where the Moon-Earth system is moving 1.5 km s^{-1} away from the Sun at first quarter and 1.5 km s^{-1} toward the Sun at last quarter. The dot plots were generated for an atom surface ejection speed of 2.0 km s^{-1} (below the lunar escape of 2.375 km s^{-1}), and each dot occurs at a time interval of 900 s along each of the 259 atom trajectories used.

km (i.e., ~0.7 lunar radii) above the limb and (2) those of Mendillo et al. (1991) acquired on 1991 February 20 when the Moon was nearing first quarter (lunar age ~5 days) with spatial coverage from ~1430 to ~7000 km (i.e., ~0.8–4.0 lunar radii) above the limb.

Model calculations are first undertaken to study the effects on the (D_1 + D_2) radial brightness profile of different combinations for the thermal accommodation and sticking coefficients for sodium on the lunar surface. Upon adopting for the sodium source atoms a Maxwell-Boltzmann velocity distribution on the sunlit surface with a temperature of 1000 K and a uniform hemispherical flux of 1.3 × 10^6 atoms cm^{-2} s^{-1}, calculated brightness profiles that are appropriate for the observing conditions of Potter & Morgan (1988b) are presented in Figure 15 along with their data. Model brightness profiles are shown for the four indicated combinations of the accommoda-

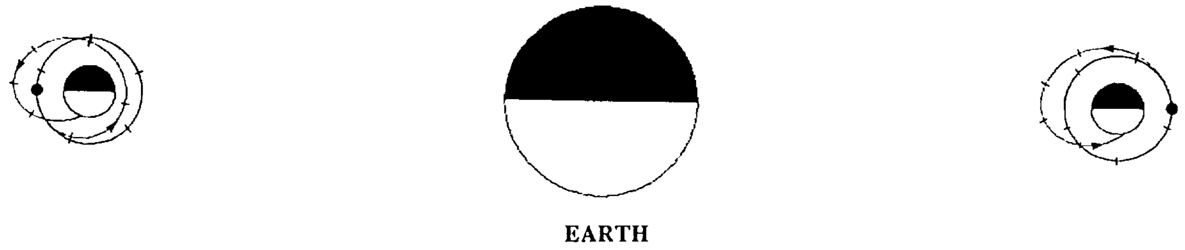

FIG. 8.—Solar radiation acceleration driven decay of a satellite orbit about the Moon. The time evolution of the orbit of a sodium atom, initially launched at the dot in the indicated direction so as to acquire the indicated circular orbit of two lunar radii about the Moon in the absence of solar radiation acceleration, is shown at first quarter (*right*) and last quarter (*left*) when solar radiation acceleration is acting. The Sun-Earth radial velocity is zero. Tick marks on the circular and decaying (ballistic) orbits occur at 1 hr intervals.

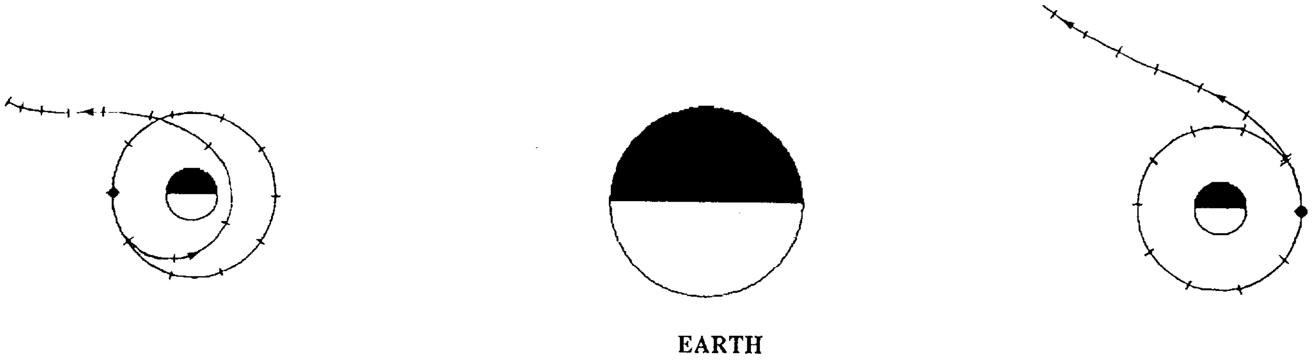

FIG. 9.—Solar radiation acceleration driven escape of a satellite orbit about the Moon. The time evolution of the orbit of a sodium atom, initially launched at the dot in the indicated direction so as to acquire the indicated circular orbit of three lunar radii about the Moon in the absence of solar radiation acceleration, is shown at first quarter (*right*) and last quarter (*left*) when solar radiation acceleration is acting. The Sun-Earth radial velocity is zero. Tick marks on the circular and escaping orbits occur at 1 hr intervals.

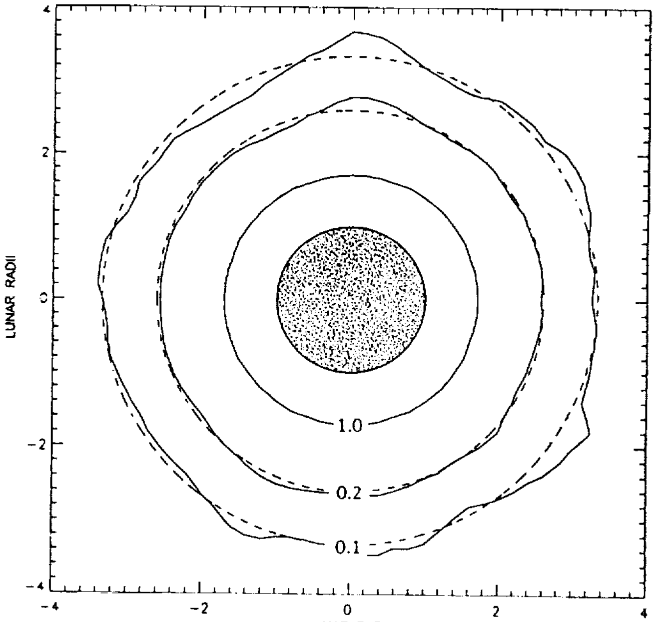

FIG. 10

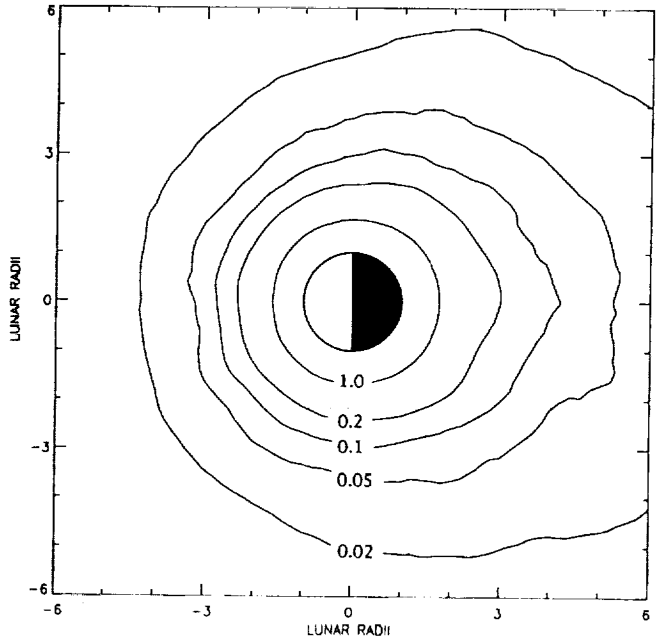

FIG. 11

FIG. 10.—Monte Carlo model comparison with the Chamberlain model. Normalized column density contours for sodium atoms are shown by the dashed line as determined by integrating the analytic expressions of Chamberlain (1963) for the exospheric number density produced by ballistic and escape orbits for a surface source with a 1000 K Maxwell-Boltzman velocity distribution. The same result calculated by the Monte Carlo model for 100,000 particles is shown by the solid line.

FIG. 11.—Chamberlain model with solar radiation acceleration. The normalized column density contours are shown as calculated using the Monte Carlo model to simulate the effect on the Chamberlain model in Fig. 10 of the addition of a constant solar radiation acceleration of 3.1 cm s^{-2} (near the maximum value for sodium atoms in Fig. 4). The spherically symmetric surface source has a 1000 K Maxwell-Boltzmann velocity distribution.

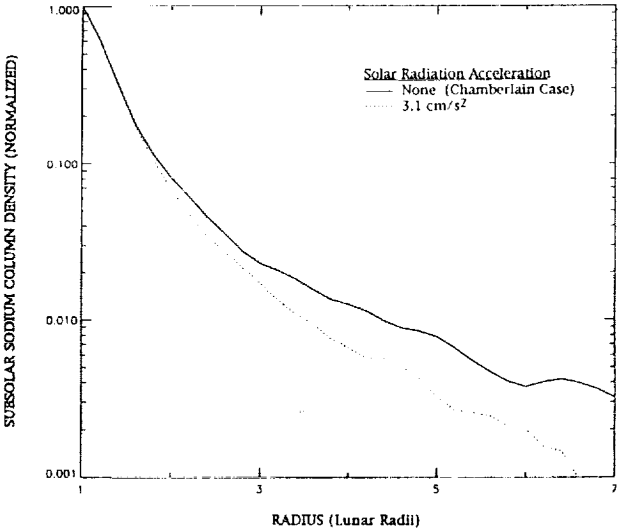

FIG. 12.—Effect of solar radiation acceleration on the subsolar sodium column density. The normalized subsolar column density profile (*dotted line*), corresponding to the calculation in Fig. 11 which includes solar radiation acceleration, is compared to the column density profile (*solid line*) calculated with the Monte Carlo model to simulate a Chamberlain model which excludes solar radiation acceleration.

tion and sticking coefficients. For no surface accommodation and a sticking coefficient of 10%, the calculated profile has a similar slope to the observations beyond a radius of ~1.4 lunar radii but has a slope within this distance that is too steep. For this choice of the two surface coefficients, ballistic atoms will bounce on the surface creating an ambient atom atmosphere. Their initial velocity range but not their velocity distribution is preserved as their population is diminished both by surface sticking and photoionization. By comparison with the brightness profile for 100% sticking, where the ballistic atoms have no bounces and hence there is no ambient atom atmosphere, it is clear that this bouncing for 10% sticking has increased the brightness profile by a factor of ~5 near the surface and by a factor of ~1.6 at a radial distance of two lunar radii. Adopting a more realistic case of an accommodation coefficient of 50% and keeping the sticking coefficient at 10%, the ambient atom atmosphere is dramatically reduced and is now restricted to an enhanced region near the surface (mostly within 0.2 lunar radii). The restricted vertical domain of the ambient atom atmosphere is now determined by the surface temperature rather than the temperature of the source atoms, and the density is now greatly diminished by the 10% sticking coefficient because of the larger number of bounces that occur for the thermal ambient atoms during their photoionization lifetime. The model brightness profile fits the data reasonably well beyond a radial distance of 1.2 lunar radii, but within this distance the observations do not show the rapid rise in the brightness that is produced by the ambient atom atmosphere. Increasing the sticking coefficient to 50% and keeping the accommodation coefficient at 50% further reduces the contribution of the ambient atom atmosphere near the surface. However, the surface brightness is still noticeably larger than the observations. Finally, increasing the sticking coefficient to 100% completely eliminates the ambient atom atmosphere and provides a reasonable match of the model to the complete observed brightness profile. The model derived sodium number density at the surface is 54 atoms cm^{-3} and is similar to the value of 44 atoms cm^{-3} derived by Potter & Morgan (1991) using a Chamberlain model with a Maxwell-Boltzmann velocity distribution of 1150 K.

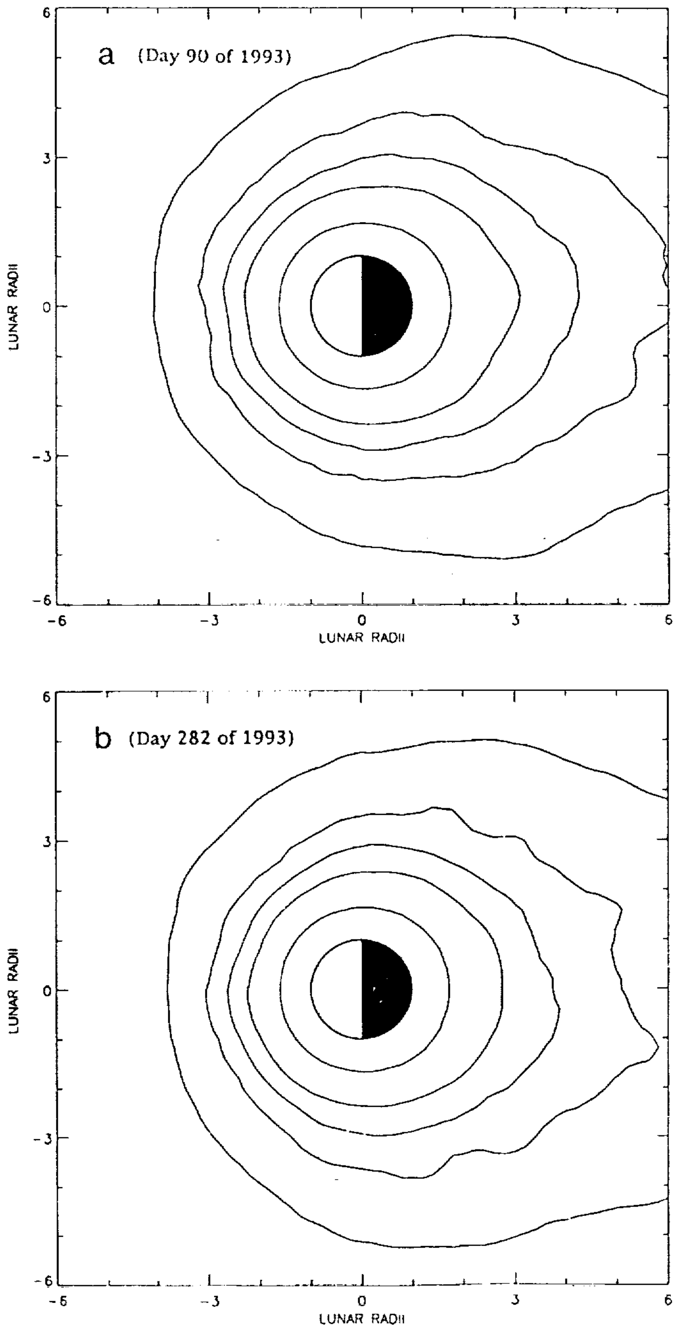

FIG. 13.—Column density for the lunar sodium atmosphere. Model calculations for the lunar sodium column density are compared in (*a*) for the case of an expanded atmosphere/coma at first quarter in the spring (day 90 of 1993) and in (*b*) for the case of a contracted atmosphere/coma at last quarter in the fall (day 282 of 1993). A spherically symmetric surface source with a 1000 K Maxwell-Boltzmann velocity distribution was assumed in both cases. Normalized column density contours are, from inside to outside, 1.0, 0.2, 0.1, 0.05, and 0.02. Sodium in the antisunward coma escapes more readily in the spring but is noticeably restricted to more bound orbits in the fall.

The lunar sodium model is now applied to the analysis of the sunward brightness profile of the more distant measurements of Mendillo et al. (1991). Upon adopting for the sodium source

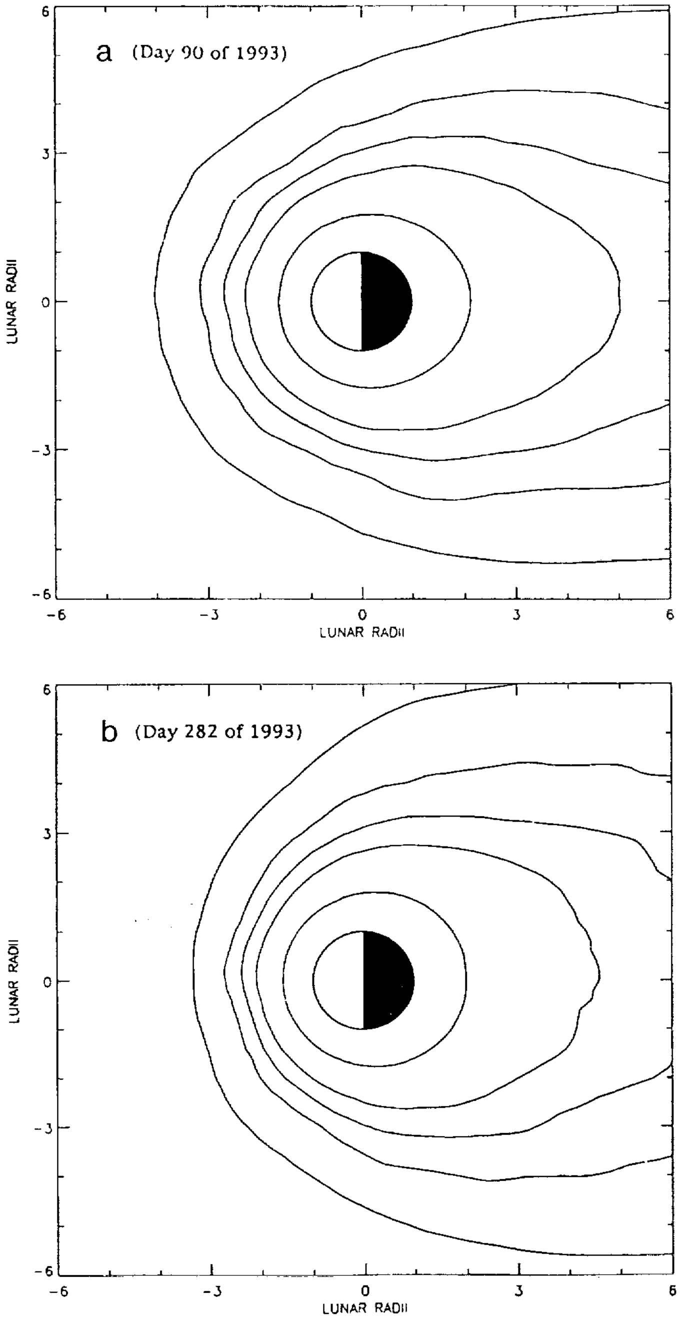

FIG. 14.—Column density for the lunar potassium atmosphere. Model calculations for the lunar potassium column density are compared in (*a*) for the case of an expanded atmosphere/coma at first quarter in the spring (day 90 of 1993) and in (*b*) for the case of a contracted atmosphere/coma at last quarter in the fall (day 282 of 1993). A spherically symmetric surface source with a 2000 K Maxwell-Boltzmann velocity distribution was assumed in both cases. Normalized column density contours are, from inside to outside, 1.0, 0.2, 0.1, 0.05, and 0.02. In the spring, the potassium atmosphere above the subsolar point is more expanded and the antisunward coma escapes more readily than in the fall.

atoms a Maxwell-Boltzmann velocity distribution on the sunlit surface with a temperature of 1000 K, adopting a uniform hemispherical flux of 2.1×10^6 atoms $\mathrm{cm^{-2}\,s^{-1}}$, and choosing the sticking coefficient to be 100% as above, a sunward brightness profile is obtained and compared to the observations in Figure 16. The observations of Mendillo et al. (1991) are also reasonably well fitted (*solid line*) by the same source that fits the observations of Potter & Morgan (1988b), except that the uniform sunlit hemispherical flux in the latter observation is about 40% lower (*dashed line*). The model-derived sodium number density at the surface is 90 atoms $\mathrm{cm^{-3}}$ and is somewhat larger than the value of 52 atoms $\mathrm{cm^{-3}}$ obtained by Mendillo et al. (1991) assuming hemispherical symmetry and using a power law (r^{-4}) column density extrapolation to the surface. Intensity profiles were also obtained by Mendillo et al. (1991) in the antisunward coma in the tail lobes to either side of the lunar shadow region. These profiles showed a much less steep power-law slope of -1.3 instead of -4 for the sunward profile. Exploratory model calculations show that to obtain slopes this small, the source on the sunlit hemisphere must be more enhanced near the subsolar point than the terminator.

The model fit in Figure 16, which requires source atoms with a 1000 K Maxwell-Boltzmann velocity distribution uniformly distributed on the sunlit hemisphere and no ambient atom atmosphere (i.e., 100% sticking), is, however, not a unique fit to the observations. It is one of many fits that can be obtained by choosing different combinations of the velocity distribution for the source atom atmosphere and the gas-surface conditions for the ambient atom atmosphere. The absence of an ambient atom atmosphere for the sunward lunar temperatures of ~100–400 K is, in fact, not expected given their likely short adsorption times on the sunlit surface, although more complex surface interactions could introduce some sticking. For the brightness profiles in Figure 16, the presence of a whole class of solutions which have an ambient atmosphere can be readily seen as follows. For the most physically likely conditions where the ambient atoms are thermally accommodated to the surface in a few bounces (i.e., the accommodation coefficient is ~0.5 or so), it can be seen from Figure 15 that the ambient atom atmosphere contributes to the brightness profile only near the surface (i.e., radius <1.4 lunar radii or altitudes <700 km) while the source atom atmosphere contributes to the brightness profile both near the surface and at large distances from the surface. If a 1000 K Maxwell-Boltzmann velocity distribution is chosen for the source atoms, no ambient atoms are needed to fit the observation near the surface since the population of lower velocity source atoms is sufficient. If, however, this population of lower velocity source atoms is reduced relative to the population of the higher velocity source atoms (which is needed to fit the observations at large distances for the surface), then an ambient atom atmosphere population will be required near the surface. This required ambient atom atmosphere will be created when source atoms from both the lower velocity population and the higher velocity population encounter the surface. Since the relative contribution of these two source atom populations can be adjusted by the selection of different shapes for velocity distribution of the source atoms, the amount of ambient atom atmosphere population created near the surface can also be varied. The amount of ambient atom atmosphere population can, in addition, be varied by choosing different values for the sticking coefficient. More complex variations in the ambient atom atmosphere population can be envisioned by having the values of the sticking and accommodation coefficients (both assumed constant here) depend upon the impact energy of the atom with the surface and the surface temperature. Various combinations of the initial velocity distribution for the source atoms and the sticking coefficient may therefore be considered in tailoring the model brightness profile to fit the sodium observations in Figure 16.

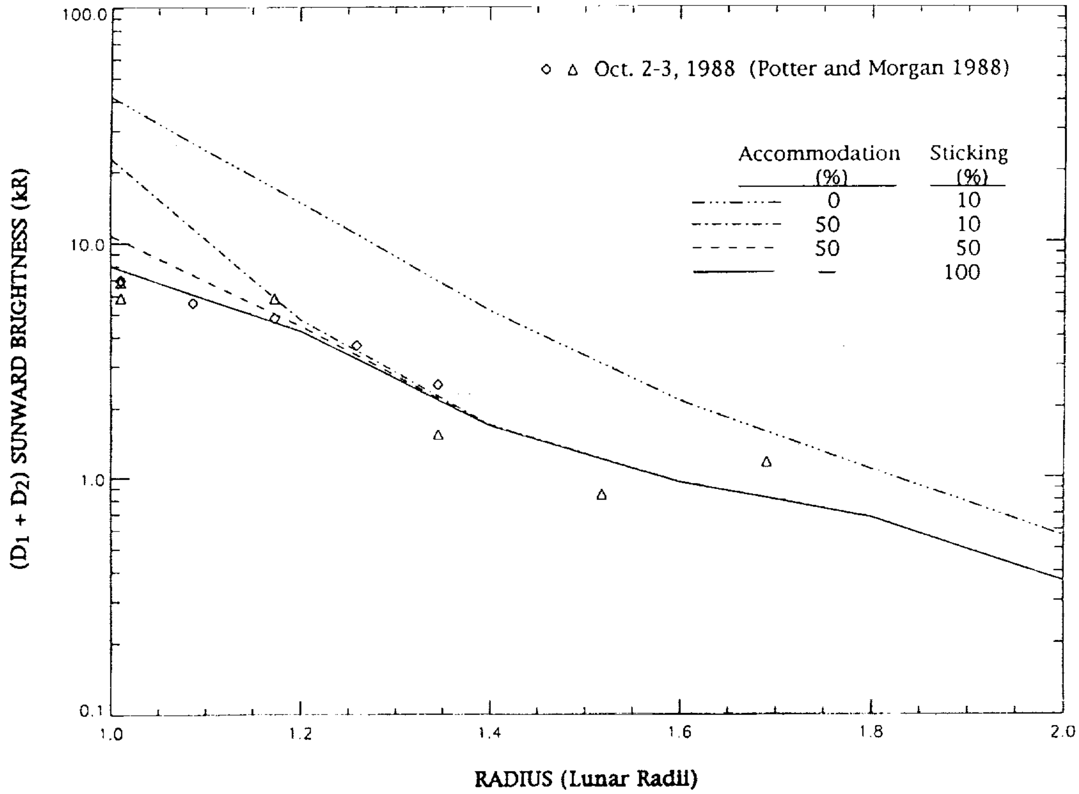

FIG. 15.—Effect of gas-surface interactions on the subsolar brightness profile for sodium. Model calculations for four different combinations of the energy accommodation coefficient and the surface sticking coefficient are shown for the subsolar ($D_1 + D_2$) brightness profile for sodium and compared with the observed ($D_1 + D_2$) brightness data of Potter & Morgan (1988b). The Monte Carlo simulation was undertaken for 100,000 source atoms ejected from the surface. See text for discussion.

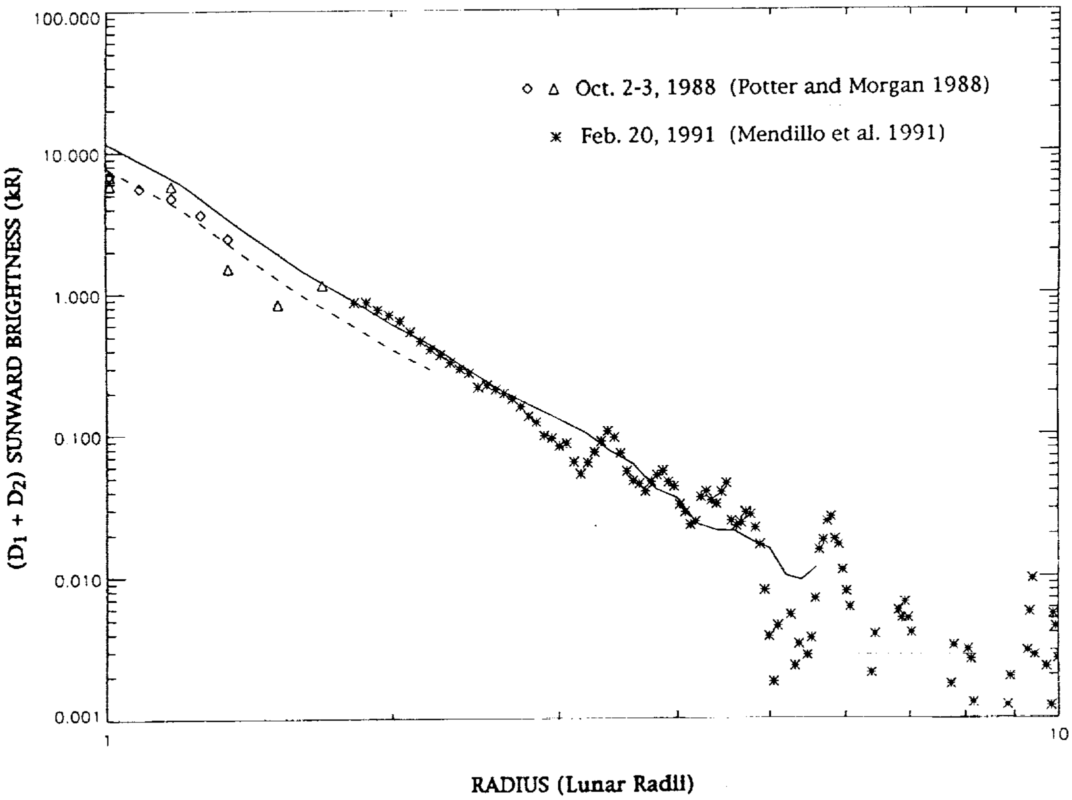

FIG. 16.—Analysis of observations for the lunar sodium atmosphere for a Maxwell-Boltzmann surface source. The sodium ($D_1 + D_2$) brightness profiles observed by Mendillo et al. (1991) and Potter & Morgan (1988b) near first and last quarters, respectively, are both fitted quite well (*solid line* and *dashed line*) using the Monte Carlo sodium model. A uniform sunlit-hemisphere source with a 1000 K Maxwell-Boltzmann velocity distribution, having only a small difference in the sodium surface density for the two observations, was adopted in the model. The Monte Carlo simulation was undertaken for 100,000 source atoms ejected from the surface. See text for discussion.

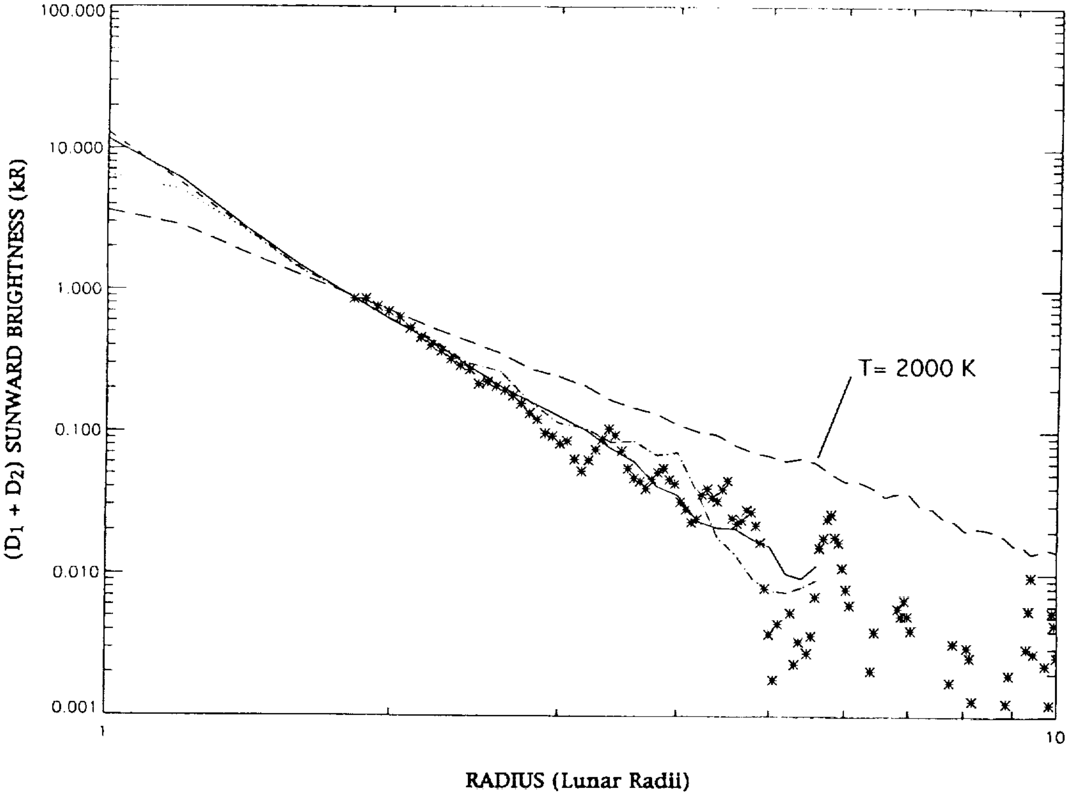

FIG. 17.—Analysis of observations for the lunar sodium atmosphere for a truncated Maxwell-Boltzmann surface source. Two model calculations (*dotted line* and *short-dashed line*) for the $(D_1 + D_2)$ sunward brightness profiles appropriate to the observations of Mendillo et al. (1991) are compared with the measured sunward profile (*asterisks*) and the fit (*solid line*) to their profile given in Fig. 16. A uniform sunlit-hemisphere source of 0.94×10^6 atoms cm^{-2} s^{-1} for a 1200 K Maxwell-Boltzmann velocity distribution truncated below 1 km s^{-1} was adopted for the two model calculations, and 10,000 source atoms were ejected from the surface. The model profile for 100% sticking is given by the dotted line, and the model profile for 15% sticking and an accommodation coefficient of 50% is given by the short-dashed line. A dot-dashed line is produced when these two model profiles merge. In addition, for comparison with the model calculation (*solid line*) for a nontruncated 1000 K Maxwell-Boltzmann velocity distribution with 100% sticking, a similar model calculation, but with a temperature of 2000 K, is given by the long-dashed line.

In Figure 17, a simple example of a model calculated brightness profile (*short-dashed line*), which includes an ambient atmosphere and which provides an equally good fit to the observations of Mendillo et al. (1991) as the model fit (*solid line*) of Figure 16, is illustrated. The modified velocity distribution assumed for the sodium source atoms is a 1200 K Maxwell-Boltzmann, truncated below 1 km s^{-1}, with a uniform hemispherical flux on the sunlit surface of 0.94×10^6 atoms cm^{-2} s^{-1}. A sticking coefficient of 15% and an accommodation coefficient of 50% are assumed in the model calculation. The contribution to the brightness profile of the source atom population is shown by the dotted line, which was determined by a model calculation adopting the truncated Maxwell-Boltzmann with the same uniform hemispherical flux but assuming a sticking coefficient of 100%. By comparing the dotted-line and the short-dashed line, the ambient atmosphere produced by the encounter of source atoms with the surface is seen to contribute about one-half of the surface brightness. If the sticking coefficient were smaller than 15%, the relative brightness contribution of the ambient atmosphere population at the surface would increase. By truncating a Maxwell-Boltzmann velocity distribution with a similar temperature at a slightly higher or lower velocity and making small changes in the sticking coefficient, it is clear that other fits to the data could also be obtained where the ambient atom atmosphere would be, respectively, larger or smaller than the 15% sticking case.

As an additional example (not graphically shown), a reasonable fit to the data of Mendillo et al. (1991) can also be achieved for a 1200 K Maxwell-Boltzmann velocity distribution, truncated below 1.5 km s^{-1}, with a somewhat smaller uniform hemispherical flux on the sunlit surface of 0.35×10^6 atoms cm^{-2} s^{-1} for 100% sticking. The calculated brightness profile within ~1200 km of the surface for this source atom atmosphere, however, falls well below the source atom atmosphere for the 1.0 km s^{-1} truncated case (*dotted-line* fit of Fig. 17) discussed above and has a surface brightness that is a factor of ~5 lower than the corresponding fit for the 1.0 km s^{-1} truncated case including the ambient atom atmosphere (*short-dashed line* in Fig. 17). To provide a similar fit for the 1.5 km s^{-1} truncated case, the ambient atom atmosphere would need to contribute about 80% of the surface brightness. A factor of ~4 increase in surface brightness, which is most of the ambient atmosphere required, can be obtained by simply selecting a much smaller value for the surface sticking coefficient ~1%. Therefore, within certain limits, it is clear that solutions may be obtained for various combinations of source atom velocity distributions and gas-surface interaction conditions, with increasing complexity added if the surface sticking and accommodation coefficients are, for example, dependent on the atom impact speed and the surface temperature. If, however, the temperature of the Maxwell-Boltzmann velocity distribution is increased significantly beyond ~1000 K, the slope of the brightness profile at larger distances from the lunar limb will become less steep than the observations. This is illustrated in Figure 17 by the long-dashed line calculated for a non-truncated 2000 K Maxwell-Boltzmann velocity distribution and 100% surface sticking. This brightness profile illustrates that the higher-velocity source atoms cannot, for example, have a velocity tail characterized by a Maxwell-Boltzmann velocity distribution with a temperature of 2000 K or more, which might be crudely representative of a micrometeoroid impact vaporization source.

Model calculations have also been undertaken for the direct source atoms produced by ion sputtering of the lunar surface by protons in the solar wind. For this process, the Sigmund-Thompson sputtering flux velocity distribution is adopted. This flux velocity distribution with a maximum cutoff speed is proportional to the local velocity integrated surface flux ϕ_0 and depends upon two velocity parameters, v_M and v_b:

$$\phi(v; v_M, v_b) = \phi_0 \frac{1}{v_b D(v_M/v_b)} \left(\frac{v}{v_b}\right)^3 \left(\frac{v_b^2}{v^2 + v_b^2}\right)^3 \times \left[1 - \left(\frac{v^2 + v_b^2}{v_M^2}\right)^{1/2}\right], \quad (2)$$

where $D(v_M/v_b)$ is a dimensionless normalization coefficient which is a function of v_M/v_b (see Smyth & Combi 1988, Appendix D for their case of $\alpha = 3$). The velocity parameter v_b, which for surface sputtering is related to the surface binding energy ($E_b = 1/2mv_b^2$), is also related nonlinearly to the most probable speed v_m of the flux speed distribution and primarily determines v_m. The velocity parameter v_M determines the cutoff speed for the flux distribution and depends, in the case of ion sputtering of a sodium gas, upon the maximum relative speed (and masses) of the incident ion and sodium atom. For solar-wind proton sputtering of sodium atoms in the gas phase, the velocity v_M is ~37.5 km s^{-1} for a nominal solar wind velocity at 1 AU of 450 km s^{-1}. For ion sputtering of sodium atoms from a surface, however, the velocity v_M is expected to be perhaps half of this value due to surface effects (Johnson 1994) so that a value of 15 km s^{-1} is adopted here. For a Sigmund-Thompson distribution, the velocity tail (somewhat before the cutoff speed) decays rather slowly as $\sim v^{-4}$ and provides a much larger relative population for the higher velocity source atoms than does a Maxwell-Boltzmann velocity distribution with a similar most probable speed.

Model calculations for the brightness profile of Mendillo et al. (1991) have been undertaken for direct source atoms based upon the Sigmund-Thompson sputtering flux velocity distribution for the solar wind proton sputtering of sodium atoms isotropically emitted from the sunlit hemisphere of the lunar surface. In these calculations, the sticking coefficient is selected to be 100%, since the critical issue is to investigate the slope of the model derived brightness profile at larger distances from the lunar surface where there are no ambient atoms. For the velocity parameter v_b, which typically has a value of ~1–3 km s^{-1}, three values are selected: 0.5, 0.85, and 2.5 km s^{-1}. These three values span an appropriate range which corresponds, respectively, to a sodium binding energy E_b of ~0.03 eV (~350 K, typical of the higher thermal energy), 0.09 eV (~1000 K, similar to the Maxwell-Boltzmann distribution used above), and 0.74 eV (~8600 K, perhaps a more typical surface binding energy). For the velocity parameter v_M, a value of 15 km s^{-1} is chosen, as discussed above, although a value of 8 km s^{-1} would not appreciably alter the velocity population of the distribution below several kilometers per second and consequently would not appreciably alter the brightness profile within the present maximum radius for the observations of ~6 lunar radii. Model calculated brightness profiles normalized to unity for these three values of v_b are presented in Figure 18 and compared with the normalized 1000 K Maxwell-Boltzmann fit in Figure 16 for 100% sticking (*solid line*). For all three values of v_b, the ion sputtered profiles have a slope that is significantly less steep at larger distances from the lunar surface than the 1000 K Maxwell-Boltzmann fit of Figure 16. A comparable fit to the observation can be accomplished only by artificially reducing the velocity parameter v_M for the cutoff speed to unrealistically small values so as to eliminate the high-velocity source atoms in the tail of the Sigmund-Thompson sputtering flux distribution. Such a nonphysical fit can be obtained, for example, for v_b equal to 0.85 km s^{-1} if the value of v_M is reduced to 2.7 km s^{-1}, as illustrated by the short-dashed line in Figure 18. While such a small v_M is nonphysical when interpreted in the context of the physics of ion surface sputtering appropriate to this system, the sputtering distribution with a small v_M may more generally be regarded as yet another example of a distribution that leads to a reasonable match to the observations. For α particles in the solar wind, which are thought to produce a comparable flux of sputtered sodium (because the lower ion abundance is offset by a larger sputtering yield), the value of v_M is even larger, so that a similar modeling result as obtained for proton sputtering would occur. The incorrect behavior of the model calculated brightness profiles at larger distances from the lunar surface for realistic values of the cutoff speed parameter v_M, therefore, clearly indicates that the direct source produced by solar wind ion sputtering cannot be a dominant source for the sodium source atoms in the lunar atmosphere.

The relationship between the sodium flux ϕ_S for the source atoms and the net loss of sodium flux ϕ_L from the lunar surface will now be examined. The sodium flux ϕ_S may be divided into a ballistic flux ϕ_B and an escaping flux ϕ_E:

$$\phi_S = \phi_B + \phi_E . \quad (3)$$

The sodium flux ϕ_S sustains a zenith column density N, which is determined by the average flight times for ballistic atoms $\bar{t}_B$ and escape atoms $\bar{t}_E$ in the atmosphere before being lost to the surface by sticking, to the solar wind by photoionization, or to gravitational escape. The average flight times depend upon the velocity distribution for the source atoms, which determines their residence time in the gas column, and upon the bounce times of the ambient atoms in the column, which are determined by the accommodation and sticking coefficients. Expressed simply, the relationship between the column density N, the sodium fluxes ϕ_B and ϕ_E, the average flight times $\bar{t}_B$ and $\bar{t}_E$, and the photoionization lifetime τ is given by

$$N = \int_0^{\bar{t}_B} \phi_B e^{-t/\tau} dt + \int_0^{\bar{t}_E} \phi_E e^{-t/\tau} dt = t_B \phi_B + t_E \phi_E , \quad (4)$$

where the effective average residence times of ballistic atoms t_B and escape atoms t_E in the atmosphere are

$$t_B = \tau(1 - e^{-\bar{t}_B/\tau}) , \quad (5)$$

$$t_E = \tau(1 - e^{-\bar{t}_E/\tau}) . \quad (6)$$

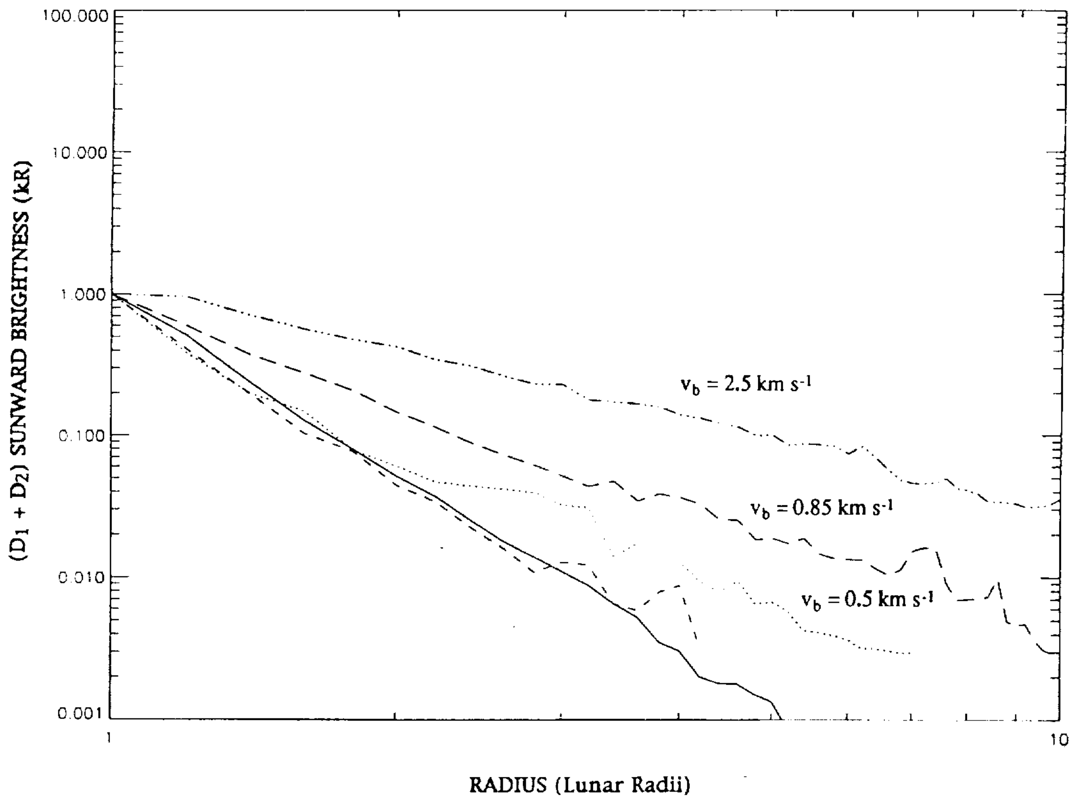

FIG. 18.—Analysis of observations for the lunar sodium atmosphere for a solar-wind proton sputtering source. Four model calculations for the $(D_1 + D_2)$ sunward brightness profiles of Mendillo et al. (1991) based upon a Sigmund-Thompson sputtering flux velocity distribution with a uniform sunlit-hemisphere source are compared with the Maxwell-Boltzmann model fit (*solid line*) to the observed profile given in Fig. 16. All model profiles have been normalized to unit brightness at the surface to facilitate the comparison. Each Monte Carlo simulation was undertaken for 10,000 source atoms ejected from the surface. The top three model profiles correspond to the indicated value for the velocity parameter v_b, where v_M has a value of 15 km s^{-1}. The lowest model profile (*short-dashed line*), which reasonably well matches the solid-line profile, corresponds to a value of v_b = 0.85 km s^{-1} and an unrealistically low value of v_M = 2.7 km s^{-1}.

Once the column density is established by the source atoms and ambient atoms, the net loss of the sodium flux ϕ_L from the lunar surface is determined by the photoionization loss from the gas column, and the non-ionized fraction of the sodium escape flux ϕ_E from the Moon:

$$\phi_L = \frac{N}{\tau} + \phi_E e^{-t_E/\tau} = \phi_B \frac{t_B}{\tau} + \phi_E . \qquad (7)$$

The sodium escape flux ϕ_E is determined by the velocity distribution for the source atoms and their spacetime and velocity-dependent orbital evolution in the lunar gravitational and solar radiation accelerations.

For the limiting case of no surface sticking (i.e., $\bar{t}_B \gg \tau$), t_B is approximately equal to τ, so that

$$\phi_L = \phi_B + \phi_E = \phi_S , \qquad (8)$$

and the source flux and loss flux are equal. For the limiting case of rapid surface sticking relative to the photoionization lifetime (i.e., $\bar{t}_B \ll \tau$), t_B is approximately equal to $\bar{t}_B$, so that

$$\phi_L = \phi_B \frac{\bar{t}_B}{\tau} + \phi_E = \phi_S \frac{\bar{t}_B}{\tau} + \phi_E\left(1 - \frac{\bar{t}_B}{\tau}\right) , \qquad (9)$$

and the source flux can be much larger than the loss flux when the escape flux is small.

For the 1000 K Maxwell-Boltzmann fit in Figure 16 with 100% sticking, ϕ_E is small ($\sim$ 1.2% of ϕ_S), $t_B = 0.58$ hr, and $\tau = 15$ hr for sodium, so that for $\phi_S = 2.1 \times 10^6$ atoms cm^{-2} s^{-1}, we have $\phi_L = 0.050\phi_S = 1.1 \times 10^5$ atoms cm^{-2} s^{-1}. For the 1200 K truncated Maxwell-Boltzmann fit in Figure 17 with 15% sticking, ϕ_E is somewhat larger ($\sim$4.6% of ϕ_S), $t_B = 1.52$ hr, and $\tau = 15$ hr for sodium, so that for $\phi_S = 0.94 \times 10^6$ atoms cm^{-2} s^{-1}, we have $\phi_L = 0.14\phi_S = 1.3 \times 10^5$ atoms cm^{-2} s^{-1}.

5. DISCUSSION

Model simulations discussed in § 4 for the more distant lunar sodium sunward brightness profile of Mendillo et al. (1991) indicate that the source atoms have a surface flux that is as high as $\sim 2 \times 10^6$ atoms cm^{-2} s^{-1} when no ambient atom atmosphere is allowed and a surface flux that may be almost an order of magnitude lower when the ambient atom atmosphere is allowed to dominate the surface density. In these cases, the source atoms must have a velocity distribution with a tail that is only mildly nonthermal (i.e., characterized approximately by a Maxwell-Boltzmann distribution with a temperature of $\sim$1000 K) in order to fit the sunward brightness profile at larger distances (> 0.4 lunar radii) above the lunar surface than can be populated by a thermally accommodated ambient atom atmosphere. For the lunar sodium sunward brightness profile of Potter & Morgan (1988b) extending from the surface to 1200 km altitude, a model fit was obtained with the same source atom velocity distributions (and their properly created ambient atmosphere), but with a source rate lowered by ~40%. The thermal accommodation of sodium ambient atoms to the surface is physically expected, as demonstrated for the hotter surface of Mercury (Smyth & Marconi 1995), and may occur in a few encounters, although this rate may depend on atom velocity and surface temperature. In the model simulations, the presence or absence of the lunar ambient atom atmosphere depends upon the shape of the source atom velocity distribution at lower speeds (< 1.5 km s^{-1}) and the nature of the surface sticking and accommodation coefficients for the ambient atoms as illustrated in Figures 16 and 17. As discussed in § 4, it is clear that there are other more complex combinations for the shape of the velocity distribution and the sticking coefficient that could be chosen to fit the observed sunward brightness profile.

Since solar wind sputtering is certain to occur, it is interesting to consider how this source mechanism exists in the light of the source strength and velocity distribution for the sodium atoms required above. The direct sodium source, characterized by a Sigmund-Thompson sputtering flux velocity distribution is not compatible, as noted in Figure 18. Because the source strength of the direct source is also small (~3%–10% of the total source flux, best estimated in Table 2 to be $\sim 1.5 \times 10^5$ atoms cm^{-2} s^{-1}) compared to the model-derived flux from the observations, the D-line emission brightness signature of the direct source will be overwhelmed by other sources nearer the Moon and will become evident only at much larger radial distances which are likely to be radially beyond the useful observational data in Figure 16. The delayed source, however, may be compatible, since it is characterized by a quasi-thermal flux velocity distribution, which could well be similar to the required source velocity distribution with an ~1000 K Maxwell-Boltzmann–like tail. The estimated sodium flux for the delayed source atoms (~68%–74% of the total source strength of 1.5×10^5 atoms cm^{-2} s^{-1}) is $\sim 1 \times 10^5$ atoms cm^{-2} s^{-1} near the subsolar point and is comparable to the smallest sodium flux of 3.5×10^5 atoms cm^{-2} s^{-1} required for the observations of Mendillo et al. (1991) and the corresponding 2.1×10^5 atoms cm^{-2} s^{-1} (i.e., 40% less) required for the observations of Potter & Morgan (1988b) when a large ambient atmosphere is present. Considering the significant time variation of the solar wind flux from its nominal value and the uncertainties in estimating the yields and sodium surface abundance in Table 2, it would thus appear that solar wind sputtering of the lunar surface could be a viable mechanism for supplying the sodium source atoms to the atmosphere.

In contrast, given the source strength and velocity distribution for the sodium atoms required by the model calculations of § 4, micrometeoroid impact vaporization would appear unlikely to be a competitive source for the sodium lunar atmosphere. First, the best estimated source strength for micrometeoroid impact vaporization in § 2.2 is too small, only (2–3) $\times 10^4$ atoms cm^{-2} s^{-1}, which is about an order of magnitude smaller than the smallest sodium flux required in the model calculations. Second, the vapor velocity distribution, although uncertain as discussed in § 2.2, is generally thought to be characterized by a temperature of a few thousand degrees and is too energetic. As noted in Figure 17, even a velocity tail for the source atoms characterized by a 2000 K Maxwell-Boltzmann velocity distribution is too hot and produces a brightness profile at larger distances from the limb that is significantly less steep than the observed profile. Third, the spatial distribution of the atmosphere produced by micrometeoroid impact vaporization should be somewhat isotropic and perhaps organized with azimuthal symmetry on the lunar hemisphere facing in the direction of Earth's orbital motion and is not expected to decrease with angular distance from the subsolar point of the Moon, which is the pattern supported by the sodium observations (Mendillo et al. 1991; Flynn & Mendillo 1993; Potter & Morgan 1994) and by our limited modeling of the antisunward tail lobes. Given the small source strength, the sodium brightness profile for micrometeoroid impact vaporization should be suppressed somewhat below the observed brightness profile in Figure 17 and hence be rendered undetectable at these radial distances.

Solar photon-stimulated desorption, on the other hand, would appear to be a possible but a highly uncertain candidate. This uncertainty stems from having laboratory studies for only a very limited number of materials so that the various and complex physical processes that characterize photon-stimulated desorption are at present poorly understood. The velocity distribution and yield of the liberated atoms, for example, appear to be sensitive to the composition, the detailed structure of the surface material, the temperature of the surface, and the wavelength of the bombarding photons. As a result, it is not clear that one can easily extrapolate from the materials studied to the lunar materials. However, it appears that for the materials studied up to now, neutral metal atoms liberated from smooth surfaces under photodesorption characteristically can display nonthermal Maxwellian-like distributions. For the porous lunar surface, this would likely produce an atmosphere with a minor component from the direct source that is nonthermal and a major component from the delayed source that is more thermalized. Whether or not the composite atmosphere would be too thermalized in nature to fit the observations is difficult to assess at the moment, but it might be compatible. Estimates in Table 2 for the sodium flux from photon-stimulated desorption vary from a high value of 3×10^6 to 3×10^7 atoms cm^{-2} s^{-1}, as given by McGrath et al. (1986), to an intermediate value of 3×10^4 atoms cm^{-2} s^{-1}, as given by Killen, Potter, & Morgan (1990), and to a low value of 5×10^3 atoms cm^{-2} s^{-1}, as given by Morgan & Shemansky (1991). The estimate for the high value is based upon an effective, but uncertain, dissociation rate in the surface layer, while the estimates for the intermediate and low values are based upon a yield for an ultraviolet solar flux at wavelengths equal to and below Lyα. As discussed in § 2.2, two more recent measurements have shown photon-stimulated desorption yields of Zn and Na of $\sim 10^{-6}$ and 10^{-7} atoms per photon, respectively, for the much longer 3080 Å wavelength photons. For photons at these longer wavelengths, the solar flux is more than a few $\times 10^{15}$ photons cm^{-2} s^{-1}, which is several orders of magnitude larger than the ultraviolet solar flux at wavelengths equal to and below Lyα. If this photon-stimulated desorption process were operative on the Moon at this level, it would produce a sodium flux of $\sim 5 \times 10^5$ to 5×10^6 atoms cm^{-2} s^{-1}, similar to the lower estimated values of McGrath et al. (1986) and sufficient for the model requirements noted above.

6. SUMMARY AND CONCLUSIONS

A brief review of the lunar atmosphere with emphasis on the more recently discovered sodium and potassium atomic species was given. Modeling efforts to date were summarized, and the need was established for more sophisticated models to include the effects on the sodium and potassium atmospheres of a finite atom lifetime, solar radiation acceleration, nonuniform surface sources, surface sources with non-Maxwellian velocity distributions, and various gas-surface interaction processes. A theoretical overview was given to depict the character and to evaluate the relative importance of various physical processes in shaping the lunar sodium and potassium atmospheres. The discussion covered the general nature of exospheric atmospheres and distinguished between the roles of source atoms liberated from the surface and ambient atoms created when source atoms encounter the surface and are allowed to bounce. The four primary factors shaping the atmospheres, sources, sinks, gas-surface interactions, and transport dynamics, were discussed, and various uncertainties were noted. Radiation acceleration produced by resonance scattering of sunlight by sodium and potassium atoms was shown to be an important factor in the transport and lunar escape of source atoms but is too small to be important for fully thermally accommodated ambient atoms which are located near the surface. Because the magnitude of the radiation acceleration experienced by sodium and potassium atoms depends upon the Doppler shift out of the Fraunhofer features in the solar spectrum, it varies with the radial motion and distance of the Moon from the Sun as well as the instantaneous velocity of the atmospheric atoms relative to the Moon. This variability produces in the spring of the year at first quarter an expanded sunward atmosphere with an enhanced escape of gas in the antisunward coma and in the fall of the year at last quarter a contracted sunward atmosphere with a reduction in the escape of gas in the antisunward coma. This behavior has been recently observed (Mendillo et al. 1991; Flynn & Mendillo 1993).

Models for the sodium and potassium atmospheres were developed, verified in the limiting Chamberlain case, and used to illustrate the basic nature of these atmospheres and their spacetime variability for simple source conditions. The sodium model was applied to analyze sodium observations for the sunward ($D_1 + D_2$) brightness profiles obtained near last quarter by Potter & Morgan (1988b) from the surface up to 1200 km altitude and obtained near first quarter by Mendillo et al. (1991) for an altitude between ~1430 and ~7000 km. To match the observed sunward brightness profile at the larger altitudes of the Mendillo et al. observations, it was shown that the surface mechanism for the source atoms must have a velocity distribution with a tail that is mildly nonthermal (like an ~1000 K Maxwell-Boltzmann distribution). For the models presented here, a sodium flux that varied between 0.35 to 2.1×10^6 atoms cm^{-2} s^{-1} was required, depending upon the shape of its velocity distribution at speeds below ~1.5 km s^{-1}. The lower value of 0.35×10^6 atoms cm^{-2} s^{-1} was obtained for a 1200 K Maxwell-Boltzmann distribution which was truncated below 1.5 km s^{-1} and for gas-surface conditions chosen to create a large ambient atmosphere, while the higher value of 2.1×10^6 atoms cm^{-2} s^{-1} was obtained for a 1000 K (untruncated) Maxwell-Boltzmann distribution and for a sticking coefficient of 100% so as to eliminate the ambient atmosphere. Model calculations for Maxwell-Boltzmann velocity distributions with somewhat higher temperatures ($\geq$2000 K) or for the relatively hotter Sigmund-Thompson ion sputtering flux velocity distribution are too energetic, however, and do not fit the observed brightness profile of Mendillo et al. (1991) because their velocity tail produces a model profile that falls off too slowly with increasing distance from the limb. For the lunar sodium sunward brightness profile of Potter & Morgan (1988b) extending from the surface to 1200 km altitude, model fits could be obtained with the same source atom velocity distributions (and their properly created ambient atmosphere), but with a source rate lowered by ~40%. In order to fit simultaneously the sodium tailward brightness lobe, also measured by Mendillo et al. (1991), preliminary model calculations indicate that the strength of the surface source mechanism must be significantly more peaked at the subsolar point than at the terminator.

From the comparison of the source mechanisms discussed in § 2.2 and the model requirements for the speed distribution, sodium flux magnitude, and angular distribution about the Moon of the source atoms, it would appear that solar wind sputtering is a viable mechanism for supplying the sodium source atoms to the atmosphere, while solar stimulated desorption may be possible but is highly uncertain. For the solar wind, the delayed source has approximately the correct flux, a quasi-thermal velocity distribution that could be mildly nonthermal as required, and a source strength that peaks near the subsolar point. Although the various physical processes for photon-stimulated desorption are presently poorly understood, its estimated sodium flux, velocity distribution, and source strength that peaks at the subsolar point are not inconsistent with model requirements. The mechanism of micrometeoroid impact vaporization is, however, unlikely to be a viable mechanism for supplying the sodium source atoms to the atmosphere, since its sodium source is too small, its velocity distribution is probably too hot, and its source strength is unlikely to peak at the subsolar point.

Future modeling efforts will be directed to the analysis of one-dimensional brightness profiles above the limb as a function of the lunar phase, such as those recently reported for sodium by Potter & Morgan (1994), as well as two-dimensional emission images obtained at a particular lunar phase angle, such as one composite sodium image recently reported by Flynn & Mendillo (1993). These more complete data sets, and others anticipated to be acquired in the near future, should provide the opportunity to uncouple and define more completely the shape of the velocity distribution for the source atoms and the gas-surface interaction conditions for the ambient atoms.

Future observations of the lunar sodium and potassium atmospheres for brightness profile and image data as well as very high resolution spectral line profile data to study the velocity distribution of atoms in the sunward atmosphere and escaping tailward coma are very important. In addition, fundamental work in the areas of understanding the nature of gas-surface interactions and surface source processes such as photon-stimulated desorption is clearly needed. A determination of the velocity distribution of gases liberated by micrometeoroid impact vaporization is also highly desirable. General understanding acquired by study of the lunar atmosphere is also particularly useful in the larger context of understanding the sodium and potassium atmospheres of Mercury, Earth, Io, and comets.

We are grateful to C. A. Peterson for many helpful discussions and for developing the description for the distance and radial velocity of the Moon with respect to the Sun. The determination of the potassium solar Fraunhofer features above Earth's atmosphere from ground-based data by R. L. Kurucz is also gratefully acknowledged. This research was supported by the Planetary Atmospheres Program of the National Aeronautical and Space Administration under contract NASW-4576.

REFERENCES

Ahrens, T. J. 1994, private communication
Ahrens, T. J., & O'Keefe, J. D. 1971, Moon, 4, 214
Arlinghaus, H. F., Calaway, W. F., Young, C. E., Pellin, M. J., & Gruen, D. M. 1989, J. Vacuum Sci. Technol., A, 7, 1766
Battin, R. H. 1964, Astronautical Guidance (New York: KcGraw-Hill)
Bjorkholm, P., Golub, L., & Gorenstein, P. 1973, Science, 180, 957
Chamberlain, J. 1963, Planet. Space Sci., 11, 901
Cintala, M. J. 1992, J. Geophys. Res., 97, 947
Eichhorn, G. 1978, Planet. Space Sci., 26, 463
Fastie, W. G., Feldman, P. D., Henry, R. C., Moos, H. W., Barth, C. A., Thames, G. E., & Donahue, T. M. 1973, Science, 182, 710
Feldman, P. D., & Morrison, M. D. 1991, Geophys. Res. Lett., 18, 2105
Flynn, B., & Mendillo, M. 1993, Science, 261, 184
Gault, D. E., Hörz, F., & Hartung, J. B. 1972, Proc. Lunar Planet Sci. Conf., 2, 1421
Gorenstein, P., & Bjorkholm, P. J. 1977, Phys. Earth Planet. Interiors, 14, 289
Gorenstein, P., Golub, L., & Bjorkholm, P. 1974a, Moon, 9, 129
———. 1974b, Science, 183, 411
Haglund, R. F., & Tolk, N. H. 1986, Proc. SPIE, 690, 9
Hapke, B. 1986, Icarus, 66, 270
Hapke, B., & Cassidy, W. 1978, Geophys. Res. Lett., 5, 297
Hodges, R. R., Jr. 1977, Phys. Earth Plan. Interiors, 14, 282
———. 1978, Proc. Lunar Planet. Sci. Conf., 9, 1749
———. 1985, Final NASA Rept. NSG 7034
Hodges, R. R., Hoffman, J. H., & Evans, D. E. 1972, NASA SP-315, 21-1
Hoffman, J. H., Hodges, R. R., & Evans, D. E. 1973, Geochim. Cosmochim. Acta Suppl., 4(3) 2865
Hunten, D. M., Morgan, T. M., & Shemansky, D. E. 1988, The Mercury Atmosphere, ed. F. Vilas, C. Chapman, & M. Matthews (Tucson: Univ. of Arizona Press), 562
Ip, W.-H. 1991, Geophys. Res. Lett., 18, 2093
Johnson, R. E. 1990, Energetic Charged-Particle Interactions with Atmospheres and Surfaces (New York: Springer), 172
———. 1994, private communication
Johnson, R. E., & Baragiola, R. 1991, Geophys. Res. Lett., 18, 2169
Johnson, F. S., Carroll, J. M., & Evans, D. E. 1972, Proc. Lunar Planet. Sci. Conf., 3, 2231
Killen, R. M., Potter, A. E., & Morgan, T. H. 1990, Icarus, 85, 145
Kozlowski, R. W. H., Sprague, A. L., & Hunten, D. M. 1990, Geophys. Res. Lett., 17, 2253
Love, S. G., & Brownlee, D. E. 1993, Science, 262, 550
McGrath, M. A., Johnson, R. E., & Lanzerotti, L. J. 1986, Nature, 323, 694
Mendillo, M., Baumgardner, J., & Flynn, B. 1991, Geophys. Res. Lett., 18, 2097
Morgan, T. H., & Shemansky, D. E. 1991, J. Geophys. Res., 96, 1351
Morgan, T. H., Zook, H. A., & Potter, A. E. 1989, Proc. Lunar Planet. Sci. Conf., 19, 297
O'Keefe, J. D., & Ahrens, T. J. 1977, Proc. Lunar. Planet. Sci. Conf. 8, 3357
Potter, A. E., & Morgan, T. H. 1988a, Science, 241, 675
———. 1988b, Geophys. Res. Lett., 15, 1515
———. 1991, Geophys. Res. Lett., 18, 2089
———. 1994, Geophys. Res. Lett., 21, 2263
Shemansky, D. E. 1993, Workshop on Sodium Atmospheres, Exospheres, and Coronae in the Solar System (San Juan Capistrano, CA)
Shemansky, D. E., & Broadfoot, A. L. 1977, Rev. Geophys. Space Phys., 15, 491
Smyth, W. H., & Combi, M. R. 1988, ApJ, 328, 880
Smyth, W. H., & Marconi, M. L. 1993, Workshop on Sodium Atmospheres, Exospheres, and Coronae in the Solar System (San Juan Capistrano, CA)
———. 1995, ApJ, 441, 839
Sprague, A. L., Kozlowski, R. W. H., Hunten, D. M., Wells, W. K., & Grosse, F. A 1992, Icarus, 96, 27
Townsend, P. C. 1983, in Sputtering by Particle Bombardment, ed. R. Behrich (Berlin: Springer), 147
Tyler, A. L., Kozlowski R. W. H., & Hunten, D. M. 1988, Geophys. Res. Lett., 15, 1141
Wiens, R. C., Burnett, D. S., Calaway, W. F., & Pellin, M. J. 1993, BAAS, 25, 1089

aer

Atmospheric and
Environmental Research, Inc.

840 Memorial Drive
Cambridge, Massachusetts
02139-3771

Telephone
617 547-6207

Facsimile
617 661-6479

www.aer.com

February 11, 1999

NASA Center for Aerospace Information
Attn: Accessioning Department
800 Elkridge Landing Road
Linthicum Heights, MD 21090-2934

Dear Accessioning Department:

Enclosed please find one (1) reproducible and two (2) copies of the final report for the contract NASW-4970 covering the period from February 1, 1995 to January 31, 1999.

Sincerely,

William H. Smyth

William H. Smyth

WHS/eas

Encl.

cc C. Sze (AER)
P542 file

REPORT DOCUMENTATION PAGE

Form Approved
OMB No. 0704-0188

1. AGENCY USE ONLY *(Leave blank)*

2. REPORT DATE
February, 1999

3. REPORT TYPE AND DATES COVERED
Final February 1, 1995 – January 31, 1999

4. TITLE AND SUBTITLE
Comparative Studies for the Sodium and Potassium Atmospheres of the Moon and Mercury

5. FUNDING NUMBERS
NASW-4970

6. AUTHORS
William H. Smyth

7. PERFORMING ORGANIZATION NAME(S) AND ADDRESS(ES)
Atmospheric and Environmental Research, Inc.
840 Memorial Drive
Cambridge, MA 02139

8. PERFORMING ORGANIZATION REPORT NUMBER
P-542

9. SPONSORING/MONITORING AGENCY NAME(S) AND ADDRESS(ES)
NASA Headquarters
Headquarters Contract Division
Washington, DC 20546

10. SPONSORING/MONITORING AGENCY REPORT NUMBER

11. SUPPLEMENTARY NOTES

12a. DISTRIBUTION/AVAILABILITY STATEMENT

12b. DISTRIBUTION CODE

13. ABSTRACT *(Maximum 200 words)*

A summary discussion of recent sodium and potassium observations for the atmospheres of the Moon and Mercury is presented with primary emphasis on new full-disk images that have become available for sodium. For the sodium atmosphere, image observations for both the Moon and Mercury are fitted with model calculations (1) that have the same source speed distribution, one recently measured for electron-stimulated desorption and thought to apply equally well to photon-stimulated desorption, (2) that have similar average surface sodium fluxes, ~2.8 x 10^5 to 8.9 x 10^5 atoms cm^{-2} s^{-1} for the Moon and ~3.5 x 10^5 to 1.4 x 10^6 atoms cm^{-2} s^{-1} for Mercury, but (3) that have very different distributions for the source surface area. For the Moon, a sunlit hemispherical surface source of between ~5.3x 10^{22} to 1.2 x 10^{23} atoms s^{-1} is required with a spatial dependence at least as sharp as the square of the cosine of the solar zenith angle. For Mercury, a time dependent source that varies from 1.5 x 10^{22} to 5.8 x 10^{22} atoms s^{1} is required which is confined to a small surface area located at, but asymmetrically distributed about, the subsolar point. The nature of the Mercury source suggest that the planetary magnetopause near the subsolar point acts as a time varying and partially protective shield through which charged particles may pass to interact with and liberate gas from the planetary surface. Suggested directions for future research activities are discussed.

14. SUBJECT TERMS

15. NUMBER OF PAGES
97

16. PRICE CODE

17. SECURITY CLASSIFICATION OF REPORT
Unclassified

18. SECURITY CLASSIFICATION OF THIS PAGE
Unclassified

19. SECURITY CLASSIFICATION OF ABSTRACT
Unclassified

20. LIMITATION OF ABSTRACT